UNIVERSIDADE DE LISBOA
FACULDADE DE CIÊNCIAS
DEPARTAMENTO DE FÍSICA

High-Density Mapping Analysis of Electrical Spatiotemporal Behaviour in Atrial Fibrillation

Maria Alexandra Cabanos Nunes

Mestrado Integrado em Engenharia Biomédica e Biofísica
Perfil em Sinais e Imagens Médicas

Dissertação orientada por:
Professor Alexandre Andrade
Doutor Sérgio Laranjo

2022

Acknowledgments

First, I would like to thank my supervisors, Dr. Sérgio Laranjo and Prof. Alexandre Andrade, for their expertise, support, and guidance throughout this project.

I would also like to express my gratitude to Prof. Juan Pablo from the University of Zaragoza for all the valuable expertise and guidance.

I would like to acknowledge Dr. Pedro Cunha and Dr. Mário Oliveira from Santa Marta hospital for their insight and expertise.

On a more personal level, a loving thank you to my boyfriend for always being there for me when I needed the most and for all the patience and support through stressful and difficult times. I would also like to thank my family for their precious support and love throughout each and every day. A special thank you to my aunt and godmother, and most importantly, a dear friend of mine, who unfortunately passed away too soon.

A huge thank you to all of my friends for making me laugh and smile, and for all the good times spent together. Clara, Inês, Kamila, Gonçalo, Ana, Guilherme, and Filipe, you are all awesome!

And finally, to the reader, thank you for showing an interest in this work. I hope you will find it compelling and motivating.

Resumo

Doenças cardiovasculares, tais como arritmias, são a principal causa de morte no mundo, especialmente no Sul e no Este da Ásia, e nos Estados Unidos da América [1]. As arritmas são caracterizadas pela alteração no ritmo sinusal normal do coração.

Em particular, a fibrilhação auricular (FA) é a arritmia cardíaca mais comum na prática clínica, contribuindo para mais de 200 mil mortes globalmente em 2017 [2]. Caracteriza-se pela contração rápida e dessincronizada das aurículas, e está associada ao aumento da mortalidade e afecta de forma negativa a qualidade de vida dos pacientes. A FA é geralmente tratada através de medicação, porém quando esta falha, a ablação por cateter é indicada, sendo um tratamento de referência para combater esta patologia. A ablação apresenta uma taxa de sucesso de aproximadamente 50% no primeiro procedimento, sendo necessário efectuar vários procedimentos para aumentar a eficácia do tratamento [3]. A detecção desta patologia envolve, numa primeira fase, a realização de um electrocardiograma (ECG) e, posteriormente um estudo electrofisiológico para saber com precisão onde se localiza e o mecanismo subjacente à mesma. Este último implica o registo da actividade eléctrica através de electrogramas (EGM) locais em diferentes pontos das aurículas e dos ventrículos, com o auxílio de sistemas de mapeamento tridimensionais (3D) electroanatómicos, sendo um procedimento invasivo.

Existem diversos métodos lineares e não lineares que permitem a análise dos EGMs nos domínios do tempo, frequência, fase, entre outros, com a finalidade de melhor compreender os mecanismos subjacentes à FA e, consequentemente aumentar a taxa de sucesso do processo de ablação e melhorar a sua eficiência. Esta área de estudo progrediu significativamente, tanto a nível de hardware, como de software. Apesar disso, os métodos desenvolvidos não têm nem acrescentado benefícios adicionais, nem melhorado significativamente a taxa de sucesso do processo de ablação. Existem várias razões para tal, e grande parte deve-se ao facto destes métodos de análise estarem incorporados nos sistemas de mapeamento e o seu software ser exclusivo. Isto leva a que não consigamos perceber como é que os algoritmos funcionam nos diferentes sistemas de mapeamento para comparar as suas diferenças e semelhanças. Devido a estes constrangimentos, os investigadores são compelidos a desenvolver os seus próprios métodos de análise e técnicas de mapeamento, o que leva à existência de uma multitude de métodos e técnicas de mapeamento que parecem ser diferentes entre si, resultando em informação ambígua e conflituosa no que diz respeito aos mecanismos da FA, e a conclusões distintas entre estudos. O sucesso do tratamento poderia aumentar se tivéssemos uma melhor compreensão dos métodos de análise e da sua aplicação no contexto da FA; perceber se os métodos apontam para o mesmo fenómeno de fibrilhação, se existe alguma correlação entre os métodos, e se a informação fornecida pelos mesmos é complementar ou redundante. Assim, o objectivo deste trabalho consistiu em implementar diferentes métodos para analisar os EGMs e a estrutura 3D da aurícula esquerda (AE) de doentes com FA, numa tentativa de responder às questões que motivaram a realização deste projecto. Em última análise, ao observar os mapas 3D da AE tendo uma melhor compreensão dos métodos, poderemos identificar com precisão as regiões na AE responsáveis por iniciar a FA, e ter mais conhecimento sobre os mecanismos responsáveis pela mesma. Desta forma, o processo de ablação poderá alcançar o seu potencial.

Para este projecto, foram incluídos os mapas 3D electroanatómicos da AE de dez doentes com FA paroxística ou persistente do hospital de Santa Marta, recolhidos com o sistema de mapeamento CARTO 3. Cada ponto electroanatómico dos mapas inclui as 12 derivações do ECG, e os EGMs unipolares e bipolares registados com o cateter de mapeamento Pentaray de 20 pólos. Porém, apenas os EGMs bipolares foram incluídos na análise. Processaram-se os sinais bipolares e, devido a algumas limitações, foi possível apenas a implementação de dois métodos diferentes para os analisar: um no domínio da frequência – Frequência Dominante (FD) –, e outro no domínio da Teoria da Informação – a entropia de Shannon. De seguida, criaram-se três tipos de mapas 3D electroanatómicos da AE para cada doente: um de voltagem, cuja informação foi adquirida com o sistema de mapeamento, um de FD, e outro de entropia. A informação de cada mapa estava organizada segundo um padrão de cores. Observando os diferentes tipos de mapas da AE paralelamente, foi possível comparar os métodos, e

perceber que tipo de informação cada um deles fornecia, numa tentativa de melhor compreender os mecanismos da FA.

Foi possível observar em algumas regiões da AE, principalmente nos mapas de voltagem e de FD, a presença de "centros de activação" ou "centros de fibrilhação", que poderão ser os gatilhos responsáveis por desencadear ou manter o mecanismo de fibrilhação. Para confirmar se de facto aquelas regiões eram os gatilhos de fibrilhação, seria necessário submeter os doentes ao processo de ablação e queimar essas zonas; e posteriormente acompanhar os doentes para observar os efeitos do procedimento e confirmar a hipótese. Contudo, dadas as limitações do trabalho e o facto desta área de investigação ser pouco explorada, é fulcral obter um maior número de estudo comparativos entre mais métodos de diferentes domínios e confirmar se apontam ou não para o mesmo fenómeno de fibrilhação.

Apesar de terem sido implementados apenas dois métodos de análise dos EGMs, o projecto permitiu a comparação entre os mesmos, uma área de estudo por onde ainda há muito para investigar. Com mais conhecimento sobre os diferentes métodos, a sua aplicação, inter-relação e adequação no estudo dos mecanismos da FA e das propriedades electrofisiológicas desta patologia, é possível desenvolver procedimentos de ablação mais eficientes e selectivos, de forma a diminuir os riscos e aumentar a taxa de sucesso do tratamento.

Palavras-chave: Fibrilhação auricular, processamento de sinal, electrogramas intracardíacos, mapas de alta densidade tridimensionais da aurícula esquerda

Abstract

Atrial fibrillation (AF) is the most frequent cardiac arrhythmia in clinical practice and is described by rapid and irregular contractions of the atria. Despite catheter ablation (CA) being a well-established treatment for AF, it is sub-optimal, with a success rate of approximately 50 % after a single procedure, with some patients requiring multiple procedures to achieve long-term freedom from this pathology. This prompted the proposal and development of various quantitative electrogram (EGM)-based methods along with different mapping systems with their respective mapping techniques, to better understand the mechanisms responsible for initiating and maintaining AF, thus improving ablation outcomes. However, this diversification of methods and tools resulted in disperse and inconsistent data regarding the mechanisms of AF.

This work consisted of employing two different methods to analyse the electrograms (EGM): dominant frequency (DF) and Shannon entropy (ShEn). From these EGMs, metrics were then extracted and displayed in colour-coded fashion on a 3D mesh of the left atrium (LA) from patients with paroxysmal or persistent AF. The two methods were compared to understand whether or not these indicated different phenomena/mechanisms, and if these could locate sites suspected of triggering and maintaining AF.

The results, while not fully conforming to the literature, allowed the comparison between different EGM analysis methods, a field of study that requires further research. Overall, this project highlighted the limited data available within the topic, hindering our understanding of AF mechanisms and development of more effective and selective ablation procedures to avoid unnecessary complications, and ultimately improve the effects of the treatment's outcomes.

Keywords: Atrial fibrillation, signal processing, intracardiac electrograms, three-dimensional high-density maps of the left atrium

Table of Contents

List of Figures

List of Tables

List of Abbreviations

3D	three-dimensional
AF	atrial fibrillation
ANS	autonomic nervous system
AP	action potential
AVN	atrioventricular node
b-EGM	bipolar electrogram
CA	catheter ablation
CFAE	complex fractionated atrial electrogram
CL	cycle length
CS	coronary sinus
CT	computed tomography
CVD	cardiovascular disease
DF	dominant frequency
DOAC	direct oral anticoagulants
EAM	electroanatomical mapping
ECG	electrocardiogram
EGM	electrogram
EP	electrophysiological
FFT	fast fourier transform
FIRM	focal impulse and rotor modulation
GP	ganglionated plexi
HD	high density
ICL	interval confidence level
IIR	infinite impulse response
INR	international normalized ratio
LA	left atrium
LAT	local activation time
LIPV	left inferior pulmonary vein
LUPV	left upper pulmonary vein
LV	left ventricle
LVA	low voltage area
LVEF	left ventricle ejection fraction
MRI	magnetic resonance imaging
OI	organization index
PS	phase singularity
PV	pulmonary vein
PVAI	pulmonary vein antral isolation
PVI	pulmonary vein isolation
RA	right atrium
RF	radiofrequency
RFCA	radiofrequency catheter ablation
RI	regularity index
RIPV	right inferior pulmonary vein
ROI	region of interest
RUPV	right upper pulmonary vein
RV	right ventricle

SAN	sinoatrial node
SCL	shortest complex interval
ShEn	Shannon entropy
SR	sinus rhythm
SVC	superior vena cava
u-EGM	unipolar electrogram
WCT	Wilson central terminal
WOI	window of interest

1 Introduction

Cardiovascular diseases (CVD) such as arrhythmias are a leading cause of mortality in the world, totalling 18.6 million fatalities in 2019 [1]. In particular, atrial fibrillation (AF) is the most common sustained cardiac arrhythmia [4], and affects almost 1% of the worldwide population [5]. It is characterized by an uncoordinated, rapid, and irregular electrical activation of the atria [6], [7], resulting in an ineffective atrial contraction [8]. AF is a major cause of mortality and morbidity, as it increases the risk of stroke, heart failure and thromboembolic complications, which impair the patient's quality of life [9], [10]. Due to this condition's severity and magnitude, there has been much interest and investment in procuring methods to identify, analyse, and combat it. One such procedures devised to treat AF is catheter ablation (CA), a well-established treatment for AF in case antiarrhythmic medication fails, and for prevention of AF recurrences. However, as we still do not know for certain the causes and the mechanisms responsible for initiating and sustaining AF, the success rate of this treatment is sub-optimal as it often requires multiple procedures to achieve long-term freedom from AF in some patients [3].

In this perspective, quantitative electrogram (EGM)-based methods have been proposed and different mapping systems have been developed. Some of the most frequently used methods target complex fractionated atrial electrograms (CFAE), high dominant frequency (DF) sites, singularities identified during phase mapping, among others. These all serve to improve the efficacy and outcomes of CA, assist physicians in the decision process, and to better understand the mechanisms of AF. These methods process, extract, and quantify clinically relevant features of the EGM signals recorded in the heart using multi-electrode catheters, either in unipolar or bipolar configurations [11]–[13].

In spite of the great advances, such methods employed by the different mapping systems to terminate AF have not shown significant and additional benefits to the outcomes of CA. This is due to several reasons: 1) different mapping systems have their own algorithms and mapping techniques, and the software is proprietary, so we do not know how the algorithms actually work to compare their similarities and differences; 2) a large portion of the spatiotemporal content of the EGMs is discarded and thus rarely utilised in current clinical practice. This is due to the number of filters that the mapping systems apply to the EGM signals, since they only have algorithms to map and analyse filtered and well characterised signals; 3) no mapping system is able to plot every type of map (CFAE map, DF map, entropy map, etc.), let alone simultaneously. All of this led to the development of a myriad of methods and mapping techniques that may seem different from each system, resulting in disperse and conflicting information regarding the mechanisms of AF.

The main motivation behind this project is to surpass some of the limitations described above and employ different methods to analyse EGM signals and the 3D structure of the heart of patients with AF, and extract metrics that better characterise this disease and understand if: 1) the methods point to the same phenomenon; 2) there is any correlation between the methods; and 3) the information given by the methods is complementary or redundant. Ultimately, by observing the 3D structure of the heart with better signal methods, we could identify sites suspected of triggering AF, annotate them, analyse correlations, and through that knowledge allow for the treatment procedure to reach its full potential and greatly increase its effectiveness.

This project is divided into 5 chapters with the following content: The present chapter is dedicated to give an overview of AF and the contextualisation of the motivation behind this project. Chapter 2 provides a background of the cardiovascular system, as well as the technique used to measure physiological signals evaluated in this project. A background of AF is also given, including its electrophysiological mechanisms, methods, and mapping approaches used to study and analyse the mechanisms responsible for initiating and sustaining AF with the goal of better understanding them and improve the treatment's effectiveness. A brief explanation of the CA procedure is also given. Chapter 3 describes the methodology employed in this study, including a description of the mapping procedure, the clinical mapping data and the patients' clinical characteristics; the algorithms used for pre-processing, processing, and analysing the EGM signals. Chapter 4 gives the discussion of the

results and a critical analysis in comparison to other studies, as well as the limitations of this project. And lastly, chapter 5 concludes the study, and provides a summary of its outcomes and future perspectives.

2 Background

This chapter serves to establish a foundation for the reader in regard to AF, by first providing a background of the cardiovascular system, then the techniques used to measure the physiological signals, which are registered in the electrocardiogram and electrogram, following a description of the electrophysiological mechanisms of AF. Additionally, some methods and mapping approaches, along with the hardware dedicated to the electrophysiological study of AF are also discussed, as well as their limitations. Afterwards, a brief description of the CA procedure is given. This chapter ends with the exposure of the objectives of this project.

2.1 The Cardiovascular System

The primary function of the cardiovascular system is to provide the needs to the body tissues, by transporting nutrients and oxygen, and carrying away waste products and carbon dioxide. It is composed of two closed-loop circuits that originate and return to the heart: the pulmonary and systemic circulations. The pulmonary circulation takes the carbon dioxide-rich blood to the lungs where it is oxygenated, and the systemic circulation supplies oxygen-rich to the entire body and carries out carbon dioxide-rich blood. The heart maintains the flow between the two circuits [14], [15].

2.1.1 Anatomy and Function of the Heart

The heart is a muscular organ located in the middle mediastinum, inside the thoracic cavity, and it is enclosed in a two-layer thin membrane, called the pericardium [15], [16]. As illustrated in figure 2.1, it is composed of four chambers that can be segregated into the left side and the right side, each containing an atrium and a ventricle that together form the left and the right pumps, respectively. The right pump is responsible for collecting carbon dioxide-rich blood and pumping it to the lungs for blood oxygenation. From there, oxygenated blood flows to the left pump to be distributed to the body tissues. Within each side, the atrium serves as a volume reservoir for blood coming from the systemic (right atrium (RA)) or the pulmonary (left atrium (LA)) system circuit, before pumping it to the ventricle; and the ventricle collects blood from the atrium and pumps it out of the heart [15], [17].

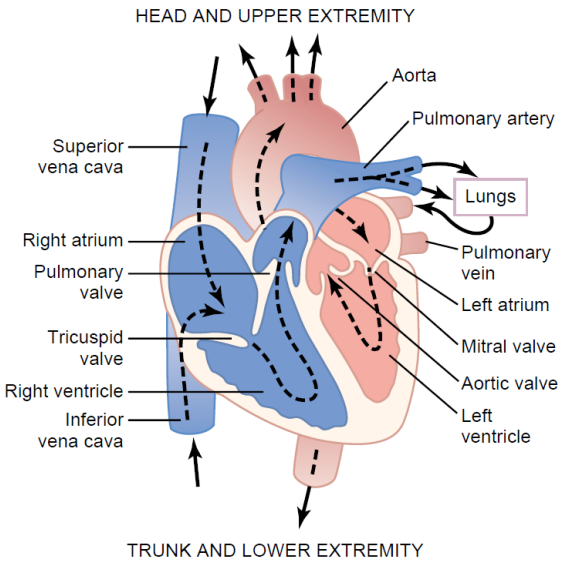

Figure 2.1: Anatomy of the heart, and circulation of blood flow through the heart chambers and heart valves. Adapted from [14].

2.1.2 Electrical and Mechanical Activity of the Heart: The Cardiac Cycle

At a cellular level, the heart is formed by highly specialized myocytes responsible for both electrical impulse conduction and mechanical contraction [18]. Like other cell types, the membrane bilayer of these cardiac muscular cells contains a collection of transmembrane proteins, called ion channels, allowing ions to move across the membrane, important in the generation of action potentials. The major ions that are present in the intra and extracellular media of the myocytes are sodium (Na^+), potassium (K^+), calcium (Ca^{2+}), and chloride (Cl^-); and they play a role in the resting membrane potential of these cells [15].

A cardiac cycle is a repeated rhythmic event initiated from impulses generated within the myocytes. Each cycle is composed of electrical and mechanical contraction (systole) and relaxation (diastole) [19].

At the beginning of the cardiac cycle, in the early phase of ventricular diastole, all four chambers are relaxed (ventricular and atrial diastole), allowing blood to empty the veins into the atria. Because the pressure in the ventricles fall below that in the atria, the tricuspid and mitral valves (atrioventricular valves) open, causing passive filling of the ventricles. Near the end of ventricular diastole, both atria start to contract (atrial systole), augmenting ventricle filling. Then, the atrioventricular valves close and the pulmonary and aortic valves (semilunar valves) open when the ventricles contract (ventricular systole), ejecting blood into circulation. Simultaneously, the atria are relaxed (atrial diastole), and afterwards the ventricles enter their diastolic phase, initiating a new cardiac cycle [15].

An action potential (AP) is the rapid change in the membrane potential that results from ion electrochemical interactions between the extracellular and intracellular media, leading to the mechanical contraction of the myocyte. Depolarization is the rising of the transmembrane voltage above the resting potential, and its return to the resting potential is referred to repolarization [14].

The cardiac AP has five phases illustrated in figure 2.2:

- Phase 4 corresponds to the resting potential, where the transmembrane potential remains stable at ≈ -90 mV throughout the diastolic period [20]. During rest, the cell membrane is permeable to K^+ and relatively impermeable to Na^+ and Ca^{2+} [21].

- Phase 0 is the phase of rapid depolarization [20]. Inflow of Na^+ and Ca^{2+} lead to an increase of the membrane voltage over the threshold potential (approximately -65 mV), initiating an AP [18], [19].

- Phase 1 is the phase of early repolarization. The Na^+ inward current is quickly inactivated, followed by a subsequent outward K^+ and Na^+/Ca^{2+} exchanger currents, initiating rapid membrane repolarization [19], [22].

- Phase 2, the plateau phase. It is unique among excitable cells [20] and it is characterized by the balance of Ca^{2+} inward currents, Na^+ currents, and hyperpolarizing outward K^+ currents [22].

- Phase 3 is the phase of rapid repolarization, where the resting potential of the membrane is restored [20] as a result of the inactivation of Ca^{2+} inward currents and the dominant K^+ outward currents [22].

During an AP, the already excited area of cardiac muscle is unable to get re-excited, regardless of the strength of the stimulus, as it is refractory to restimulation [14], [19]. The refractory period of the heart is called absolute refractory period and it occurs immediately after phase 0 and during phase 2 to allow the recovery of the cardiac cells and prevent multiple APs [19]. The normal refractory period of the ventricle is 250 ms to 300 ms, and of the atrium is 150 ms. Through phase 3, there is an additional relative refractory period that lasts 50 ms and only stronger-than-normal stimuli can activate the cardiac muscle [14], [19].

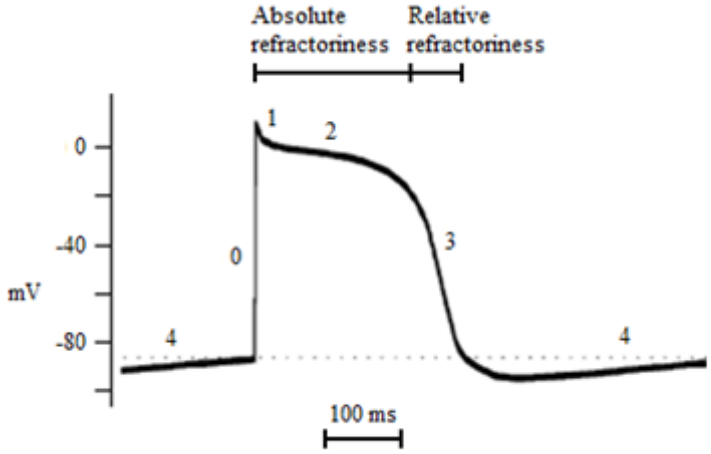

Figure 2.2: Illustration of the phases of the AP on a His Purkinje cell, including the refractory periods. The dashed line represents the threshold potential. Adapted and modified from [23].

2.2 The Electrocardiogram

The heart has a specialized electrical conduction system, composed of pacemaker cells, responsible for generating and conducting electrical impulses in a rapid and highly coordinated fashion to the cardiac myocytes for a rhythmical and synchronized contraction of the heart (see figure 2.3(a)). The normal rate of the heart, known as sinus rhythm (SR), is between 60 and 100 beats per minute [14], [15].

The electrocardiogram (ECG) is the graphical representation of the electrical cardiac activity during a heartbeat recorded by electrodes attached to the surface of the skin [17], [24]. To record an ECG waveform, a differential recording between two points on the body, referred to as a lead, is made [25].

The normal ECG shows a set of waveforms that represent the different phases of the cardiac cycle (figure 2.3(b)). The information regarding the waveforms' morphology and timing is used to diagnose diseases that are reflected by disturbances of the heart's electrical activity [26].

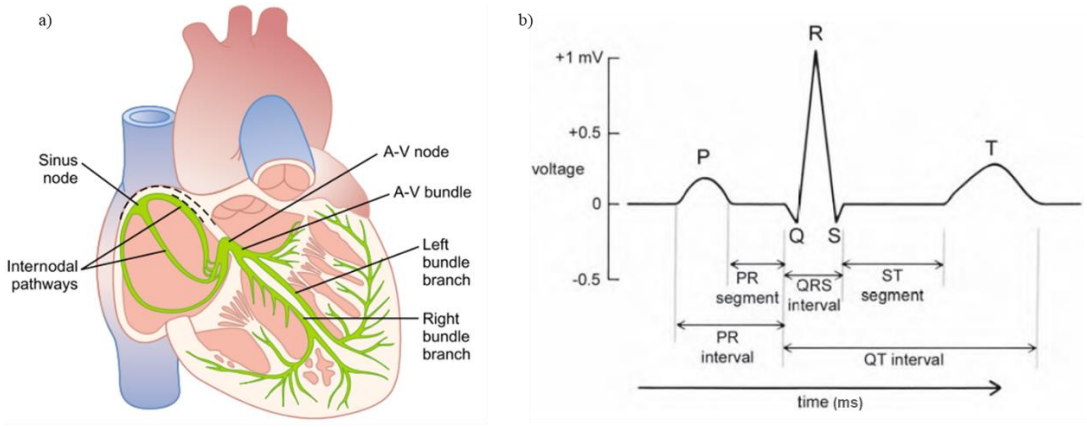

Figure 2.3: Electrophysiology of the normal heart during SR: a) the electrical conducting system of the heart (adapted from [14]), and b) an ECG waveform of a normal cardiac cycle measured from the lead II (adapted and modified from [15]).

During normal SR, in the diastole phase, the cardiac cycle begins with the electrical impulse generated in the sinoatrial node (SAN), a collection of cardiac myocytes located in the superior lateral wall of the RA that acts as the intrinsic cardiac pacemaker. When initiated, the impulse travels through the internodal pathways, reaching the atrioventricular node (AVN) located in the posterior wall of the RA immediately behind the tricuspid valve, and consequently depolarizing first the RA, then the LA, before contraction of both chambers. The atrial depolarization is represented by the P-wave on the surface ECG [14], [15].

The AVN prevents the impulse from travelling too quickly from the atria to the ventricles. This delay allows ventricular blood filling that was accumulated in the right and left atria as they mechanically contract; represented by an electrically silent period after the P-wave. Afterwards, the impulse resumes the rapid conduction through the bundle of His (divided into the right and left bundle branches supplying each ventricle, respectively), and the His-Purkinje system, reaching each ventricle, depolarizing it. The ventricular depolarization is represented in the surface ECG by the Q, R, and S waves, together known as the QRS complex. Simultaneously, the atrial contraction has ended, and atrial repolarization begins (systole) [14], [15].

The cardiac cycle ends with the ventricular repolarization (diastole) represented by the T wave in the surface ECG, and another one begins anew.

The most commonly used ECG recording configuration in clinical practice is the 12-lead ECG system [26], and it is composed by three different sets of electrodes: three bipolar limb leads – I, II, III; three augmented unipolar limb leads: augmented vector right (aVR), augmented vector left (aVL), and augmented vector foot (aVF); and six precordial unipolar leads: V1, V2, V3, V4, V5, and V6 (see figure 2.4(a) – (b)).

The bipolar leads form a configuration around the heart known as Einthoven's triangle, providing a frontal plane view of the heart's activity in 60° orientation gaps [17]. Each lead is obtained as followed [25]:

$$I = V_{\mathrm{LA}} - V_{\mathrm{RA}} \tag{2.1}$$

$$II = V_{\mathrm{LL}} - V_{\mathrm{RA}} \tag{2.2}$$

$$III = V_{\mathrm{LL}} - V_{\mathrm{LA}} \tag{2.3}$$

where V_{LA}, V_{RA}, and V_{LL} are the potentials from the electrodes placed on the left arm, right arm, and left leg (foot), respectively.

The augmented unipolar limb leads provide further information of the heart's frontal plane view [17]. Each augmented lead is given by the voltage difference between each vertex of the triangle and the average voltage of the remaining two vertices [25]:

$$aVR = V_{\mathrm{RA}} - \frac{V_{\mathrm{LA}} + V_{\mathrm{LL}}}{2} \tag{2.4}$$

$$aVL = V_{\mathrm{LA}} - \frac{V_{\mathrm{RA}} + V_{\mathrm{LL}}}{2} \tag{2.5}$$

$$aVF = V_{\mathrm{LL}} - \frac{V_{\mathrm{LA}} + V_{\mathrm{RA}}}{2} \tag{2.6}$$

The unipolar precordial leads are placed in sequence across the chest, on the front and left sides, and provide a more detailed view of the heart [14], [26]: leads V1 and V2 primarily reflect the activity of the RV; leads V3 and V4 show the anterior wall of the LV, and V5 and V6 its lateral wall. The precordial leads record voltages between each of the precordial wires and the Wilson central terminal (WCT). The WCT is defined as the average voltage measured on the right and left arms and the left leg, and is assumed to be at the center of a triangle with the 3 limb wires at the apices [26], [27]:

$$V_{\mathrm{WCT}} = \frac{V_{\mathrm{LA}} + V_{\mathrm{RA}} + V_{\mathrm{LL}}}{3} \tag{2.7}$$

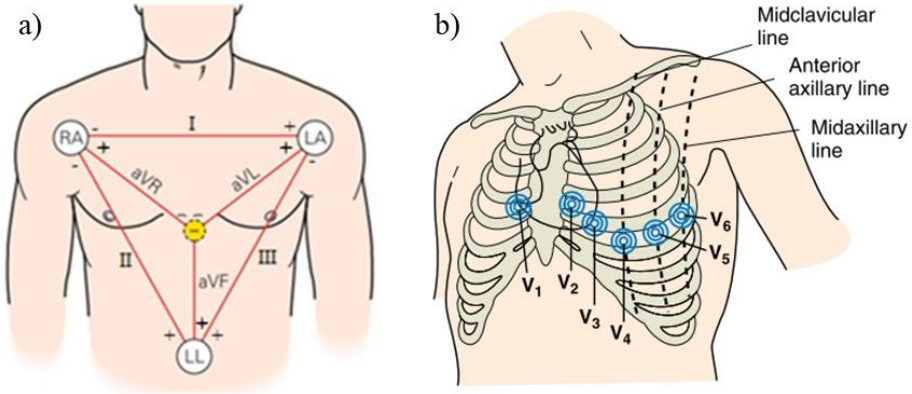

Figure 2.4: Electrode location of the 12-lead ECG system: a) unipolar and bipolar leads electrode location and b) unipolar precordial leads electrode location. Adapted and modified from [28].

2.3 The Intracardiac Electrogram

Whereas the surface ECG represents a summation of the electrical activity of the entire heart, the intracardiac electrogram (EGM) records the electrical activity of the local cardiac tissue using a multipolar catheter directly in contact with the myocardial tissue [23], which is inserted percutaneously, through the femoral vein.

An EGM corresponds to the voltage difference recorded between two recording electrodes during the cardiac cycle [23], [29], and it is recorded with amplifiers that have high-input impedances to decrease unwanted electrical interference and ensure high quality recordings. Filtering is also an important step to eliminate far-field noise, typically at 30 to 500 Hz. Far-field signals correspond to signals that do not originate in the recorded local myocardium, but instead in an adjacent myocardial tissue. EGMs can provide three types of information: 1) the activation time of the myocardium; 2) the

direction of propagation of electrical activity activation within the field of view of the recording electrode; and 3) the complexity of myocardial activation within the field of view of the recording electrode [23].

There are a few types of EGM recording, but the most common ones are the unipolar and the bipolar configurations, which are discussed below.

2.3.1 Unipolar Electrogram

A unipolar electrogram (u-EGM) represents the potential difference between an exploring electrode positioned in the heart and a second electrode (referred to as the indifferent or reference electrode) distant from the heart (theoretically at infinite distance) so that little or no cardiac signal is recorded [24], [30], [31]. Most clinical recording systems have the option to select a unipolar recording mode that connects the reference electrode to the WCT to reduce electrical noise, with the exploring electrode being the distal electrode of a mapping catheter [24], [27], [30]. Alternatively, noise may also be reduced by connecting a reference electrode in the inferior vena cava [30]. Figure 2.5(a) illustrates a setup of the indifferent electrodes for unipolar recordings.

The conventional configuration has the exploring electrode connected to the positive input of the recording amplifier and the reference electrode to the negative input. Thus, when a depolarization wavefront approaches the exploring electrode, it creates a positive deflection that quickly reverses itself into a negative deflection as the wavefront passes under the electrode and moves away from it, generating a RS complex as shown schematically in figure 2.5(b) [23], [24], [31].

In healthy cardiac tissue, the maximum negative slope (dV/dt) of the u-EGM signal coincides with phase 0 of the AP, corresponding to the rapid Na^+ intake, and thus with the depolarization of cardiomyocytes (or local activation time (LAT)) directly beneath the electrode [23], [31], [32]. The dV/dt of the u-EGM is considered the most accurate marker of local tissue activation [32].

The unipolar recording provides information about the direction of impulse propagation, as it is dependent on wavefront origin: positive deflections (R waves) are generated by propagation toward the recording electrode, and negative deflections (QS complexes) are generated by propagating away from the electrode [23], [24], [31].

Although unipolar recordings can provide an indication of the direction of wavefront propagation and a more precise measure of the timing of local activation, they are less preferred to be used in clinical practice than bipolar recordings because the former contain substantial far-field signals generated by electrical depolarization of remote tissue from the recording electrode and are susceptible to electrical noise. This happens because u-EGMs record all events occurring between electrodes [23], [24], [32], [33]. Another issue in particular with atrial EGMs is the overlap with ventricular electrical activity [13].

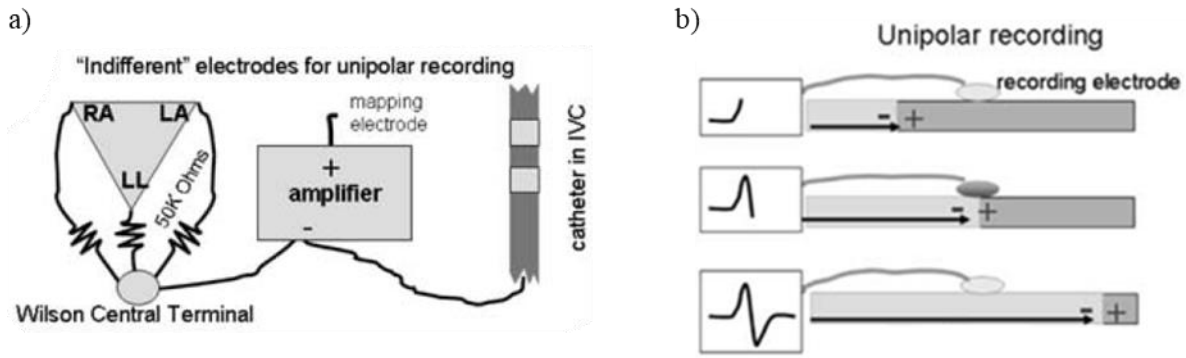

Figure 2.5: Unipolar recordings for clinical electrophysiology: a) indifferent electrode configurations for unipolar recordings, and b) generation of u-EGMs. From the top schematic, since by convention the exploring electrode is connected to the positive input of the recording amplifier, as the wavefront propagates toward the exploring electrode, it generates a positive deflection. As the wavefront propagates away the recording electrode, a negative deflection is generated (middle and bottom schematics). Adapted from [30].

2.3.2 Bipolar Electrogram

A bipolar electrogram (b-EGM) represents the potential difference between a pair of connected electrodes to the recording amplifier, placed at the site of interest, and it corresponds to the difference between the two u-EGMs recorded at the two poles of a multipolar catheter, as long as the two unipolar electrodes are close to each other and placed at the same site, as shown in figure 2.6(a). Given that the far-field signal recorded at the two electrodes is similar at each point in time, it is largely subtracted out, leaving the local signal [23], [30]. This is notable in bipolar electrodes with short interpolar distances [23]. Consequently, b-EGM recordings offer a better signal-to-noise ratio and allow a better identification of local depolarization, especially in abnormal areas of infarction or scar [23], [24], [30]. These areas are characterized by multiple sharp deflections that are obscured in unipolar recordings and are associated with asynchronous activation of multiple myocyte bundles [29]. Hence, bipolar recordings are used to locate focal arrhythmias by identifying the point of earliest activation relative to a stable reference, and overall, they are preferred for catheter mapping in humans and particularly for scar-related arrhythmias. However, it is important to note that the precision of locating the source of a particular electrical signal is dependent on the distance between the recording pair of electrodes [30].

In a homogeneous conducting tissue, the initial peak of the b-EGM coincides with depolarization beneath the recording electrode and corresponds to the maximal negative dV/dt of the u-EGM [23], [29], thus it is usually used as a fiducial LAT marker in bipolar recordings [33]. However, and especially when considering a complex activation, there is no consensus regarding the choice of marker on b-EGMs to assess the LAT (see figure 2.6(b)) [24], [32]. Therefore, b-EGMs lack directionality features when comparing to u-EGMs. Additionally, several factors affect b-EGMs' morphology and amplitude, including wavefront direction, the angle between the recording pair of electrodes, electrode size, inter-electrode spacing, direction of propagation of the wavefront with respect to the bipolar recording axis, among others [23], [24], [32], [33].

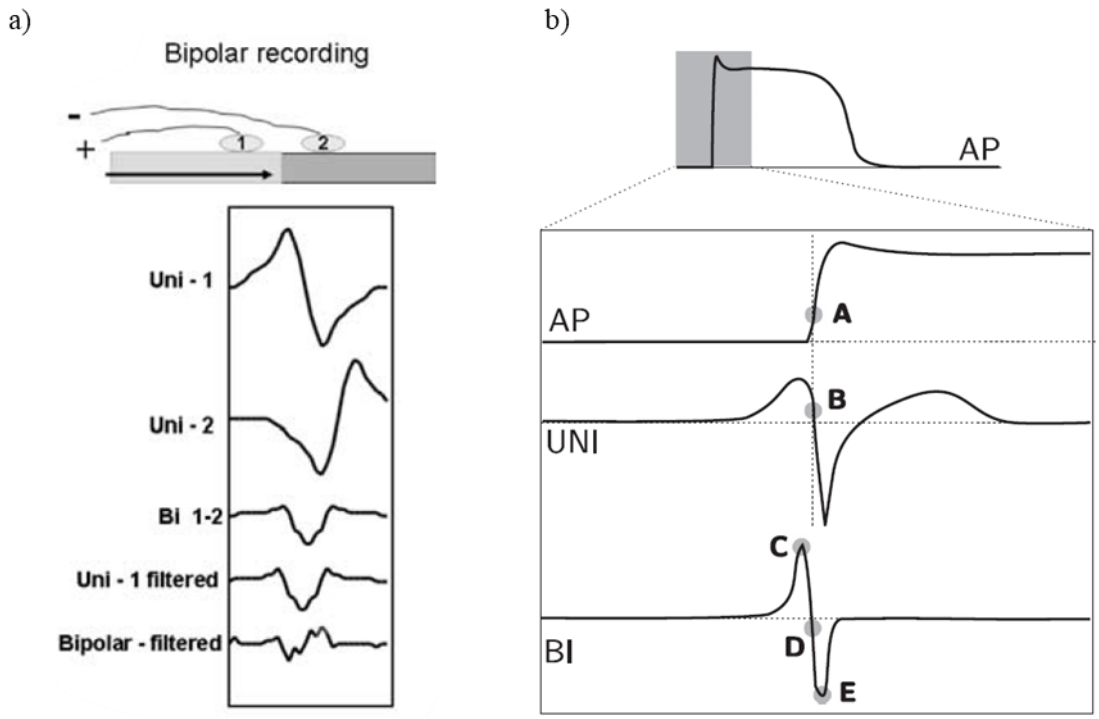

Figure 2.6: Bipolar recordings for clinical electrophysiology: a) generation of b-EGMs. Electrode 1 and electrode 2 are connected to the positive and negative inputs of the recording amplifier, respectively. The wavefront first reaches electrode 1 (Uni-1) and then electrode 2 (Uni-2), making Uni-2 signal slightly delayed compared to the Uni-1 signal. Uni-2 is inverted because it is attached to the negative input of the recording amplifier. Adding these two signals together generates the bipolar signal (Bi 1–2), removing much of the far-field signal. High pass filtering is simulated by numerically differentiating the signal with respect to time. Differentiating the Uni-1 signal decreases the far-field component and produces a signal quite similar to the bipolar signal but slightly shifted with respect to time (image from [30]); and b) location of commonly used activation times in the literature for AP, extracellular unipolar (UNI), and bipolar (BI) EGMs. (A) maximum dV/dt, (B) maximum negative dV/dt, (C) maximum absolute voltage $|V|$, (D) maximum absolute slope $|\mathrm{d}V/\mathrm{d}t|$, and ((E) minimum voltage (adapted from [32]).

2.2 Atrial Fibrillation

Atrial fibrillation (AF) is a supraventricular tachyarrhythmia characterised by rapid and irregular activations of the atria, at a rate between 350 and 600 beats per minute [23]. A characteristic ECG of AF, illustrated in figure 2.7, is described by the absence of the P-wave, as it is substituted by fibrillatory or f waves, and irregular ventricular rhythm [8], [34], [35].

AF is the most common cardiac arrhythmia in clinical practice, with approximately one third of hospitalizations. Estimates point for 2.3 million people in the United States and 4.5 million in the European Union with paroxysmal or persistent AF [23]. Its prevalence increases with age, affecting 5% of people older than 65 [37], and over 10% of those above 80 years old [5].

The type of AF is classified according to the temporal pattern of the arrhythmia: after detecting the first episode of AF, if a patient has two or more episodes, then AF is considered recurrent. The disease progresses to paroxysmal if the episodes terminate spontaneously, usually within seven days. When the episodes extend more than a week and medical intervention is required to cease the arrythmia, AF is considered to be persistent. It can become permanent if electrical cardioversion has failed or not indicated to restore SR [4], [8].

Catheter ablation (CA) is a well-established treatment for AF when antiarrhythmic medication fails, and for prevention of AF recurrences. While CA is capable of terminating AF, the overall success rate is only around 50% after a single procedure in paroxysmal AF patients and less than 50% in

nonparoxysmal patients. When performing multiple procedures, the success rate increases up to 80% [3].

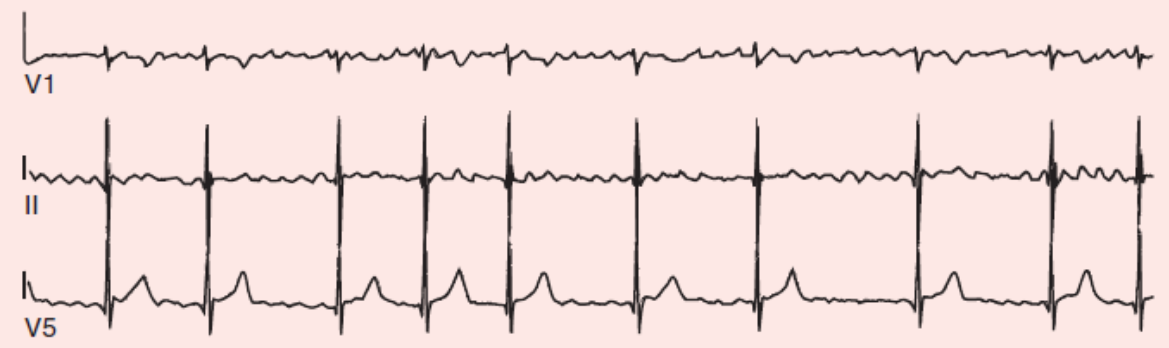

Figure 2.7: Example of an ECG recording during AF. From top to bottom: leads V1, II, and V5, respectively, showing f-waves and irregular ventricular rhythm. Adapted from [34].

2.3 Electrophysiological Mechanisms of Atrial Fibrillation

The existence of two concepts of the underlying mechanisms of AF have been taken into consideration: 1) mechanisms responsible for its initiation, triggers and 2) mechanisms responsible for sustaining it, substrates [9], [10], [23], [38]. Although not fully understood yet, it is generally accepted that the development of AF results from the interaction and interplay between both types of mechanisms [6], [18], [23], [38]. While a trigger is a rapidly firing focus that can act as an initiator for the arrythmia, a substrate corresponds to electrical, mechanical, and anatomical characteristics of the atria that sustain AF. The development of this substrate usually includes both electrical and structural elements of atrial remodelling [39], including slowed conduction velocity, altered electrical excitability, and development of scarring (fibrosis) that acts as a barrier to electrical propagation in the atrial tissue [13]. Over time, AF progresses from a trigger-driven to a substrate-mediated arrhythmia as a consequence of these remodelling elements of the atria [40].

2.3.1 The influence of the Autonomic Nervous System and the Ganglionated Plexi

The importance of the cardiac autonomic nervous system (ANS) has been recognized in the setting and development of arrythmias, including AF [41]–[43].

The heart is innervated by the extrinsic and intrinsic cardiac ANSs, both important for cardiac function and arrhythmogenesis [42]. The extrinsic cardiac ANS includes fibers that mediate connections between the heart and the nervous system, whilst the intrinsic cardiac ANS consists of primarily autonomic nerve fibers inside the heart, including an extensive epicardial neural network of nerve axons, interconnecting neurons, and clusters of autonomic ganglia, known as ganglionated plexi (GP) [41], [44].

In contrast to ventricular GP, the atrial GP are concentrated in different locations on the chamber walls. A particular region of the atria that contains a high density of GP and is highly innervated by the ANS is the pulmonary vein-left atrium junction, each one innervating one of the four PVs and the surrounding atrial myocardium [41], [44]. The GP connect the extrinsic and intrinsic components of the ANS [44], and are important mediators of electrophysiological effects of the heart responsible for initiating AF [38], [44].

2.3.2 AF Triggers

In 1998, Haïssaguerre et al. first demonstrated the role of the PVs to be the underlying mechanism of most paroxysmal AF. In their study, they were able to identify triggering foci of rapidly firing cells within the sleeves of atrial myocytes extending into the PVs; ablation of these ectopic foci was able to reduce AF recurrence [45].

The anatomical and electrophysiological properties of the PVs that may present a predisposition for arrhythmogenesis were assessed in following studies [46]–[50]. The myocardial sleeves within the PVs appear to demonstrate key differences from the remaining atrial myocardium in terms of cellular electrophysiology [48], anatomy, and fiber geometry [51], as the PV myocytes present unique electric properties and a complex fiber arrangement. These differences may well promote reentry and ectopic activity not only to initiate, but also maintain AF [46], [47], [52].

Nowadays, the PVs are well established as the primary sources of triggers in paroxysmal AF, as well as their contribution to the maintenance of AF [6], [18]. Hence, the PVs are the main targets of CA, this approach being known as pulmonary vein isolation (PVI) [6], [39]. The PVI approach consists of electrically isolating the PVs from the rest of the LA and performing linear lesions around the antrum of the PVs [8]. Though the clinical outcome of this procedure has yielded good results for patients with paroxysmal AF, its efficacy was much lower for patients with persistent AF [53]. Furthermore, ablation of the GP has been used in addition to PV isolation, giving better results compared to linear lesion together with PVI [54]. Additional triggering foci responsible for initiating AF have been identified outside the PVs, including the coronary sinus (CS), the ligament of Marshall, the superior vena cava (SVC), among others [9], [18], [23], potentially due to the presence of myocardial sleeves or regional atrial fibrosis at these sites [39].

2.3.3 Arrhythmic Mechanisms Sustaining AF

The underlying mechanisms regarding substrates are still debated and how they interact with the ANS. Additionally, the mechanisms that sustain AF may evolve over time as AF progresses from paroxysmal to persistent and permanent forms, due to structural and electrical atrial remodelling [38].

Multiple Wavelet Hypothesis

In 1959, Moe and Abildskov argued that, although the circus movement and ectopic focus theories were plausible to explain AF initiation, these mechanisms were inadequate to explain its perpetuation because they would not be endowed with sufficient stability to persist for years as fibrillation frequently does. Based on their results, they hypothesized that, rather than reentry waves that return to some initial starting point, AF is sustained by multiple randomly wandering wavelets that 1) collide with each other and extinguish if the tissue has reduced excitability, or 2) maintain themselves and/or divide into daughter wavelets if they propagate through tissue of adequate excitability, continually reexciting the atria (see figure 2.8) [55]. Therefore, the maintenance of AF is dependent on the number of wavelets present in the heart, and this depends on the atrial mass, refractory period, conduction velocity, and anatomical obstacles in different portions of the atria. Essentially, a large atrial mass endowed with short refractory periods and conduction delay would yield increased wavelets and would present the most favourable condition to sustain AF [23].

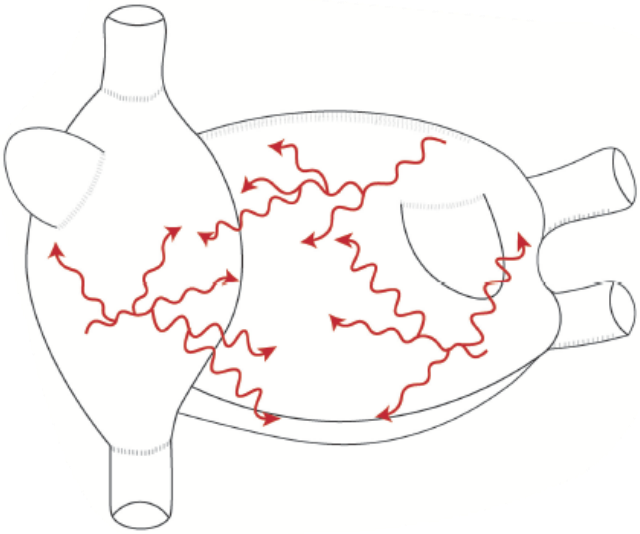

Figure 2.8: Multiple wavelet hypothesis: multiple waves propagate randomly and give birth to new daughter wavelets. Adapted from [9].

Localized or “reentrant” sources

An alternative hypothesis postulates that AF is maintained by predominantly localized or “reentrant” sources. During normal electrical activity, each cardiac cycle begins with an electrical impulse generated in the SAN and propagates until the entire heart is activated. Physiological excitation waves vanish spontaneously after the entire heart has been activated because of the long refractory period in the cardiac tissue compared with the duration of the excitation period; thence the impulse, having no place to go, extinguishes and must be restarted anew. However, if a group of fibers has not been activated during the initial wave of depolarization, they can serve as a link to reexcite areas that were just depolarized and have already recovered from the initial depolarization. Consequently, the impulse will propagate continuously instead of extinguishing itself and will continue to excite the heart as it will always encounter excitable tissue (see figure 2.9). Such process is known as reentry [18], [23], [34]. Reentry can be divided in two groups: anatomic and functional reentry.

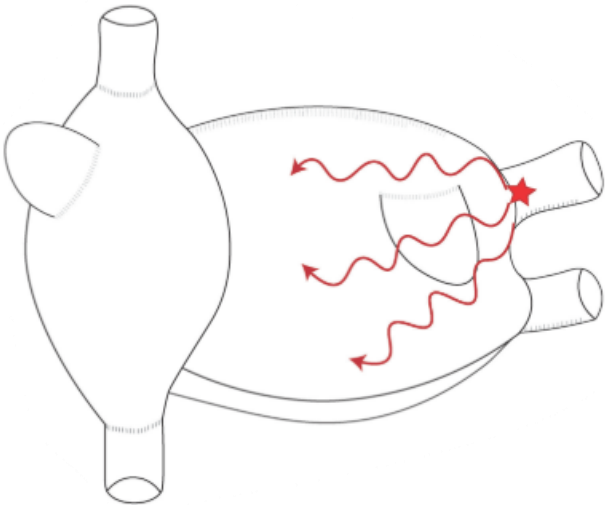

Figure 2.9: Localized or "reentrant" sources: single stable focal or reentrant source (star) with fibrillatory conduction. Adapted from [9].

Anatomic Reentry

In anatomically reentry mechanism, an inexcitable anatomical obstacle creates a surrounding circular pathway in which the wavefront can “reenter”, creating fixed and stable reentrant circuits. The anatomic obstacle determines the presence of two pathways, as shown in figure 2.10(a). When the excitation wavefront encounters the obstacle, it will travel down one pathway (unidirectional block), propagating until the point of block, creating a circus movement. The initiation and maintenance of this circuit is dependent on the conduction velocity and refractory period of each pathway, which in turn determines the extension of the refractory zone behind the excitation wave, called wavelength of excitation (wavelength = conduction velocity × refractory period). For reentry to occur, the wavelength must be shorter than the length of the reentrant pathway. This path length corresponds to a zone of excitable tissue that exists between the head of the reentrant wavefront and the tail of the preceding wavefront, known as the excitable gap, illustrated in figure 2.10(b). The presence of this gap allows the reentrant wavefront to continue propagation around the circuit. Conditions that promote decreased conduction velocity or shortened refractory period allow the creation of smaller circuits, aiding the initiation and maintenance of reentry [18], [23]. Such conditions are commonly encountered in patients with AF, primarily in the presence of fibrosis [9].

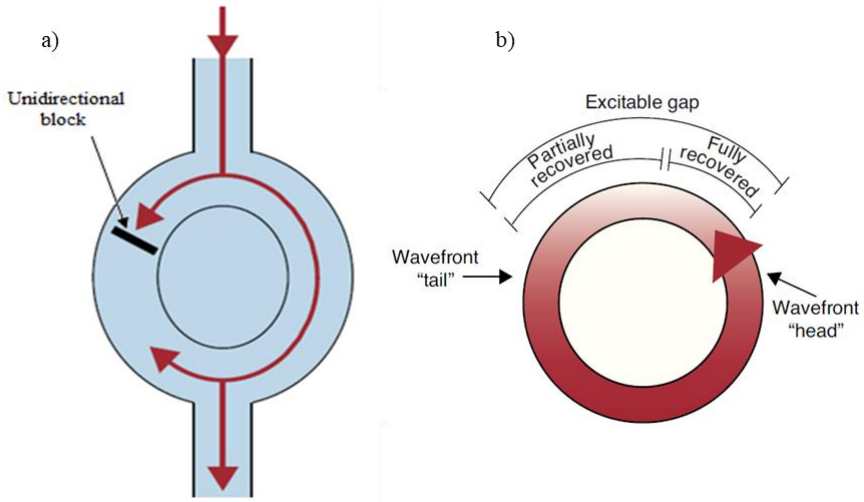

Figure 2.10: Anatomic reentry: a) the central obstacle creates pathways; when the impulse arrives, unidirectional block occurs and slow conduction through the other path allows reentry, and b) schematic representation of an excitable gap. Adapted and modified from [18].

Functional Reentry

In functionally determined circuits, the reentrant pathway depends on the intrinsic heterogeneity of the electrophysiological properties of the myocardium, and not on anatomical obstacles, as illustrated in figure 2.11. Such heterogeneity includes dispersion of excitability or refractoriness and conduction velocity, as well as anisotropic conduction properties of the myocardium. The location and size of functional reentrant circuits can vary, but in general, they tend to be small and unstable. Functional reentrant circuits can be associated with ordered reentry, where the circuit remains in the same place, or random reentry, where it changes size and location; and can occur due to different mechanisms, including the leading circle type of reentry, anisotropic reentry, and spiral wave reentry [18], [23].

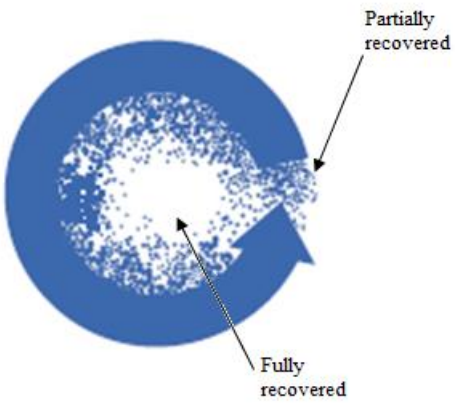

Figure 2.11: Functional reentry: the rate is as rapid as it can be and still allow all portions of the circuit to recover. The dots indicate partial recovery. Adapted and modified from [23].

The Leading Circle Model

The Leading Circle Model was formulated by Allessie and colleagues in 1976 as their experimental studies in rabbit atrial myocardium suggested that the involvement of an anatomical obstacle was unlikely, and instead the sustained tachycardia was completely defined by the electrophysiological properties of the fibers composing the circuit in which the impulse propagated. This model was defined as "the smallest possible pathway in which the impulse can continue to circulate" and "in which the stimulating efficacy of the circulating wavefront is just enough to excite the tissue ahead which is still in its relative refractory phase". Hence, "the head of the circulating wavefront is continuously biting in its own tail of refractoriness". In other words, the premature impulse responsible for initiating reentry blocks in fibers with long refractory periods and conducts in fibers with shorter refractory periods eventually returns to the initial region of block after excitability has recovered there. Then, the impulse continues to circulate around a functionally determined region of inexcitable tissue or a central refractory core and amongst neighbouring fibers with distinct electrophysiological properties. The tissue within the core is kept in a state of refractoriness by constant centripetal bombardment of wavelets/impulses from the circulating wavefront that travel through partially refractory tissue [56]. Because the length of the reentrant pathway is equal to the wavelength of the impulse, there is usually no fully excitable gap, as illustrated in figure 2.12. Due to the absence of a fully excitable gap, this form of reentry is less susceptible to resetting, entrainment, and termination by premature stimuli and pacing maneuvers [23].

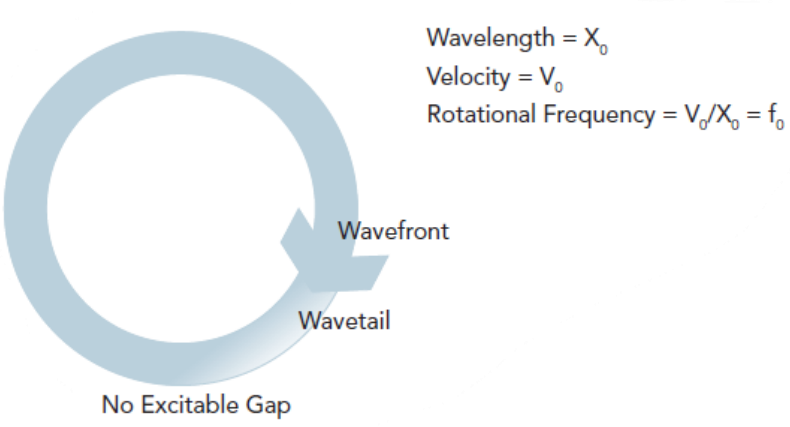

Figure 2.12: Leading circle reentry: no excitable gap is present, and the circuit rotates with a frequency of f0. Adapted from [38].

Anisotropic Reentry

Anisotropy is the normal feature of the cardiac muscle and is related to the differences in longitudinal and transverse conduction velocities, which are determined by the structural organization of the myocardial fibers, including their orientation and the nonuniform distribution of gap junctions. The heterogeneity in conduction velocities and repolarization properties of the cardiac tissue can lead to blocked impulses and slowed conduction that allow reentry even in small anatomical circuits. The key functional characteristic in this type of reentry is the difference in effective axial resistance to impulse propagation dependent on fiber direction. Rather than a circular shape, anisotropic circuits are elliptical or rectangular due to the directional differences in conduction velocities [18], [23]. Figure 2.13 shows a schematic of anisotropic conduction.

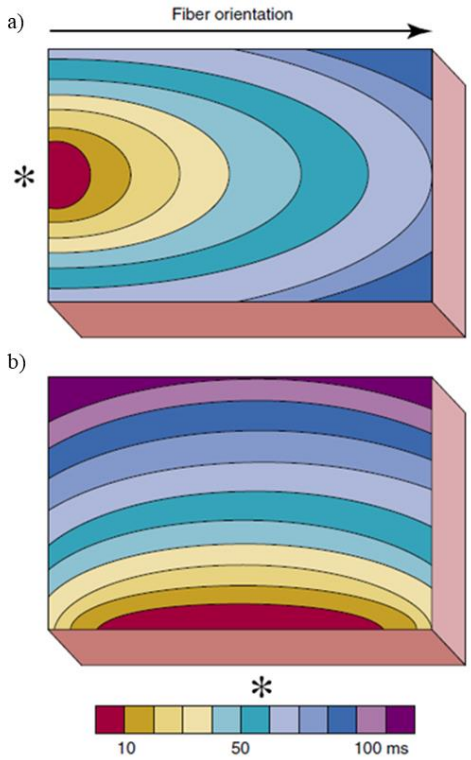

Figure 2.13: Progression of activation wavefronts in myocardial tissue in relation to the longitudinal fiber orientation: a wavefront stimulated (*) at the left edge progresses more rapidly a), than one starting perpendicularly b), because of more favourable conduction parameters in the former direction, such as a wider isochrone spacing. Adapted from [23].

Spiral Wave (Rotor) Reentry

Spiral wave (rotor) reentry corresponds to a specific type of functional reentry, where the wavefront has a curved or spiral form, meeting the wavetail at a focal point, the phase singularity (PS), shown in figure 2.14. The wavefront velocity in a rotor is not constant, as it depends on the wavefront curvature, resulting in slow conduction and block [18]. Because PS corresponds to the region of highest curvature and slowest wavefront conduction velocity simultaneously, the propagating wavefront is unable to invade a core of tissue in the centre of the rotor, being effectively unexcitable. These properties allow rotors to move through space and meander in complex forms, having important effects on their behaviour and sustainability [38].

The rotor model maintains that, while AF shows to be a chaotic and disorganised rhythm, it is continually driven by the organised activity of some high frequency reentrant circuits. These circuits produce wavefronts that eventually degenerate into chaotic and fibrillatory atrial activity at a distance. This is also supported by mapping studies demonstrating the existence of localised, organised drivers in AF, a few of which are thought to represent rotor-like activity [38].

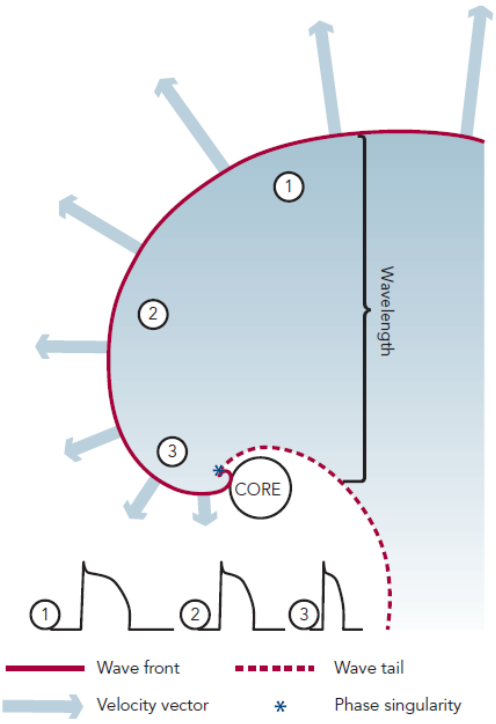

Figure 2.14: Schematic of a rotor: points 1-3 represent the gradient of AP duration along the curvature of the rotor. Adapted from [38].

Complex Fractionated Atrial Electrograms

Many authors have also suggested that complex fractionated atrial electrograms (CFAEs) potentially represent AF substrate sites [57], [58], and that ablating them may terminate AF and prevent its re-induction or recurrence [38]. These are typically low voltage atrial EGMs, ranging from 0.04 to 0.25 mV [59], and patients with persistent and permanent AF tend to have greater number and locations of sites with CFAE compared with paroxysmal AF [60]. Therefore, PVI is usually not sufficient to eliminate persistent AF, and additional ablation on substrates is necessary [34].

CFAEs were first defined by K. Nademanee et al. as: 1) Atrial electrograms that are fractionated, composed of two deflections or more, and/or have a perturbation of the baseline with continuous deflection from a prolonged activation complex or; 2) atrial electrograms with very short cycle, less than 120 ms, with or without multiple potentials; however, when compared to the rest of the atria, this site has the shortest cycle length (p. 981) [59]. The former can be caused by multiple mechanisms, but mainly represent slowed, dyssynchronous, and/or anisotropic local conduction due to separated or disorganised myocardial fibers in the myocardium. In human AF, this may be caused by local collision of multiple wavelets, zones of slow conduction, local reentry and areas adjacent to high frequency sites, where autonomic innervation occurs or is directed by wavebreak and fibrillatory conduction [38]. Figure 2.15 illustrates examples of CFAEs in different regions of the heart.

Figure 2.15: Examples of CFAEs from different regions of the heart. From top to bottom: CS os: coronary sinus ostium, LA: left atrium, LIPV: left inferior pulmonary vein, and RSPV: right superior pulmonary vein. Adapted from [61].

2.4 Electrophysiological Study of Atrial Fibrillation

Electrocardiography is the primary tool for diagnosis and quantification of AF [6]. When a patient is suspected of having or has a clinical history of a cardiac arrhythmia, an electrophysiological study is performed to confirm the type of arrhythmia, its mechanisms, and origin point. This information is later used to determine the best approach of treatment. An electrophysiological (EP) study is an invasive procedure that makes use of multipolar catheters in contact with the cardiac chambers to register the local electrical activity in different points through an intracardiac EGM and several surface ECG leads, all which are recorded simultaneously [15], [23].

2.4.1 Approaches for Cardiac Mapping and Electrogram Analysis

Cardiac mapping is the process of identifying the temporal and spatial distribution of electrical potentials at multiple sites during a particular heart rhythm, and it includes several mapping modes such as body surface, endocardial, and epicardial mapping. It aims to understand the underlying mechanism(s) of arrhythmias and the propagation patterns of activation within a region of interest (ROI), and to identify the site of origin or a critical site of conduction as a target for CA [15], [23].

Conventional mapping relies on electrical information from a relatively small number of electrodes of a catheter and requires the need for fluoroscopic control of its position [62]. Besides being time-consuming and the associated risks with the use of X-rays, fluoroscopy does not provide precise three-dimensional (3D) information on the orientation and position of the catheter tip in a heart chamber [63].

A detailed mapping of electrical events is key for a successful intervention. As such, and to overcome the limitations of conventional mapping, recent technological advances have led to the development of non-fluoroscopic computerized mapping systems, also known as electroanatomical mapping (EAM) systems, with improved spatiotemporal resolution, 3D spatial localization, and high-speed map point acquisition. This revolutionary technology has provided new insights of the

mechanisms of arrhythmias and nowadays, mapping and ablation are typically performed in a single procedure [62].

Through the sequential acquisition of new anatomical points recorded at various key locations within the cardiac chambers combined with recorded data of the catheter location and local EGM, a representation of the 3D geometry of the chamber is reconstructed in real time, color-coded with relevant electrophysiological information [23].

AF drivers and substrates have been shown to present specific rate and regularity properties, so an accurate quantification of these features may be helpful for their detection [12]. Hence, a variety of approaches have been employed to extract EGM features relevant to clinical AF ablation. Some of the quantitative methods aim at localizing and targeting AF sources based on the analysis of the fibrillatory patterns/rate, either in the time domain (assessing the local activation time) [33], [64]–[66], or in the frequency domain (analysing the fibrillation dominant frequency (DF)) [67]–[69]. Other methods aim at analysing EGM complexity, including the Shannon entropy [70]. Methods to identify and quantify areas with CFAEs in order to assist its identification during ablation procedures have also been proposed [71], [72]. Focal impulse and rotor modulation (FIRM) mapping has also been proposed as a mapping alternative to identify spiral waves and rotors during AF [73], [74]. Further quantitative methods measure the organization and regularity of AF to search for areas responsible of AF maintenance [75]–[77].

The methods that will be discussed here are the CFAE and voltage mappings (time domain), the DF analysis (frequency domain), and the Shannon entropy analysis (nonlinear domain).

2.4.1.1 Time Domain Analysis: CFAE and Voltage Mapping

Since CFAEs are surprisingly stationary, exhibiting, relative spatial and temporal stability, it is possible to perform point-to-point mapping of these areas and associate them into an electroanatomical map [60].

Sites of EGMs whose cycle length (CL) is shorter than a cut-off value or display complex morphology are subject to ablation, as they are considered to be CFAEs. Several attempts to make this approach more precise have been made by developing algorithms for automatic CFAE detection without operator input [58]. These include the CFAE software module CARTOFINDER implemented by the CARTO® 3D EAM and the CFE-mean tool from the EnSiteTM NavXTM EAM systems [78]. Figure 2.16 illustrates the two algorithms for CFAE mapping embedded in the EnSiteTM NavXTM and CARTO® systems. These EAM systems will be discussed further.

The CARTOFINDER module allows the construction of an endocardial shell, enabling the tagging of CFAE areas in the anatomy of both atria, improving mapping accuracy. The algorithm to identify CFAE complexes quantifies this phenomenon in two parameters [59]:

1. Interval Confidence Level (ICL), where the number of intervals detected between consecutive complexes are identified as CFAE;
2. Shortest Complex Interval (SCL), where the shortest interval found in milliseconds, out of all intervals identified between consecutive CFAE complexes.

After the latter step, if a cycle length shorter than a specified threshold (120 ms) in a location is found, it is considered an ablation target [58].

In 2004, Nademanee et al. conducted a study to determine if CFAEs could be used as target sites for catheter ablation of AF. They reported a 95% rate success of AF termination and 76% of freedom at 1-year follow-up after a single procedure [79]. However, following studies led by Oral et al. and Verma et al. reproduced disappointing results, the former having only 33% of patients free of AF and 55% developing recurrence [80]; and the latter revealing no difference in recurrence rate when linear ablation or CFAE ablation was performed in addition to PVI, questioning this approach [81].

These results could be because all CFAEs may not be equivalent, as most of them do not actively participate in the AF process, representing poor targets for ablation [82], although fractionation may evolve over time as AF transitions from paroxysmal to persistent [38]. Another issue is that, despite the definition provided by Nademanee et al., more than 20 definitions and/or methodologies to identify CFAE have been introduced in literature since then. Hence, the lack of a universal definition and significant methodological differences have led to distinct study results when identifying and targeting "supposed" CFAE sites for ablation [83]. Nevertheless, as Sohal et al. concluded, "Mapping of all CFAEs is almost certainly obsolete, but there undoubtedly remain some CFAEs that are critical sites for AF maintenance and better identification of these may result in better outcomes in persistent AF ablation" [82].

There are also disadvantages on working in time domain as the assessment of local CLs in this domain is limited due to the irregular CL, varying amplitude, and signal morphology in AF. The signal often contains multiple sharp deflections that might be undersensed and not counted for calculation, including spatiotemporal dynamics that are difficult to characterize and interpret, and are susceptible to artifacts due to their low amplitude [73], [84]. Thus, time measurements can be difficult and inaccurate, especially when using automated algorithms to measure CL. An alternative method is frequency domain analysis.

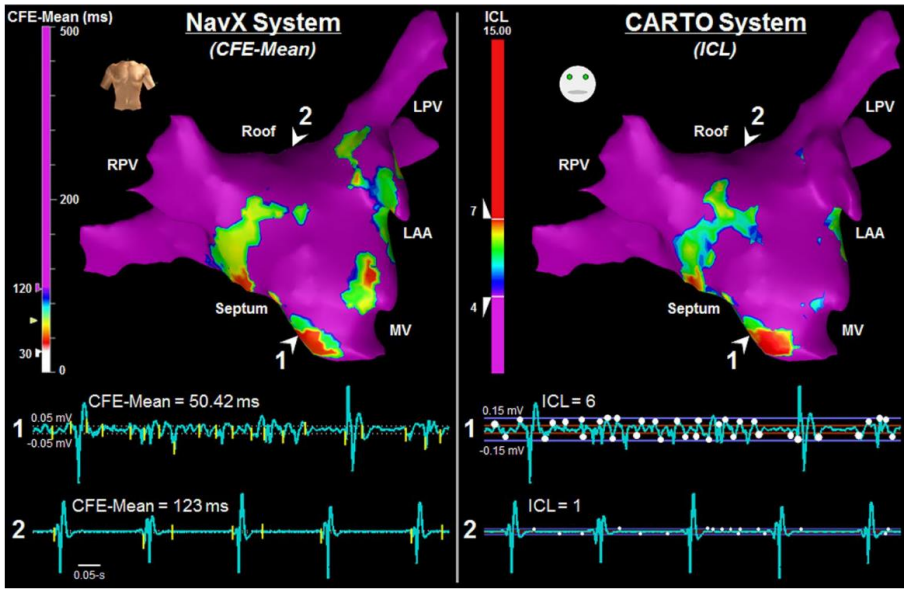

Figure 2.16: Algorithms embedded in the EAM systems for automated CFAE detection: NavX (left) and CARTO (right) 3D atrial geometry representation for the same patient. On the bottom part of the figure, the top traces refer to a segment of fractionated bipolar AEG (AEG 1), and bottom traces refer to a non-fractionated segment of bipolar AEG (AEG 2), both recorded from the LA endocardium. The AEG 1 has CFE-Mean = 50.42 ms and ICL = 6. The AEG 2 has CFE-Mean = 123 ms and ICL = 1. AEG: atrial electrogram, CFE-Mean index used by NavX to quantify AEG fractionation, FI: fractionated interval, ICL: interval confidence level: index used by CARTO to quantify AEG, LPV: left pulmonary veins, MV: mitral valve, RPV: right pulmonary veins. Adapted from [85].

The voltage map displays the maximal peak-to-peak amplitude of the EGM sampled at each anatomical site within a window of interest and provides a static representation of time-dependent electrical activation of the chamber [23], [86]. Voltage mapping is useful to help define anatomically correct regions of no voltage (typically presumed scars or electrical scars), low voltage, and normal voltage. Myocardial scars are seen as low voltage, and their delineation can help understand the location of the arrhythmia [23].

During signal acquisition, the EAMs systems typically transform in real time the raw voltage data recorded from the electrodes into a voltage map by two processes: firstly, projecting the recording coordinates onto the chamber shell, and secondly interpolating the voltage data across the surface of the anatomical model, usually in a color-coded fashion, with red as the lowest amplitude and orange, yellow, green, blue, and purple indicating progressively higher amplitudes [23], [86].

2.4.1.2 Frequency Domain Analysis: Dominant Frequency

Mathematically, it has been shown that any signal can be decomposed into a sum of weighted sinusoids of different frequencies. This mathematical operation is known as the Fourier transform, and it is the base of frequency domain analysis [87], [88]:

$$x(t) = \frac{a_0}{2} + \sum_{m=1}^{\infty} a_m \cos(2\pi m f_1 t) + \sum_{m=1}^{\infty} b_m \sin(2\pi m f_1 t) \tag{2.8}$$

A more complex signal would require more sinusoids to represent it, where each sinusoid would represent one frequency component each. When decomposing a signal into sinusoids, the one with the highest amplitude is defined as the dominant frequency (DF) of that signal [87], [89]. In a perfectly periodic signal, the frequency spectrum would present a sinusoid with the largest amplitude, corresponding to the DF (equal to the inverse of the signal's cycle length), and additional sinusoids with frequencies that are multiples or "harmonics" of the DF [24], [87]. The harmonic distribution quantifies the regularity or organization of the signal. Thence, two indices have been proposed: the Organization Index (OI) and the Regularity Index (RI).

The OI is the ratio between the area under DF ± 0.75 Hz and its harmonic frequencies between 3 to 20 Hz and the total area as shown in the following equation [90]:

$$OI = \frac{A(DF \pm 0.75) + \sum_{i=2}^{3} A[(DF * i) \pm 0.75]}{A(3\text{Hz to } 20\text{Hz})}, (DF \leq 10\ Hz) \tag{2.9}$$

where A is a function that calculates the area under the curve, and i is the ith-harmonic of the DF. When signals present a DF higher than 10 Hz, it is not possible to calculate the OI because the harmonics are greater than 20 Hz [90]. The OI denotes the percentage of periodic energy with respect to the total energy of the signal.

With regard to AF, the OI is theorized to represent the number of propagating AF wavelets. Thus, a spectrum with a dominant peak and discrete harmonics would likely represent a lower number of dominant wavelets circulating within the atria and would yield a high OI. With an increased number of wavelets, more frequency components are added to the atrial signal, resulting in a low OI [75].

The RI corresponds to the percentage of "sinusoidal" energy with respect to the total energy, and it is defined as the ratio of spectral power in a 0.75 Hz band centered at the DF and the total power between 3 and 20 Hz [90]:

$$RI = \frac{A(DF \pm 0.375)}{A(3\text{Hz to } 20\text{Hz})} \tag{2.10}$$

Usually, calculating the DF involves a filtering step prior the Fourier transform to the EGMs, known as the Botteron and Smith approach, which will be explained in chapter 3.

It has been suggested that ablation at sites of high-frequency activity during AF, some call "AF nests" [67] or regions with highest DF value (DFmax) results in termination of paroxysmal AF, indicating a possible role in the maintenance of the disease [68], [91]. The DFmax information can be displayed in a colour-coded fashion overlaid on the 3D atrial shell as illustrated in figure 2.17. In a 2009 study, Atienza et al. performed a catheter ablation of all DFmax sites prior to PVI in patients with paroxysmal and persistent AF. The probability of AF freedom with ablation of DF sites was higher, and AF recurrence increased in patients with remaining DF sites after the procedure [92]. However, later in 2014, the same group tested the hypothesis that targeted ablation of high-DF sites referred to as high frequency source ablation would be as effective as empiric PVI procedures, in which no additional improvements were observed [93]. Additionally, although in animal studies there is a correlation between sites of DFmax with rotor-like activity, it remains unclear if all DFmax sites represent areas of rotor-like reentry or other types of localised reentry, especially in humans [38].

DF analysis can be used to estimate activation rate. However, there are various factors that can affect the results, so it is essential to take those in consideration when employing this technique. In 2007, J. Ng et al. explored the technical issues that may affect the estimation of local activation rate during AF using DF analysis, including the effects of unipolar versus bipolar recordings, bipolar electrode spacing, far-field ventricular depolarizations, signal duration on AF, among others. They found out that b-EGMs are preferable to use, but preprocessing is a necessary step; that ventricular far-field significantly affects DF analysis, thus ventricular template subtraction is helpful to remove that far-field; and a recording duration above 2 seconds is required for reliable DF measurements [94]. This method also requires added precision to the term "highest" DF to be usable [58]. Another concern is that by employing the Fourier transform, we are assuming that the system is linear, and the data is stationary, which is not the case when dealing with physiological signals such as EGM; and when we apply the Fourier transform, we lose the ability to track temporal variations.

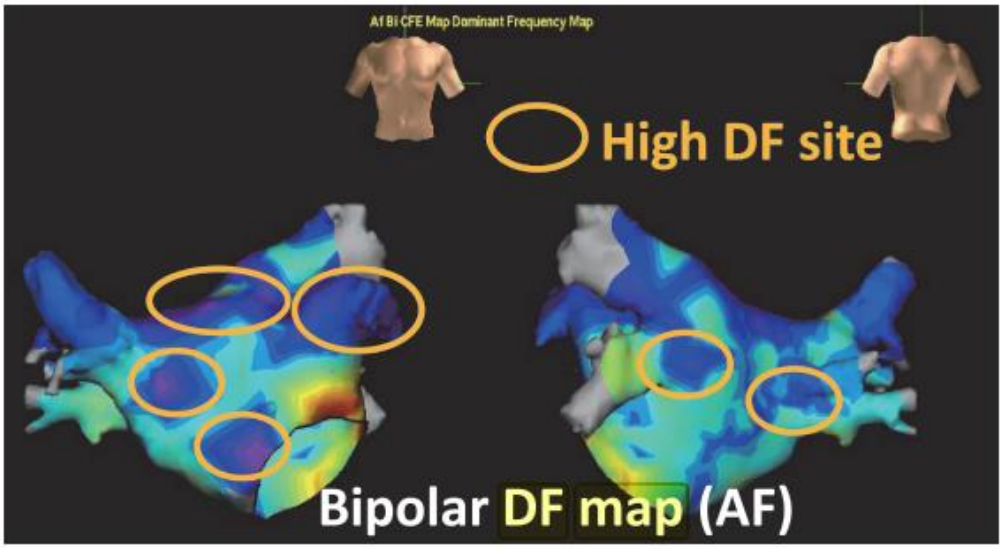

Figure 2.17: DF mapping derived from b-EGMs in a patient with AF. The 3D colour-coded DF map displays low frequencies in red and high frequencies in purple. Adapted from [95].

2.4.1.3 Nonlinear Analysis: Shannon Entropy

The (concept of) information entropy, referred to as Shannon entropy (ShEn), of a random variable is characterized by the (average) level of "information", "surprise", or "uncertainty" inherent in the variable's possible outcomes, and it is defined as [96]:

$$SE = -\sum_{i=1}^{M} p_i \log_2 p_i \tag{2.11}$$

where M is the number of discrete values the variable can assume and p_i is the probability of assuming the ith value [13]. The choice of a logarithmic base corresponds to the choice of a unit for measuring information [96]. A lower entropy indicates higher knowledge and thus, more certainty of the outcome. A common step taken to calculate the ShEn is to bin each sample according to its amplitude into a voltage histogram to obtain the probabilities [70], [97]. In this case, p_i corresponds to the relative probability density, which is the number of counts in the ith-amplitude-bin divided by the sum of bin counts in all bins [97], [98]. Figure 2.18(a) demonstrates an example of a rotating wave and how ShEn is able to differentiate the pivot from surrounding peripheral regions. EGM signals with few states, i.e., stable morphology, have a narrow distribution in the voltage histogram and low ShEn. In contrast, EGMs with a complex morphology, such as AF signals, contain a number of different types of deflections and, therefore, have a broader amplitude distribution in the voltage histogram, and a higher ShEn [97]. Afterwards, similarly done with the DF information, the ShEn values can be displayed in a colour-coded fashion overlaid on the 3D atrial shell (see figure 2.18(b)).

The ShEn has been used to quantify the complexity of the CFAE and distinguish between CFAE and non-CFAE signals determined by Nademanee's criteria, using a fully automated algorithm. ShEn had a discriminant ability higher than 85%. A limitation of this metric is that noise and EGM complexity are both characterized by high entropy values [70]. Additionally, it was shown that the pivot zone of rotors was consistently associated with high ShEn values of b-EGMs, allowing to distinguish from surrounding peripheral regions. Therefore, it can be a potential tool to assist AF rotor mapping [97], [98]. Furthermore, studies examining ablation outcome based on this technique are ongoing. Hwang et al. evaluated the nature of rotors in 2D and 3D in- silico models of persistent AF by analysing PS, DF, ShEn and CFAE cycle length and their ablation-based approaches. They found that rotor locations were well represented by DF and their ablation terminated AF. The same results were not observed for the other approaches [99].

The ShEn has the disadvantage of being a "static" measure, in the sense that it does not consider the changing activity of a system over time; it only measures information content quantified in the present value of the time series [100], [101].

In general, there has not been many studies employing this metric when it comes to AF as it remains underutilized and underexplored in this field, so more research is needed to explore the potentials of this technique and its usefulness in the study of AF.

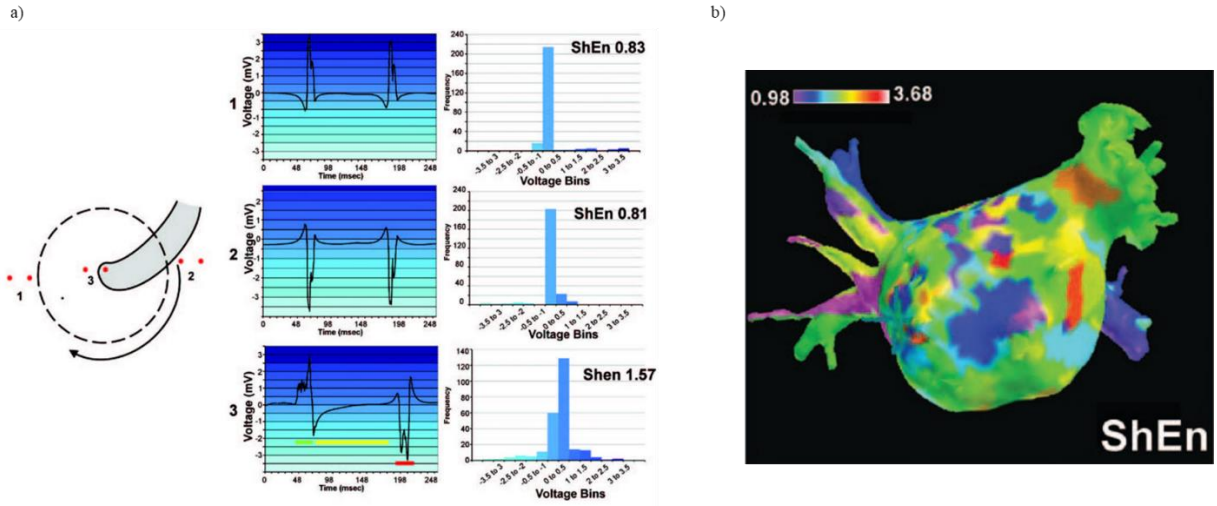

Figure 2.18: Employment of ShEn to bipolar EGMs to differentiate the pivot and periphery at sites of rotational activation: a) relationship between ShEn and the amplitude distribution (given by the histogram) in a rotating wave. The histogram was generated by binning each sample of the bipolar EGM into voltage bins with a bin size of 0.5 mV. Bipoles located in positions 1 and 2 (at the periphery of the rotating wave) experience consistent activation direction, resulting in a more stable EGM morphology and narrow voltage amplitude histogram. On the contrary, bipole at position 3 (near the pivot) experiences sharp local deflection (green), but secondary activity as the wavefront changes direction, including intermediate activity (yellow) and inverted potential (red). As a consequence, the signal values are binned in a broader range of voltage bins, leading to a higher ShEn. The largest bin in the histogram is near zero, reflecting the high proportion of signal values from near the isoelectric line; and b) an example of a left atrial ShEn map (AP view) from a patient with AF that may facilitate accurate pivot localization. Adapted from [97].

2.4.2 Non-fluoroscopic System: CARTO

There are some differences among the EAM systems in terms of how they operate; however, they share some common features [62], [102]:

- Non-fluoroscopic 3D localization of multiple catheters within the heart, reducing fluoroscopic exposure.
- Display EGM signals characteristics, most commonly activation time and voltage, in the 3D anatomical structure, using a color-coded scale.
- Integration of electroanatomic information with 3D images of the heart obtained from point-by-point sampling, intracardiac ultrasound, computed tomography (CT), or magnetic resonance imaging (MRI).

In particular, the CARTO® EAM system, developed by *Biosense Webster Inc*. (Irvine, California, USA), uses ultra-low electromagnetic fields generated by three magnetic coils located in the locator pad, positioned under the examination table where the patient lies during the procedure (see figure 2.19(a)); and six electrode patches, positioned on the patient's back and chest (see figure 2.19(b)) [23], [99], [103]; this creates a non-homogeneous electromagnetic field around the patient's chest. These fields are detected by the sensors located in the distal tip of the mapping-ablation catheter, determining accurately its position and orientation (via a triangulation calculation) in relation to the fixed magnetic field sensors; and thus, aiding its placement into a heart chamber to be mapped under fluoroscopic guidance, while simultaneously recording local bipolar and unipolar EGMs from the catheter tip [15], [23]. Additionally, a data-processing and graphic display units are coupled to the system, and so, by sequentially recording electrical and spatial information from different sites, a 3D geometry of the mapped chamber is reconstructed in real time [23].

During the mapping process, the CARTO system can deal with four types of motion artifacts: cardiac, respiratory, patient, and system motions. Therefore, to compensate for these possible artifacts,

several steps are taken including defining an electrical reference (reference EGM), an anatomical reference, and a window of interest (WOI) [23].

The electrical reference corresponds to a fiducial marker on which the entire mapping procedure will be based on, since all local-activation-timing information recorded by the mapping catheter at different anatomical sites will be relative to this marker. It is defined by the user assigning a reference channel and an annotation criterion. Any ECG lead or intracardiac EGM in bipolar or unipolar mode may serve as an electrical reference. The timing of the fiducial marker is used to determine the activation timing in the mapping catheter relative to the acquired points and ensures that the data is collected during the same part of the cardiac cycle. The LAT is calculated as the time interval between the fiducial marker on the reference EGM and the corresponding local activation determined from the unipolar or bipolar local EGM recorded from each anatomical site [23].

When the mapping catheter is placed inside the heart, it can suffer all sorts of motion artifacts. To overcome these, a reference catheter with a location sensor serves as an anatomical reference and it can be placed inside the heart or on the patient's back, in the interscapular area. When the latter, the location sensor is placed in an adhesive reference patch secured on the patient's back. The CARTO system continuously calculates the position of the mapping catheter in relation to the anatomical reference, therefore solving the problem of any possible motion artifacts [23].

The final crucial step is to define an electrical WOI to ensure the accuracy of the initial map coordinates. The WOI is defined by two intervals, one extending before the fiducial marker and other after it, during which the LAT is determined; and the boundaries are set relative to the electrical reference. Thus, within this window, activation at each anatomical site is considered early or late relative to the reference [23].

The system presents a few limitations: because the process of creating an electroanatomical map uses a sequential, point-by-point mapping technique, it requires tagging many points, making the data acquisition very time-consuming. Furthermore, if the position of the patient or the reference catheter changes considerably, a new map has to be created. Another limitation of the CARTO system is the requirement of special *Biosense Webster* catheters. No other catheter types may be used with this system [23].

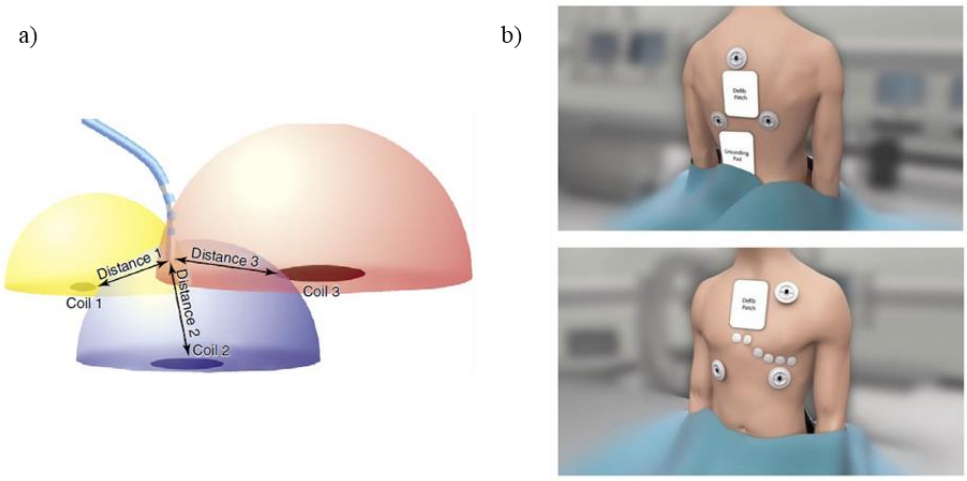

Figure 2.19: CARTO electroanatomical map setup: a) schematic diagram of CARTO coils localizing the CARTO catheter (adapted from [23]), and b) patch placement on the patient's chest and back (adapted from [103]).

2.4.3 Electrode Catheters: The Pentaray Catheter

Invasive catheters are used during an EP testing to record the cardiac electric activity and perform electrical stimulation (pacing). These catheters consist of insulated wires, with one or more electrodes attached to the wires exposed to the cardiac tissue. They come in different materials depending on the desired properties (stiffness, curvature, etc.) and different electrode configuration and sizes [23].

Multielectrode catheters have different shapes and electrode configurations (this includes inter-electrode distance and number of electrodes), allowing special properties for cardiac mapping. Specifically, the Pentaray® (Biosense Webster, Inc., Baldwin Park, California, USA) catheter, illustrated in figure 2.20(a), is a 7 Fr steerable catheter (180 degrees of unidirectional flexion) and has 20 electrodes distributed over five soft radiating spines (1-mm electrodes separated by 4-4-4 or 2-6-2 mm interelectrode spacing), allowing splaying of the catheter to cover a surface diameter of 3.5 cm (see figure 2.20(b)) [23].

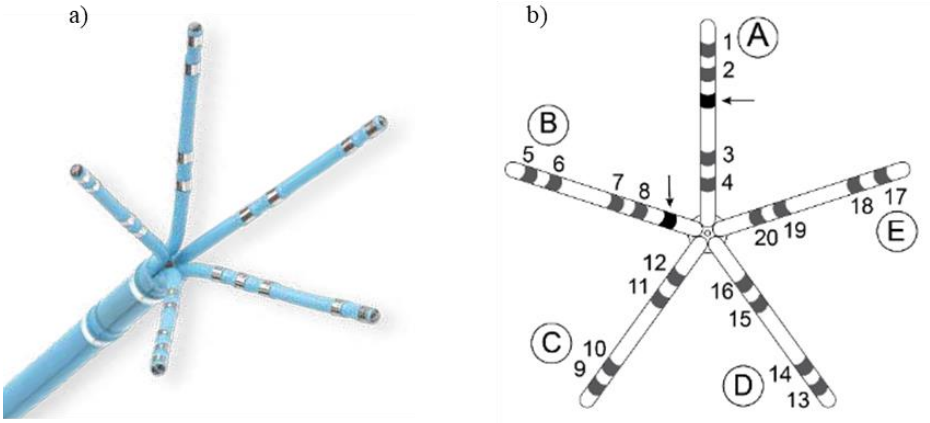

Figure 2.20: Multielectrode mapping catheter: a) Pentaray® catheter (Biosense-Webster, Inc., *Diamond Bar, CA, USA*), and b) identification of the spines of the Pentaray catheter. Adapted from [104].

2.4.4 High-Density Mapping

The concept of high-density (HD) mapping stands for the simultaneous acquisition and annotation of multiple EGMs, which are then analysed by automated algorithms to generate precise activation and voltage maps simultaneously [60].

Prior generations of EAM systems were technically capable to perform HD mapping with multielectrode catheters. However, it was a long task that required manual annotation following electrogram data collection and was prone to errors either by the operator or the system regarding appropriate acceptance/rejection of mapping data. Improvements of the HD mapping systems strived to mitigate these issues through novel mapping methodology, hardware innovations, and automated software algorithms that allow extremely fast and accurate acquisition of an almost unlimited number of 3D points, together with the respective local electrogram [105].

The feasibility of this technology was greatly supported by the development of multipolar catheters of high resolution, such as the Pentaray® catheter, the AdvisorTM HDGrid catheter, the ConstellationTM "basket" catheter, and many others appearing on the market nowadays. These catheters present multiple electrodes for fast data acquisition, and a small electrode size, with low impedance, and shorter inter-electrode distance to maximize the signal-to-noise ratio [60], [106].

The information acquired with this technology is very rich and we can observe signals that cannot be identified with conventional catheters. However, a pitfall of collecting an overabundance of points

can potentially be translated into incorrect annotation and interpolation in the surrounding regions. Hence, the operator still must manually check the EGM data, particularly if the map does not fit with what is physiologically known or the expected arrhythmia mechanism [106].

2.5 Catheter Ablation

Catheter ablation of AF is a well-established and widely performed therapy intervention for symptomatic patients when antiarrhythmic medication fails and to prevent AF recurrence [107], [108]. When ablation energy is delivered, the target is heated to temperatures above 50°C with a specialized catheter, creating permanent lesions in the arrhythmogenic tissue. This procedure is preceded by an electrophysiological study and having identified the arrhythmia mechanism and ablation target(s) [23], [102].

There are three main approaches for CA of AF [6], [8]: the PVI, which is based on electrically isolating the PVs from the rest of the LA and perform linear lesions around the tissue outside the ostium of the PVs, termed the antrum [109]; the left atrial linear ablation, consisting of additional linear lesions at the left atrial roof and mitral isthmus, a part of the postero-inferior area of the lateral left atrial wall located between the mitral annulus and the left inferior PV ostium [110]; and the ablation of left atrial electrophysiological targets, such as CFAEs, non-pulmonary foci, rotors, GP, fibrosis-guided voltage, and high DF sites. Because extensive ablation is advocated for patients with persistent AF, the latter two approaches may be performed along with the PVI. However, the STAR AF II demonstrated that additional ablation did not result in better outcome compared with PVI alone in patients with persistent AF [81], and these results have been corroborated by following publications [111], [112].

2.5.1 Radiofrequency Ablation

Radiofrequency (RF) energy is the most common energy source used for ablation. It has become a widely accepted treatment for most atrial and ventricular arrhythmias, as it was demonstrated to be effective in producing precise and effective lesions [23], [102]. Figure 2.21 illustrates a RF ablation of the PV. The delivery of RF energy is generally performed in a unipolar fashion and electrically conducted through the catheter tip, where the body becomes part of the in-series circuit, with an alternating current flowing from the RF generator connected to the catheter tip to a ground pad (or dispersive electrode) located in the patient's skin [23], thus passing the energy through the intervening tissue, heating it with the high current density around the catheter tip. Any leftover energy transferred to the ground pad is dissipated as heat [23], [113]. With standard RF, power delivery of 30-50 W is titrated to an electrode temperature between 55-70°C and an impedance fall of 10-15 ohms [23], [102], and the most common frequencies of the RF current range from 300 to 1000 kHz for safety and efficacy reasons [23].

The thermal injury produced by RF ablation is due to two phenomena: resistive heating and conductive heating [102]. Resistive heating refers to the ablation lesion created by direct contact of the electrode with the tissue, within the first 2 mm of depth from the electrode surface. Conductive heating corresponds to the conduction of the thermal heating from the rim to the tissue surroundings resulted from the direct contact, which spans to a distance depending on the applied power and continues after RF application ceases [23].

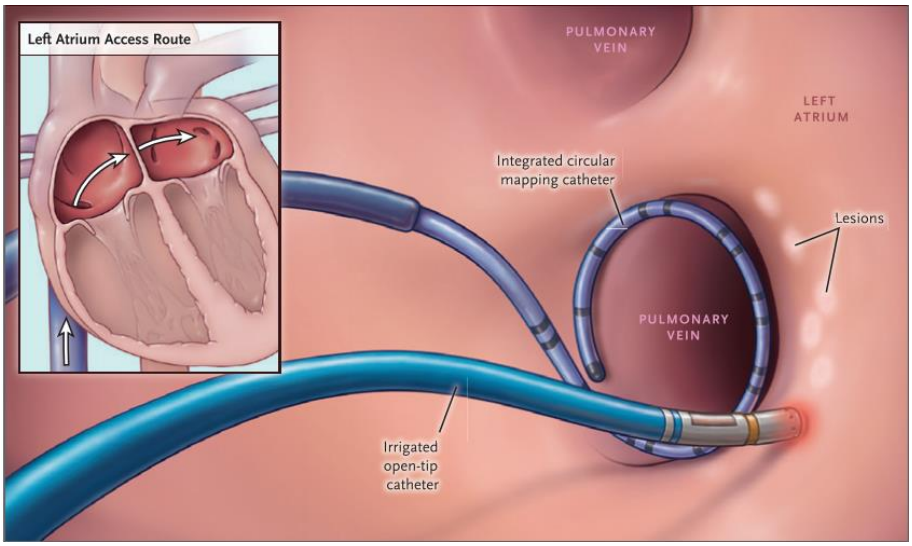

Figure 2.21: Radiofrequency ablation of PV: heat-energy is transferred to the tissue and delivered a series of point-by-point connected lesions with assistance from a 3D navigational system. Adapted from [114].

The effectiveness of RF ablation is dependent on RF power and application duration, but the most important factors are the electrode-tissue contact and cooling effect from the circulating blood pool [23], [102], [115], [116]. In normal conditions of electrode-tissue contact, only a fraction of the RF power is effectively applied to the tissue, while the remainder is dissipated in the blood pool and the rest of the patient. This causes the temperature of the catheter tip to be lower than the temperature of the tissue and thus, limits the size of the lesion formation [23], [116]. Consequently, optimizing RF ablation involves creating an adequate-sized lesion while minimizing the chance of an impedance increase, as this leads to the formation of coagula at the electrode or formation of steam within the tissue [23]. As the optimal method of energy application has not yet been defined, a variety of different approaches to energy titration can be successful. Nevertheless, energy applications should be titrated to that required to eliminate the arrhythmia while avoiding excessive tissue damage [102].

Conventionally, ablation catheters have 4-mm long tip electrodes, but there are also available bigger tip sizes, typically from 8 to 10 mm [23]. Although a larger electrode size increases the lesion RF because it allows greater energy delivery, it also causes more energy to be dissipated to the blood pool, and therefore a lower size lesion. To compensate this, greater RF power is required when compared to smaller tip size electrodes as shown in figure 2.22 [23], [117].

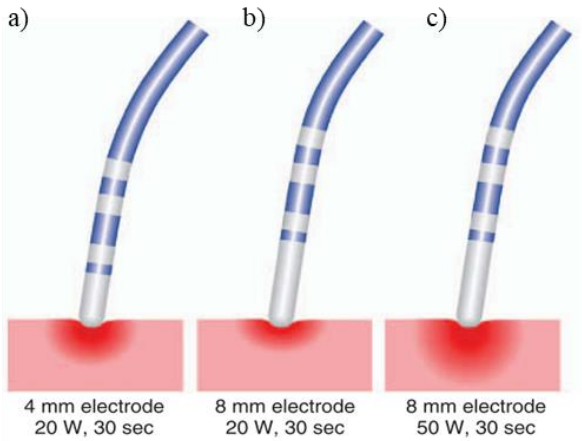

Figure 2.22: Illustration of lesion formation (extension and depth) of different catheter tip sizes: a) lesion created by a 4 mm catheter tip, b) lesion created by a 8 mm electrode catheter tip with 20 W power output, and c) lesion created by a 8 mm catheter tip with 50 W power output. Adapted from [23].

2.5.2 Other Energy Sources

RF ablation is not free from limitations, particularly on how RF produces a relatively small depth and size tissue injury. As such, modifications to the RF energy delivery mechanism, including cooled catheters and pulsed energy, and alternative energy sources have been explored to address some of these limitations [23]. Cryoablation has emerged as the main alternative to RF ablation in clinical practice. The FREEZE Cohort study and the FIRE AND ICE trial have demonstrated the method to be as safe and achieve similar success rates as with RF ablation in patients with paroxysmal AF [114], [118]. However, more data is necessary to determine the preferred energy source for first-line CA of AF [118].

Other alternative sources comprise microwave, ultrasound, and laser, but they are not clinically available for CA [23], [102].

2.6 Objectives

The field of AF has been growing over the last years. While there has been a great development in analysis techniques and methods, hardware, and automated software algorithms to get a deeper understanding of the mechanisms underlying AF and choose an optimal treatment approach, there appears to be no consensus among researchers in identifying the areas responsible for triggering and maintaining advanced stages of AF, thus forming the basis for very different approaches in the development of methods and algorithms.

This problem is compounded by the lack of a basic, 'gold standard' methodology, leading to different catheters used to record the EGM signals; different experimental setups allowing for different results and conclusions; different proprietary software systems with different analysis methods and mapping techniques; and a lack of identification of additional ablation targets, especially in patients with persistent AF, resulting in non-effective treatment. Ultimately, this raises the following inquiry: “Do different methods indicate different phenomena/mechanisms, or we are observing the same phenomena with different ‘lenses’?”. Hence, the main objective of this project is to perform a comparative exploration of alternative methods to analyse EGM signals and evaluate if in fact different methods “observe” the same phenomena or not, and their utility in detecting with precision the activation centers responsible for triggering and sustaining AF. By knowing with accuracy these sites, the ablation procedure’s efficiency and safety could be improved greatly.

3 Methodology

The purpose of this chapter is to explain the mapping procedure performed in the Santa Marta hospital to obtain the electroanatomical HD maps, and to give a description of the clinical mapping data used in this work, as well as the clinical characteristics of the patient sample. The software used and the routine employed to process the EGM signals and obtain the 3D maps of the LA are also outlined here.

Ten patients with AF were included in the study. Table 3.1 summarizes the baseline clinical characteristics of the patient sample. From these patients, 10 electroanatomical maps from the LA were studied.

Table 3.1: Baseline clinical characteristics of the studied patient sample. Values are given in mean ± standard deviation or number and (%), when appropriate.

	Entire population (n = 10)
Age (years)	67.6 ± 7.4
Male sex, (n)	8 (80)
Paroxysmal AF, (n)	6 (60)
Hypertension, (n)	7 (70)
Mapping points	2810 ± 1552

3.1 Mapping Procedure

Each patient underwent a routine preprocedural transthoracic echocardiogram to evaluate left ventricular ejection fraction (LVEF), and left atrial dimensions, screen for structural heart disease, and CT or MRI (with the segmentation of the LA) to assess left atrial anatomy and to exclude the presence of intracardiac thrombi. Additionally, if the mentioned imaging study was performed 48 hours before ablation, transesophageal echocardiography was done on the day of the procedure (to exclude thrombi).

All patients were admitted for ablation procedure at Santa Marta hospital after continued oral anticoagulation (for at least four weeks before ablation) using warfarin with a therapeutic international normalized ratio (INR) (2.0 to 3.0) or direct oral anticoagulants (DOAC), with one dosage omitted in the evening before the ablation. Continuous monitoring of oxygen saturation and ECG were maintained throughout the ablation. All procedures were carried out under conscious sedation or general anaesthesia. In brief, the protocol steps for radiofrequency catheter ablation (RFCA) consisted of: 1) positioning a decapolar catheter through the right femoral vein to guide the transseptal puncture and to pace the LA; 2) a single transseptal puncture to access the LA by fluoroscopic guidance using a needle system (St. Jude Medical Inc., St. Paul, Minnesota, USA) and an AGILIS NxT steerable introducer (St. Jude Medical Inc., St. Paul, Minnesota, USA), continuously irrigated with heparinized saline during the whole procedure; 3) heparin administered intravenously as a bolus (100 U/kg of standard heparin), followed by an additional bolus to maintain an activated clotting time between 300-350 seconds; and 4) 3D mapping of the LA performed with the CARTO system, using a HD mapping catheter.

Regarding the fourth step, the 3D electroanatomical maps of the LA were acquired using the CARTO 3 V7 EAM system while patients were in AF. For each patient, different number of mapping points were acquired, and each mapping point includes 12-lead ECG signals, unipolar and bipolar EGM signals from a 20-pole 1mm Pentaray® catheter. Since the b-EGM signals are less susceptible to noise and far-field potentials, they are often more used in clinical practice comparing to u-EGM signals [32], [33]. For this reason, only the bipolar signals were used in this study. The recording time defined by the CARTO system to acquire each EGM from each anatomical mapping point is 2.5 seconds, as it assumes that at a higher recording time, the catheter would no longer be stable. The

signals were acquired point-by-point with a sampling frequency of 1 kHz and bandpass filtered between 16 and 500 Hz with a 50 Hz powerline suppression notch filter.

After geometry and voltage map were completed, the mapping catheter was removed, and the ablation catheter was introduced by the same sheath. Radiofrequency applications were performed using an open-irrigated-tip catheter (ThermoCool SmartTouch® SurroundFlow, Biosense Webster, Inc.) with point-by-point-lesions. The maximum delivered RF energy did not exceed 35 watts. Remapping was performed to analyse signals, possible gaps, and low voltage areas (LVA). If so, ablation of gaps, followed by remapping to confirm homogeneous low voltage and PVI, was done.

An open-source tool for electrophysiology data analysis named OpenEP, which is available at [119], was used to import the data to MATLAB to process the signals and create the 3D anatomical AF maps of the LA. The data was imported to MATLAB and stored in a variable, named 'userdata', with a `struct` format with various fields. The most relevant fields for this work were the 'electric' and 'surface', which are also a `struct` containing various fields.

Regarding the 'electric' `struct`, the most important fields were the 'egm', 'egmX', 'voltages', and the 'egmSurfX'. They store, respectively, the recorded bipolar EGMs, the Cartesian coordinates of the mapping points, the bipolar voltage (and the unipolar voltage) measured by the CARTO system for each mapping point, and the Cartesian coordinates of each mapping point, projected to the closest point on the surface of the chamber. Concerning the 'surface' `struct`, the most important field was the 'triRep'. 'triRep' provides the 3D triangulation representation of the surface mesh of the LA in the form of variables 'X' and 'Triangulation', which correspond to the Cartesian coordinates of the vertices and the vertex indices of each face in the surface mesh, respectively [119].

3.2 Signal Preprocessing

The bipolar signals were preprocessed using MATLAB R2018a (version: 9.4.0.813654) and the functions from the Signal Processing ToolboxTM integrated in the software.

The first step was to sort the anatomical points collected during the mapping procedure and include those that contained just the recorded atrial activations, which are translated as sharp, large atrial EGMs (figure 3.1(a)), and exclude the remainder, by labelling as NaN and their corresponding Cartesian coordinates stored in 'egmX' and 'egmSurfX'. The remainder included points whose signal contained: 1) a lot of electrical noise, being difficult to identify the atrial activations (figure 3.1(b)); 2) ventricular signal (QRS complex) (figure 3.1(c)); 3) low amplitude activations (< 0.2 mV), characteristic of scar tissue (hampering the detection of atrial activations), or corresponded to ventricular far-field potentials due to ventricular depolarization (figure 3.1(d)); 4) isoelectric line the whole duration, particularly common around the PVs since they were electrically isolated during the mapping process (figure 3.1(e)); and 5) only one or two activations, probably due to bad contact between the electrode and the tissue (figure 3.1(f)). The open-source tool named EPLAB WORKS, available at [120], facilitated this task because it allows to visualize the mapping points in the 3D mesh of the LA and their corresponding b-EGMs simultaneously, a limitation found using both MATLAB and the OpenEP tool. Figure 3.2 illustrates the EPLAB WORKS's interface.

The second and third steps were to calculate the DF and the ShEn, and then plot their respective 3D maps, along with the voltage map, respectively. These steps are explained below.

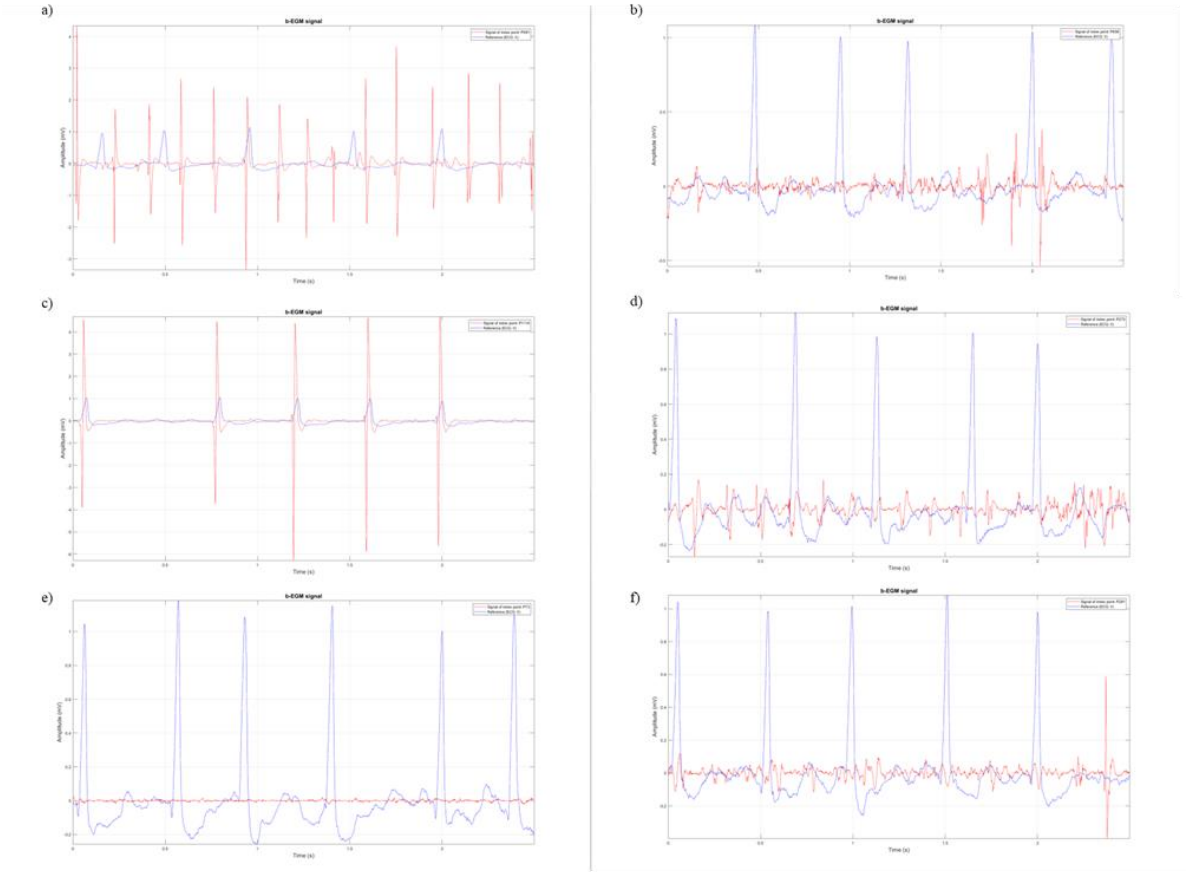

Figure 3.1: Bipolar signals from different mapping points from the same patient in AF: a) atrial activations represented by sharp, large atrial EGMs, b) signal with electrical noise, being very difficult to distinguish the atrial activations, c) ventricular far-field (QRS complex), d) low amplitude P-waves (≤ 0.2 mV), characteristic of scar tissue or corresponded to ventricular far-fields, e) signal with no activations, and f) signal with only one activation. The blue line corresponds to the signal reference, which in this case is the lead II of the ECG, and the red line is the b-EGM signal. The purpose of plotting the electrical reference is to see if the sharp activations in the bipolar EGM correspond to atrial activations or to ventricular far-field.

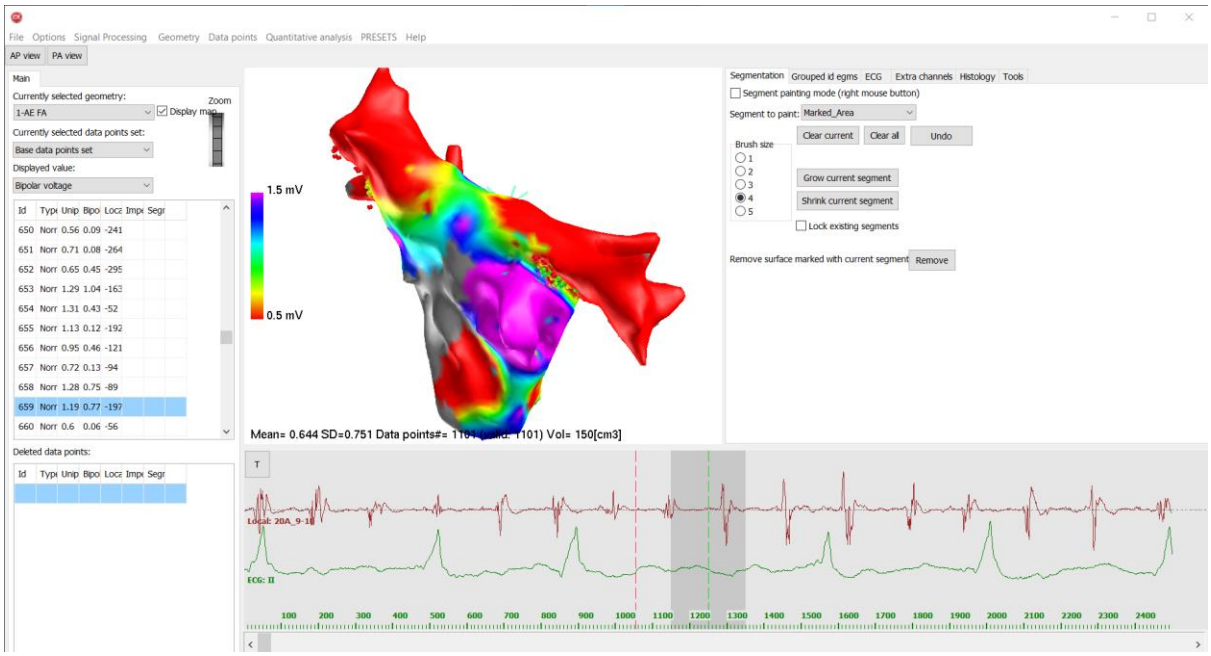

Figure 3.2: Interface of EPLAB WORKS.

3.3 Signal Processing

The processing task and the calculation of the metrics mentioned previously were performed by also using MATLAB R2018a (version: 9.4.0.813654), and the functions from the Signal Processing ToolboxTM integrated in the software and the functions from the OpenEP tool. It was not necessary to calculate the voltage of the bipolar signals, because the data exported from the CARTO system contained that information. As such, when importing the data to MATLAB, the voltage data was already stored in the 'userdata' structure.

3.3.1 Dominant Frequency

For the analysis in the frequency domain and to calculate the DF, the b-EGM signals were first processed following the Botteron and Smith approach [121]. Its aim is to enhance the atrial activations of EGM signals, simplifying the shape variations whilst reducing noise. This is achieved by transforming the signal into a train of activation pulses, with the fundamental frequency corresponding to the atrial rate [69], [122]. This approach consists of three steps that are illustrated in figure 3.3:

1. Bandpass filtering with 40 and 250 Hz cut-off frequencies, using a Butterworth infinite impulse response (IIR) filter.
2. Signal rectification.
3. Lowpass filtering with 20 Hz cut-off frequency, using a Butterworth IIR filter.

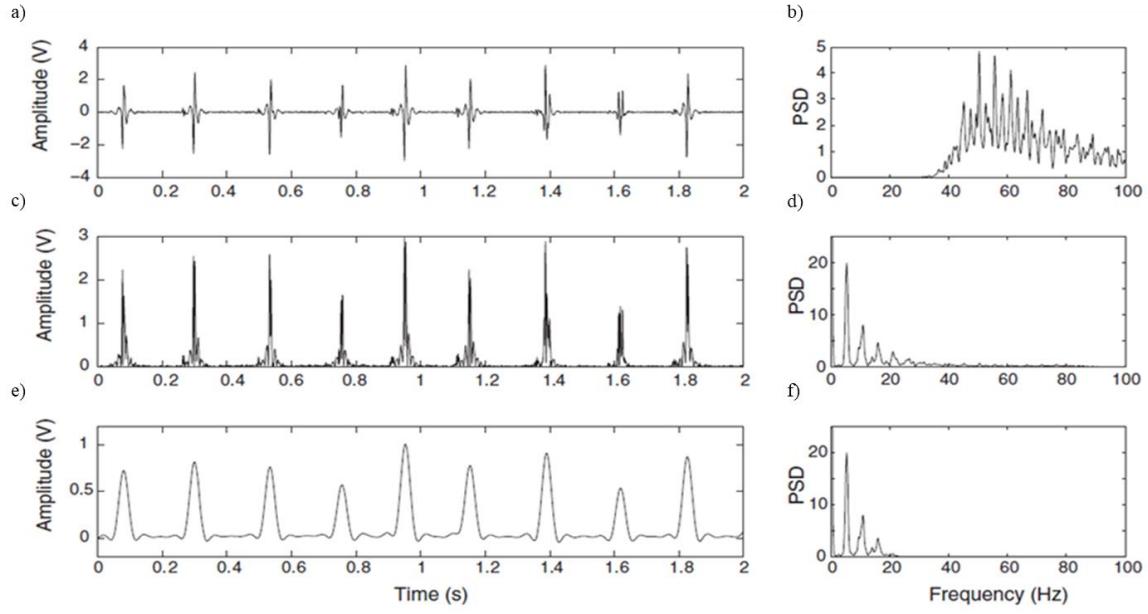

Figure 3.3: Effects of each preprocessing step on AF signal and its spectrum: a) and b) after bandpass filtering, c) and d) after rectification, and e) and f) after lowpass filtering. Adapted from [122].

Following the Botteron and Smith approach, the first step was executed using the MATLAB `butter` function to create an eighth order Butterworth bandpass filter, and the `filtfilt` function to perform a zero-phase digital filtering. The purpose of this filter is to avoid out-of-band noise. The second step was executed using the MATLAB function `abs`. Lastly, an eighth order Butterworth lowpass filter was applied using the same MATLAB functions as in step 1. The purpose of steps 2 and 3 is to enhance the fundamental frequency, which corresponds to the DF as it is related to the frequency of activation of the cardiac cells. In particular, step 3 ensures that the fundamental frequency, i.e., the real activation frequency, has more power than the harmonics so that when we calculate the DF, we are not calculating a harmonic of the DF, but instead the real activation frequency. An eighth order filter was chosen because an order below would not attenuate well enough the components outside the bandpass, and a higher order would result in undesirable instabilities.

Afterwards, a Hanning window, using the MATLAB function `hann`, was applied to the signals to reduce spectral leakage. The size of the window was equal to the length of the signals, because since the signals are only 2.5 seconds, a smaller window would worsen the resolution. Finally, the Fast Fourier Transform (FFT) was employed, giving the power spectrum of the signals. This was achieved with the MATLAB function `fft`, and zero-padding was applied through this function to improve the frequency resolution to 0.06 Hz. Applying a window and zero-padding are common steps adopted by various authors when analysing EGMs in the frequency domain [87], [89], [123], [124]. The DF was defined as the frequency with the highest amplitude within a range of 3 to 20 Hz. The DF was found by employing the MATLAB function `findpeaks` between the frequency interval mentioned previously. In AF, the most accepted values for DF range between 3 and 12 Hz [125]. Next, the OI was calculated using equation 2.9 for signals in which DF was equal or below 10 Hz. As for the b-EGMs that were labelled as NaN in the previous step, their corresponding DF and OI were also equal to NaN.

The DF and OI values were stored in created variables ‘dominantFrequency’ and ‘organizationIndex’, respectively. The variables were added in the ‘userdata’ structure to plot the DF maps. Figures 3.4 and 3.5 exemplify the Botteron and Smith approach and how the DF was found, respectively.

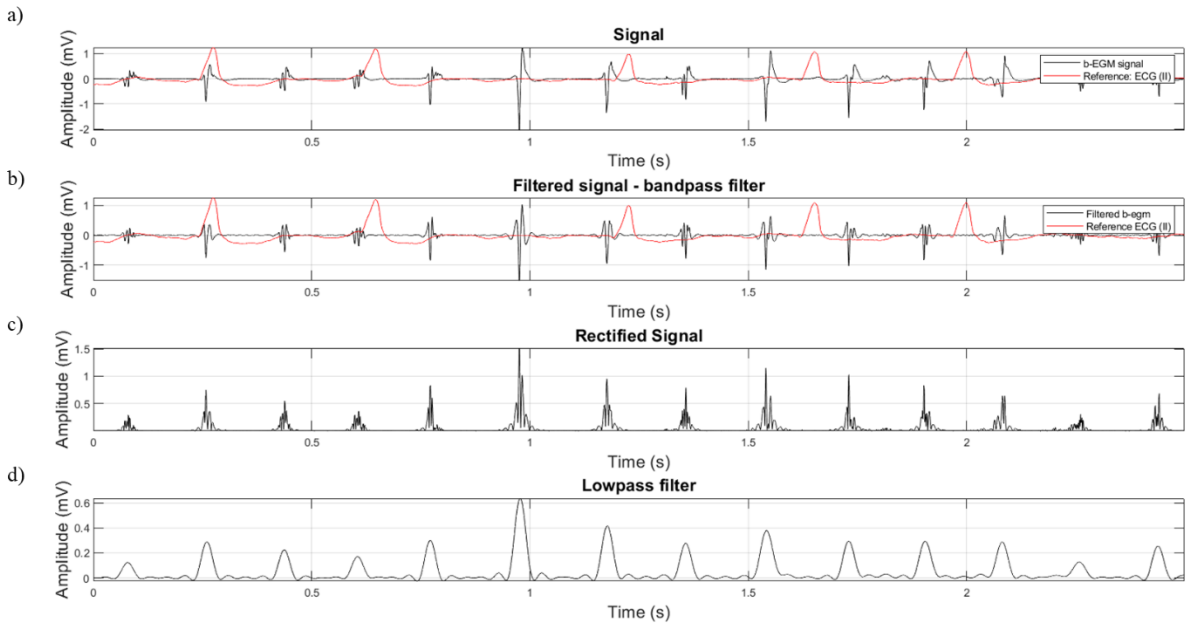

Figure 3.4: Botteron and Smith approach applied to an AF b-EGM: a) unfiltered b-EGM signal, b) after bandpass filtering, c) after rectification, and d) after lowpass filtering. The black line represents the b-EGM signal, and the red line represents the electrical reference, lead II of the ECG.

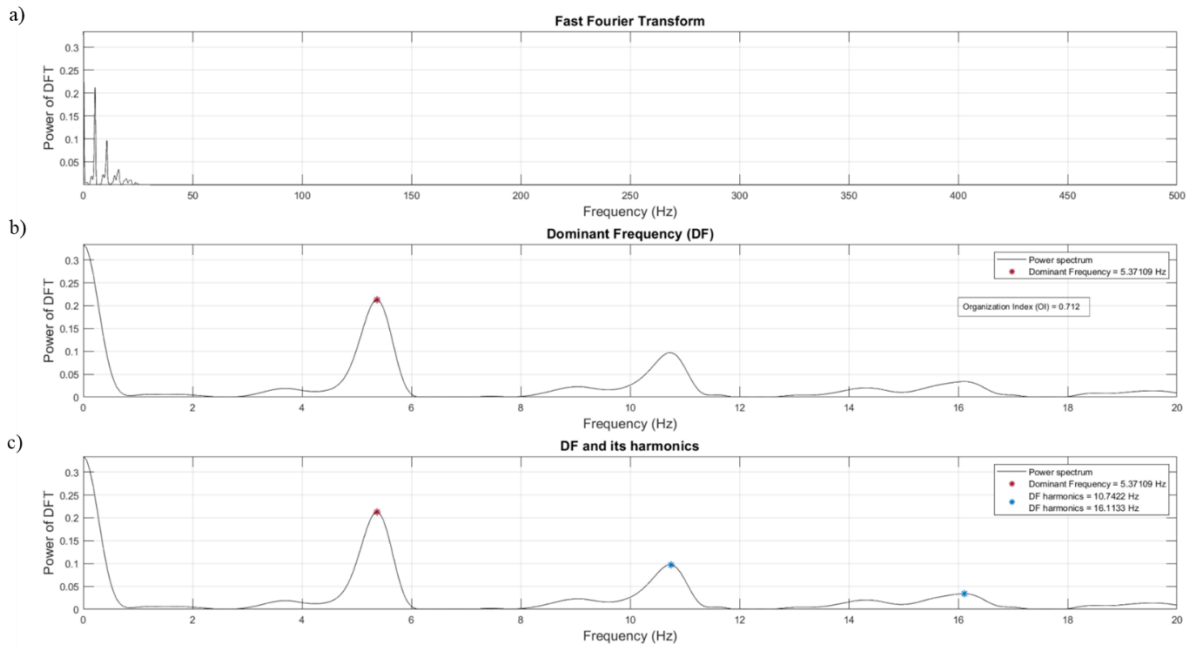

Figure 3.5: DF and its harmonics: a) power spectrum after employing the FFT, b) finding the DF and OI, and c) finding the DF harmonics.

3.3.2 Shannon Entropy

Firstly, the bipolar signals were filtered using the same Butterworth bandpass filter as before for the frequency domain. Since the calculation of the ShEn requires each EGM amplitude sample to be classified into bins according to its amplitude, the MATLAB function `histcounts` was employed, with a fixed bin size of 0.01 mV, to obtain the probabilities to calculate the ShEn by using equation 2.11. The probabilities are given by the number of counts in the ith-amplitude-bin divided by the sum of bin counts in all bins. For the special case of the probability being equal to zero, the ShEn would also be equal to zero. Just like with the DF calculation, the b-EGMs that were labelled as NaN in the signal preprocessing step, their corresponding entropy was also equal to NaN. The ShEn values were stored in a variable named 'shannonEntropy' and then added to the 'userdata' structure to plot the entropy maps. Figures 3.6 and 3.7 exemplify the filtering of the signals and the histogram to obtain the probabilities for the ShEn calculation, respectively.

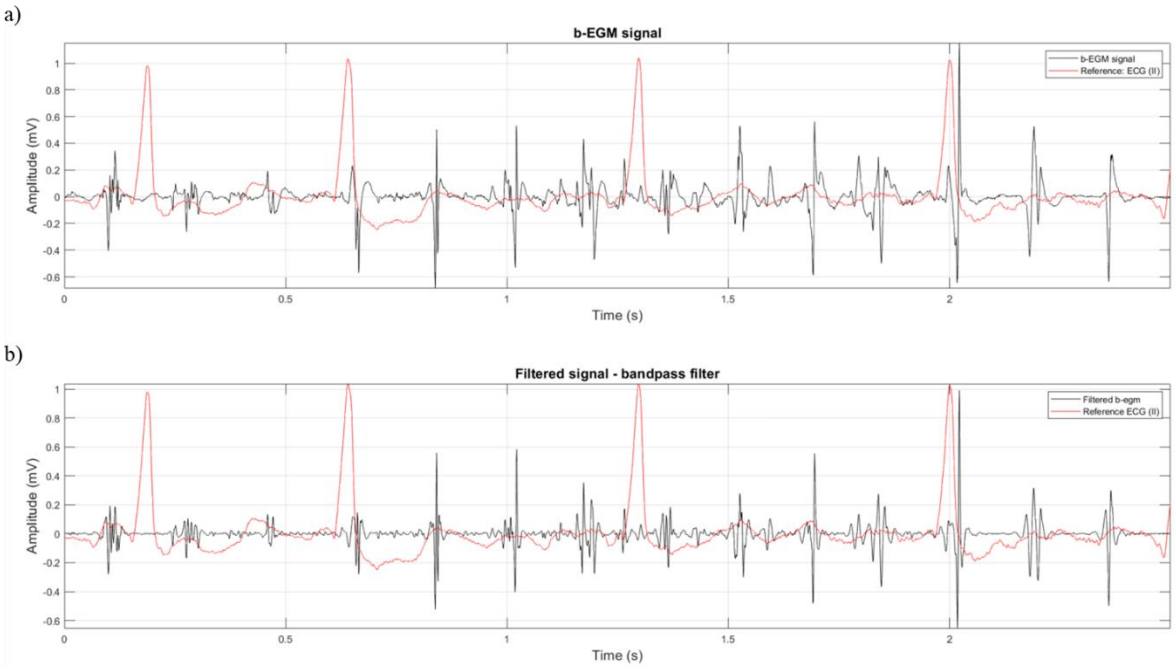

Figure 3.6: Bandpass filter applied to the AF b-EGM signal: a) unfiltered b-EGM signal, and b) after bandpass filtering. The black line is the b-EGM signal, and the red line is the electrical reference (lead II of the ECG).

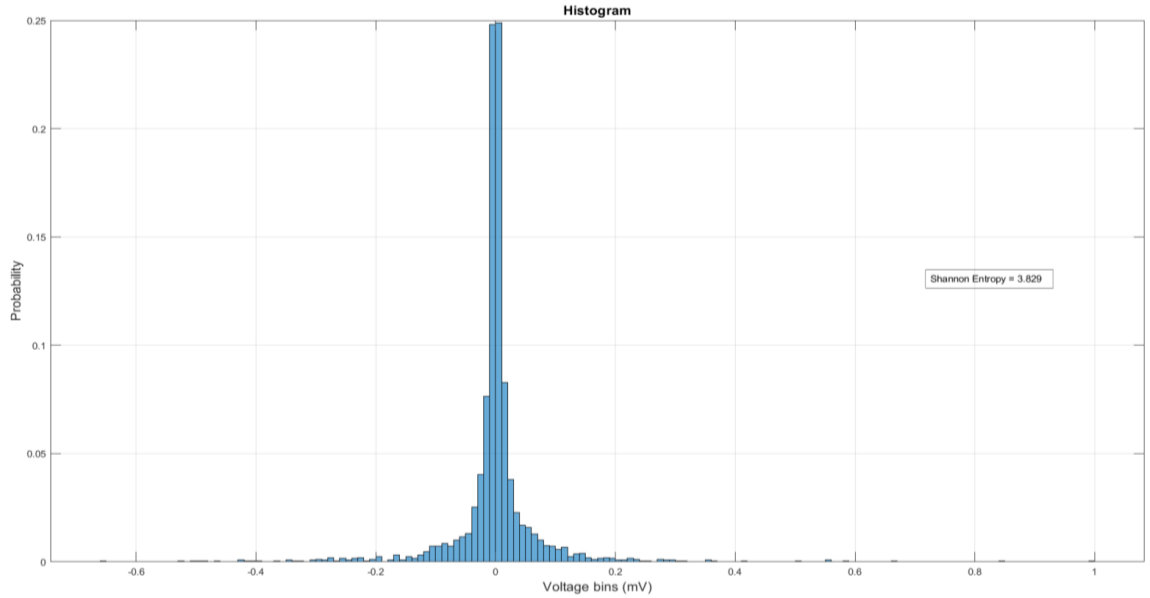

Figure 3.7: Histogram with a fixed bin size of 0.01 mV, to obtain the probabilities for the ShEn calculation. In this case, the ShEn is 3.83.

3.3.3 Dominant Frequency and Shannon Entropy 3D maps

With the DF and ShEn values calculated, the next step was to plot the corresponding maps on the 3D mesh of each patient. To do so, we modified a few scripts from the OpenEP tool and add the options to plot the DF and ShEn maps, since the only available options were the voltage, activation, force, and conduction velocity maps.

First, we had to interpolate the data (voltage, DF, and entropy) so that we could draw the maps on the 3D mesh. In other CARTO systems, the voltage map (and others) is already incorporated in the mesh. However, that is not the case with the one in Santa Marta hospital, but this gives more freedom to modify the algorithm when interpolating the data. This step was performed with the `scatteredInterpolant` function from MATLAB. This function uses a Delaunay triangulation, which is a triangulation-based interpolation.

Next, the vertices of the 3D mesh (stored in variable 'X') were labelled as NaN. These were too far from the mapping points projected to the closest point on the surface of the mesh (stored in variable 'egmSurfX'). To find out which points met this condition, the MATLAB function `knnsearch` was employed. The threshold distance chosen was 10 mm (default) and the Euclidean distance was calculated between the two sets with the `distBetweenPoints` function from the OpenEP tool. In addition, any data that was associated with vertices not referenced by 'triRep' (i.e., vertices that did not belong to the surface mesh) was removed with the function `repack`, also from the OpenEP tool.

The next step was to plot the maps on the LA 3D mesh in a colour-coded fashion. Save for the different data used to draw them, these steps are the same for all maps. We started by drawing the surface mesh of the LA, and this was accomplished with the function `trisurf`, using as input variable the data stored in 'triRep'. The boundaries of the surface mesh, i.e., the mitral valve and the edge of the PVs were drawn using the OpenEP function `drawFreeBoundary`. The distance between vertices in the 3D mesh, and mapping points projected to the closest point on its surface, was calculated with the functions `knnsearch` and `distBetweenPoints`. This is important for the colouring of the 3D mesh because any distance greater than the threshold distance of 10 mm, would be coloured with grey in the colour data matrix. Then, the colormap matrix was created with the MATLAB function colormap, with 256 colours; the interpolated data was scaled according to the colormap scheme and to the superior and inferior limit values imposed. Like that, to each interpolated data point, a RGB triplet that specifies one colour was attributed. So, for example, if colours red and blue correspond to the minimum and maximum DF values, respectively; the interpolated data will be colour-scaled accordingly to that range. The scaling of the data to the desired limits was performed with the function `scaleData` from the OpenEP tool. Although some maps presented a higher maximal (lower minimal) value of voltage/DF/entropy than the limits imposed, an identical scale for all maps was preferred to make comparisons between them. Therefore, it is important to interpret the maps with caution because some maps will present a DFmax/ShEnmax lower than the superior limit of the colour scale.

In total, we plotted three different map sets for each patient with an anterior-posterior orientation: 1) frequency vs voltage maps; 2) entropy vs voltage maps; 3) frequency vs entropy maps. In sets 1 and 2, each frequency and entropy map were followed with a voltage map to identify regions with scar tissue/low voltage and understand if there was any correlation between these regions and the frequency/entropy values. We also plotted frequency and entropy maps side by side to observe if there was any co-location of colours/curves and investigate if the two methods point to the same phenomena or not. In each respective map, the point(s) with maximal DF and entropy was marked to check whether it was located in a lower voltage area, or whether there was a common pattern through different cases. In all sets, the two axes were linked together so that both maps could be rotated and zoomed synchronically. For the frequency maps, low frequencies were displayed in red and high frequencies in blue; in the voltage maps, red represented low voltages ($\leq$ 0.5 mV) and purple normal voltages ($\approx$ 1.5 mV); and lastly for the entropy maps, low entropies were displayed in blue and high entropies in red.

4 Results and Discussion

Here we present the three sets of 3D LA anatomical maps, each with its own subchapter, the discussion of the findings, as well as the limitations encountered during the project. We have elected to include a handful of maps for the purpose of discussion. The remainder are available in the following link: https://cirrus.ciencias.ulisboa.pt/owncloud/s/TRk9CWfgjL55iH3.

4.1 Voltage and DF maps

In general, the maximal DF points were co-located in LVAs (≤ 0.5 mV) (see figure 4.1). Among the LA sites, the LA roof and mitral isthmus were regions most often possessing the highest DF value (DFmax), each appearing in 3 of the 10 patients (30%). Other LA sites with DFmax were the right upper pulmonary vein (RUPV) (10%), posterior (inferior) wall (10%), LA appendage (10%), and septum (10%).

Besides the DFmax regions, in some maps, it was possible to observe sites where the center had a higher frequency which lowered as we moved away from it (see figure 4.2(a)). The delineation of center and periphery was more prominent in some sites than others, where the colours were more homogenous between the surrounding tissue and these sites (see figure 4.2(b)). These could be considered as 'activation cores', 'DF cores', or 'AF sources', in the sense that they could be the source of fibrillatory activity as high DF can be an indicator of high electrical activity or rotor sites. These 'activation cores' were most observed in the LA roof (60%). Other LA sites included the mitral isthmus (30%), septum (30%), LA appendage (30%), posterior wall (20%), right inferior pulmonary vein (RIPV) (20%), left inferior pulmonary vein (LIPV) (10%), and anterior wall (10%). Most patients had more than one DF core, except for two. Depending on the patient, the 'activation cores' were of different sizes, with some being smaller than others; and they mostly superimposed with LVAs (between 0.5 to 1 mV), whilst some overlayed with normal voltage areas (around 1.5 mV). In some maps, the center of the 'activation core', which had a high DF, overlayed with a LVA and the periphery (lower DF) a higher voltage area (normal voltage area) (see figure 4.2(c)). One map presented the exact opposite, as in the high DF center was on top of a normal voltage region and the lower DF periphery a LVA (see figure 4.2(d)).

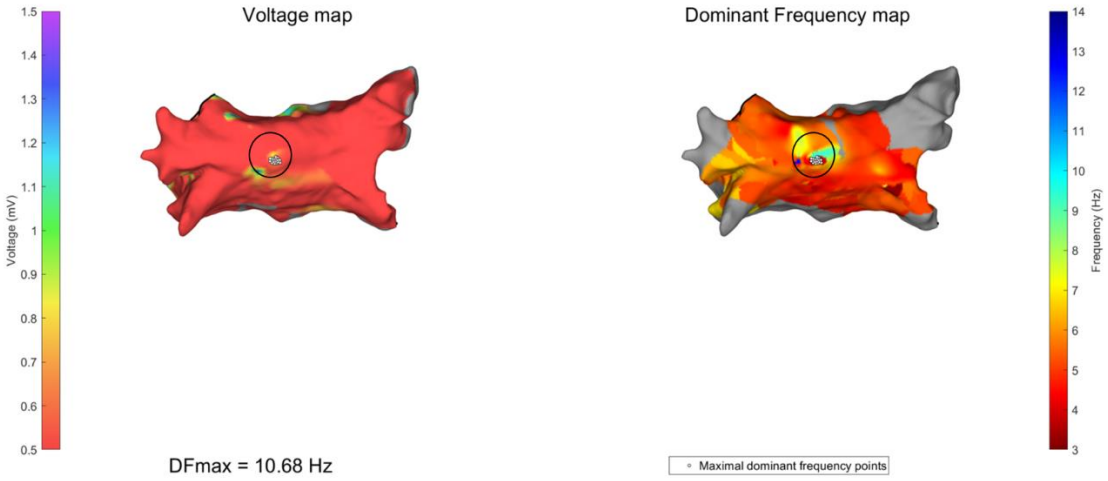

Figure 4.1: Voltage (left) and DF (right) 3D maps from different patients in AF: the maximal DF points were co-located in a LVA of the LA roof.

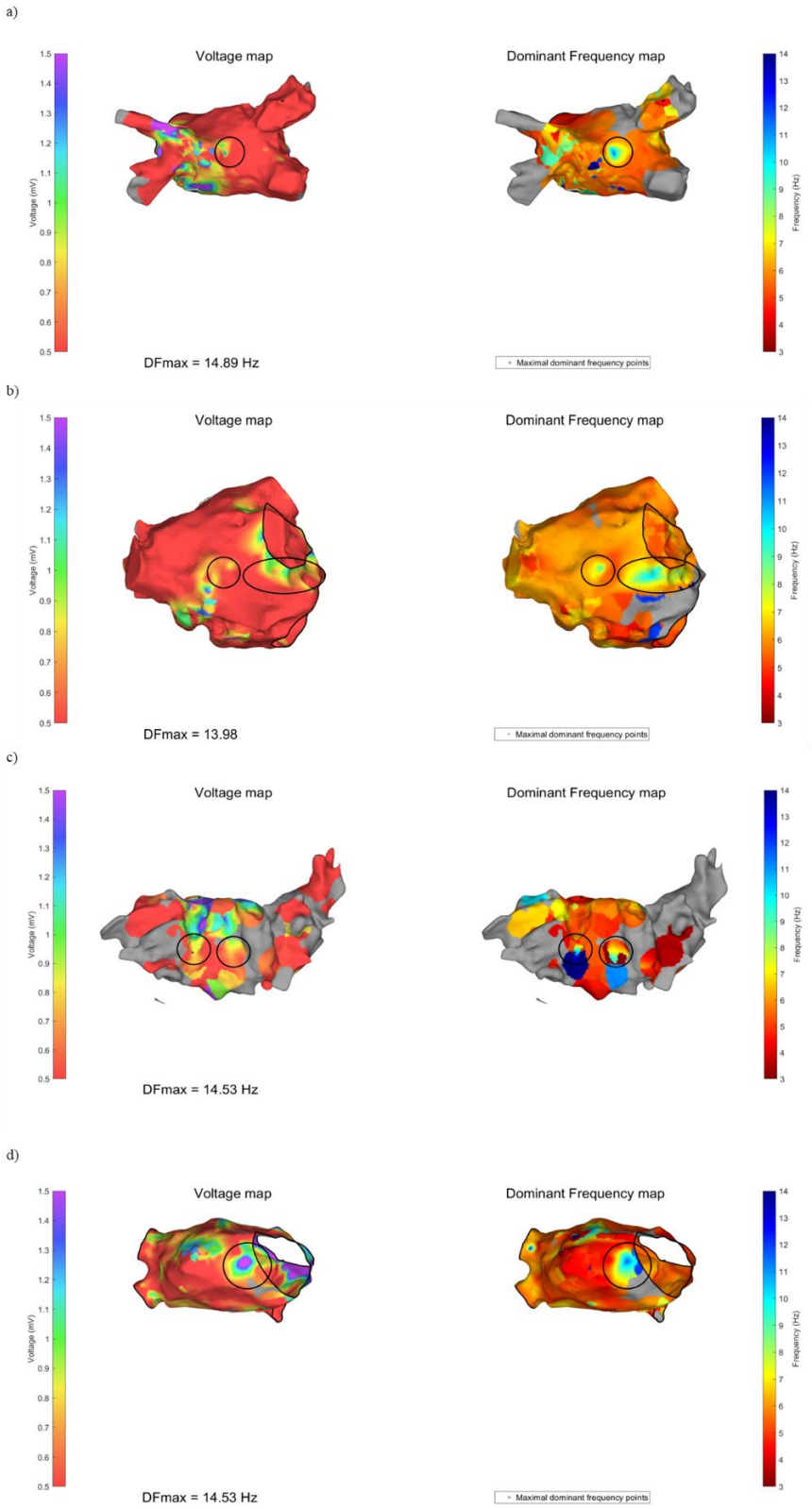

Figure 4.2: Voltage (left) and DF (right) 3D maps from different patients in AF: a) sites that could be the source of fibrillatory activity – 'activation centers' – the center has a higher frequency, and as we move to the periphery, the frequency lowers, b) in some sites, the delineation of center and periphery was more prominent, where the colours were more homogenous between the surrounding tissue and these sites, c) in some maps, the center of the 'activation core' which had a higher DF, overlayed with a LVA, and the periphery which had a lower DF, overlayed with a normal voltage area, d) in this particular map, it happens the exact opposite as in c): the high DF center overlayed a normal voltage region, and the lower DF periphery a LVA.

Surprisingly, there has not been a lot of studies discussing the relationship between LVAs and high-DF sites. K. Kumagai et al. studied the effect of ablation at high-DF sites overlapping LVAs in nonparoxysmal AF patients. The overlap between the LVAs and high-DF sites was frequently observed at the anterior, posterior, lateral, and roof of the LA. They found that in DF-based ablation group, 77% of high-DF sites overlapped with LVAs in the LA of patients with nonparoxysmal AF. This might be because fractionated activity, rotational activity, and discrete rapid local activity associated with LVAs during AF may contribute to the formation of high DFs. They concluded that ablating high-DF sites overlapping with LVAs after a PVI may be beneficial, especially when patients have extensive LVAs to avoid excessive RF applications [126].

Although the mechanism(s) that lead to electrical remodelling and fibrosis of the atria remain poorly understood, these structural alterations are more visible in later stages of AF, and they favour the development of functional reentry susbtrates [127]. LVAs are usually associated with scar tissue/fibrosis, and characterized by slow conduction, heterogenous refractoriness, and rapid repetitive activity [128]. Theoretically, high-DF and DFmax sites may indicate the source of fibrillatory activity because these give an estimation of the activation rate during AF, and even appear to be associated with rotor activity according to some researchers [99], [129]. If so, then the probability of them being located in LVAs would be higher than in normal voltage areas. Therefore, despite of some discrepancy in a few maps, we can affirm that in general, high-DF sites overlayed LVAs, and the results are consistent with the literature.

The benefits of ablating high-DF sites have been a controversial topic because of contradicting results in the literature. As mentioned previously, Atienza et al. first in 2009 showed that ablating high-DF sites prior to PVI had beneficial results for both paroxysmal and persistent patients [92]. These results were later contradicted by the ones from their study later in 2014 [93]. Supporting the new findings, Verma et al. concluded that the ablation of DF sites along with pulmonary vein antral isolation (PVAI) resulted in poor AF termination rates, and 1-year-success was not improved from PVAI alone [130]. Additionally, K. Kumagai et al. reported lower AF termination when combined high DF-guided and CFAE ablation after PVI [131]. These incongruities may also be related to disparities among studies' characteristics (e.g., absence of a control group, heterogeneity among patient's demographics) and their definition of "high DF". Another reason why ablation of high DF sites does not seem to provide better results is because DF analysis is sensitive to the complexity of the atrial EGM in terms of fractionation and amplitude variability, which in turn affects the power spectrum, impairing the DF calculation. DF analysis's vulnerability is not limited to signal processing issues, but also by meandering driver sources/rotors, or pivot of wave fronts. Hence, while a high-DF site might be an indicator of a high frequency driving source related to AF maintenance, it can also be a result of collision or overlap of different wavefronts [132].

Contrarily to DF ablation, the outcomes of low-voltage-areas-guided ablation among studies appear to be more in accordance with each other, and beneficial to paroxysmal and persistent AF patients, despite significant heterogeneities in mapping strategies (such as rhythm during mapping, electrode size, and mapping resolution), patient selection, and LVA prevalence between studies [133]–[136]. Other variables that can influence the accuracy of voltage mapping to detect and quantify atrial fibrosis, and thus the ablation procedure, include the activation direction, catheter incident angle, and atrial tissue properties, such as conduction velocity and tissue thickness [86].

Altogether, to understand if ablating high-DF sites overlapping with LVAs is beneficial to our group subject, only performing PVI versus additional ablation of those areas pointed by the method would be necessary. The patients should then be followed-up on for a period of time to observe any effects post-ablation.

4.2 Voltage and ShEn maps

The LA appendage was, amongst the LA sites, the one where highest entropy value (ShEnmax) was most observed (4 out of 10 patients – 40%) in the ShEn maps. The other LA sites with ShEnmax were the septum (20%), posterior wall (20%), LA roof (10%), and mitral isthmus (10%). There are some conflicting results concerning the overlapping of ShEnmax with the voltage areas. In 7 patients, the ShEnmax overlapped with normal voltage areas (between 1 and 1.5 mV) (see figure 4.3(a)), and the remaining with LVAs (between 0.5 and 0.7 mV) (see figure 4.3(b)). Moreover, the regions of the LA where were most observed high ShEn values were the posterior wall (100%), LA roof (70%), LA appendage (60%), septum (60%), anterior wall (60%), mitral isthmus (30%), and left upper pulmonary vein (LUPV) (10%). A common finding in all maps was that the PVs presented low ShEn values, which makes sense because since the PVs were electrically isolated during mapping, little to no signal was acquired in that area, which translates to an EGM signal with a stable morphology.

We were expecting to observe overlapping of ShEnmax/higher ShEn value sites with LVAs, and lower ShEn value sites with normal voltage areas, because a higher entropy is usually associated with less organized sites (containing a number of different types of deflections) and areas of high electrical activity, which in turn is translated into a site with fibrosis, and vice-versa. As discussed in the previous chapter, fibrosis is characterized by conduction abnormalities, and non-uniform anisotropic impulse propagation, so it would make sense that high ShEn-value sites would overlap with LVAs. Although we did encounter these results in some maps (3 maps in total), they represent the minority. An explanation for this is that since noise is also characterized by high entropy values, those high ShEn-value sites could be associated with the noise of the EGMs and not with its complexity, despite the usage of the bandpass filter.

There have been few studies evaluating and discussing the potential utilities of the ShEn metric in measuring EGM complexity and identifying CFAE sites for AF ablation [70], and assisting AF rotor mapping [97], [98]. In [70], they demonstrated that ShEn, as a statistical measure of complexity, is capable of automatically rank and classify CFAEs, suggesting its usefulness in the study of AF pathophysiology and classification of CFAEs. In the 2013 study conducted by Ganesan et al., they determined whether ShEn, a measure of signal amplitude distribution, could differentiate the pivot of a rotor from surrounding peripheral regions, and thus assist clinical rotor mapping. The results revealed that maximum ShEn was consistently co-located with the pivot zone, and so ShEn is a tool that may be of assistance in AF rotor mapping [97]. In the 2014 study led by Ganesan et al., they tested if the b-EGMs from the pivot of rotors had higher ShEn than EGMs recorded at the periphery due to spatial dynamics of spiral waves. Results showed that ShEn remained consistently high in the pivot zone and was co-localized with the trajectory of the pivoting spiral wave across AP model, variation of bipole recording direction, varying EGM filtering, and rotor meander, supporting the hypothesis of the study [98].

Concerning the relationship between LVAs and ShEn sites in the field of AF, as far as we know, there are not clinical studies discussing this matter, and if there are any potential benefits in ablating high ShEn sites overlaying with LVAs.

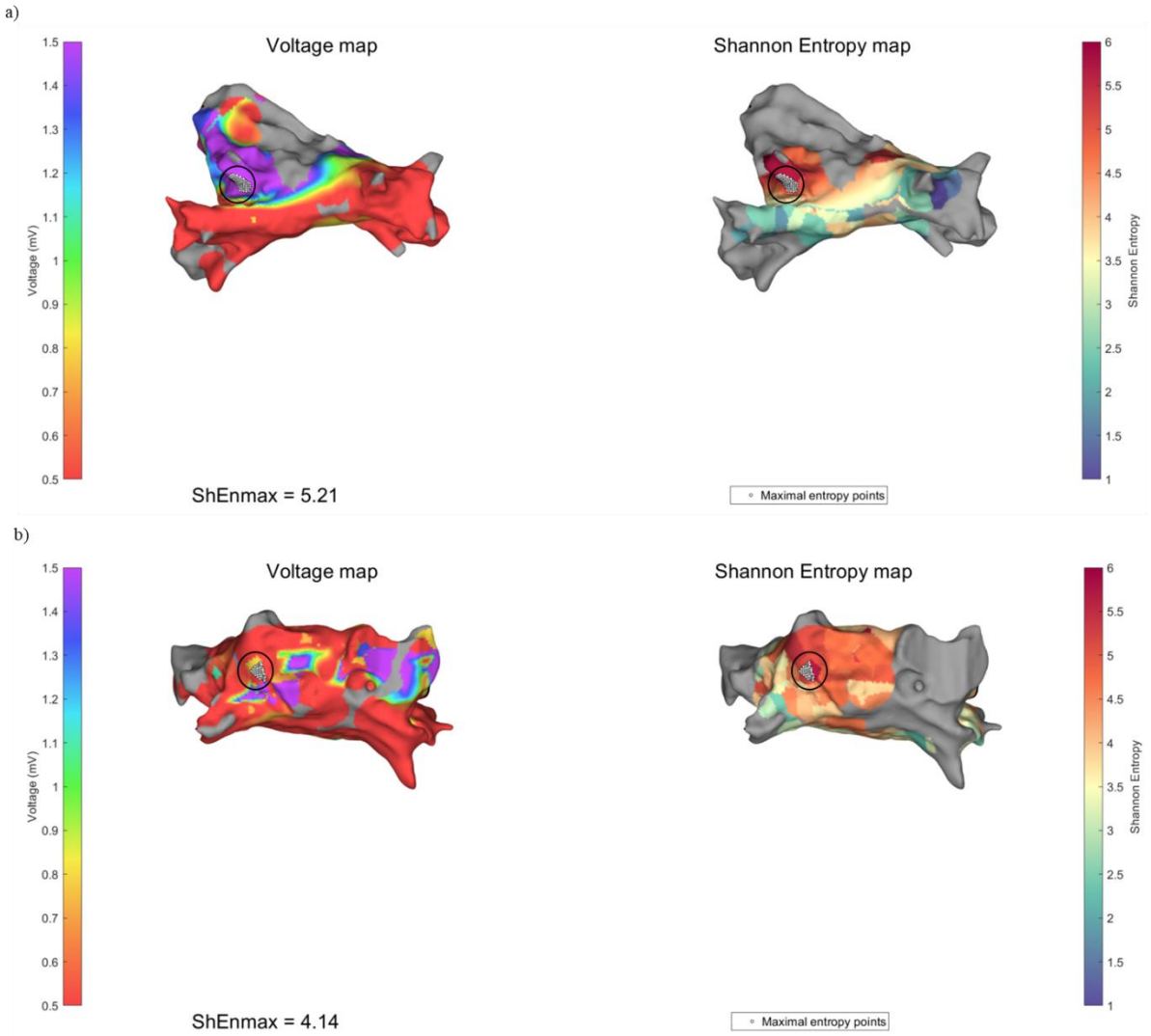

Figure 4.3: Voltage (left) and ShEn (right) 3D maps from different patients in AF: a) the maximal entropy points overlapped with a normal voltage area (≈ 1.5 mV) of the LA appendage, b) the maximal entropy points overlapped with a LVA of the posterior inferior wall.

4.3 DF and ShEn maps

Overall, the ShEnmax sites overlapped with DF areas between 3 and 10 Hz, with the exception of one map that overlapped with the DFmax site at the base of the LA appendage. And the DFmax sites overlapped with ShEn areas between 3.5 and 5, excluding one map (the same exception considered previously) that overlapped with the ShEnmax site. The sites in the DF map characterized by a high frequency center and a low frequency border, the candidates to 'AF cores', overlapped with ShEn areas between 3 and 5. In those same regions in the ShEn maps, it was not possible to observe the distinction of a high entropy center and a low entropy border; the colours were more uniform (see figure 4.4(a) – (b)). So, it is possible that maybe the methods are aiming at different AF mechanisms.

For reasons we explained previously, we were expecting to observe overlapping between ShEnmax sites with DFmax sites, which was not the case for the majority of the maps. We only observed this in one map (see figure 4.5(a)). However, in a few maps, high ShEn sites overlayed with DFmax sites (see figure 4.5(b)), and high ShEn sites overlayed with high DF sites (see figure 4.5(c)). These were easily identified because of the overlaying colours between maps. In some maps, the overlap of colours was more noticeable than in others. There is one patient whose DF and ShEn maps present an interesting spiral shape in the anterior wall (see figure 4.5(d)). The overlapped areas could be considered as AF sources and could point to the same AF mechanism. However, as there is also the possibility of pointing to different mechanisms as described earlier, the only way to confirm this hypothesis would be to ablate those overlayed areas and monitor the outcomes of the procedure. If it turns out that the methods indicate different mathematical phenomena, then we would have to investigate and understand to which phenomena each method is aiming at.

Once more, to our knowledge, there are not many surveys assessing the relationship between the DF and ShEn methods applied to AF study, the potential benefits and drawbacks, if the methods point to the same phenomena, and if they are complementary or redundant. This lack of understanding does not apply solely to DF and ShEn methods, but in general to the methods of different domains in the field of AF. The majority of the studies only employ one or two methods of different domains maximum. If more methods are employed, they are usually of the same domain.

Essentially, there are not many studies in the literature comparing the myriad of methods, and this may be one of the reasons of the inconsistent results throughout the literature. We have poor knowledge of which AF mechanisms the methods underlie exactly (if they in fact point out to different mechanisms), and which methods are most suitable to study the electrophysiological properties of AF (fibrillatory rate, conduction velocity, etc). A few studies worth mentioning concerning this issue are: 1) the study conducted by M. Hwang et al., where they evaluated the nature of rotors in 2D and 3D in-silico models of persistent AF by generating 2D- and 3D-maps of the PS, DF, ShEn, and CFAE-CL during AF. They also compared each method, and the percentage of overlapping areas among the DF, ShEn, and CFAE-CL maps. For the 3D maps, the percentage of overlap was 24.2 between the high DF and high ShEn areas [99]; and 2) the study conducted by I. Romero et al., which represents a frequency analysis of surface ECGs, where they employed three techniques: DF, ensemble average, and wavelet analysis [124].

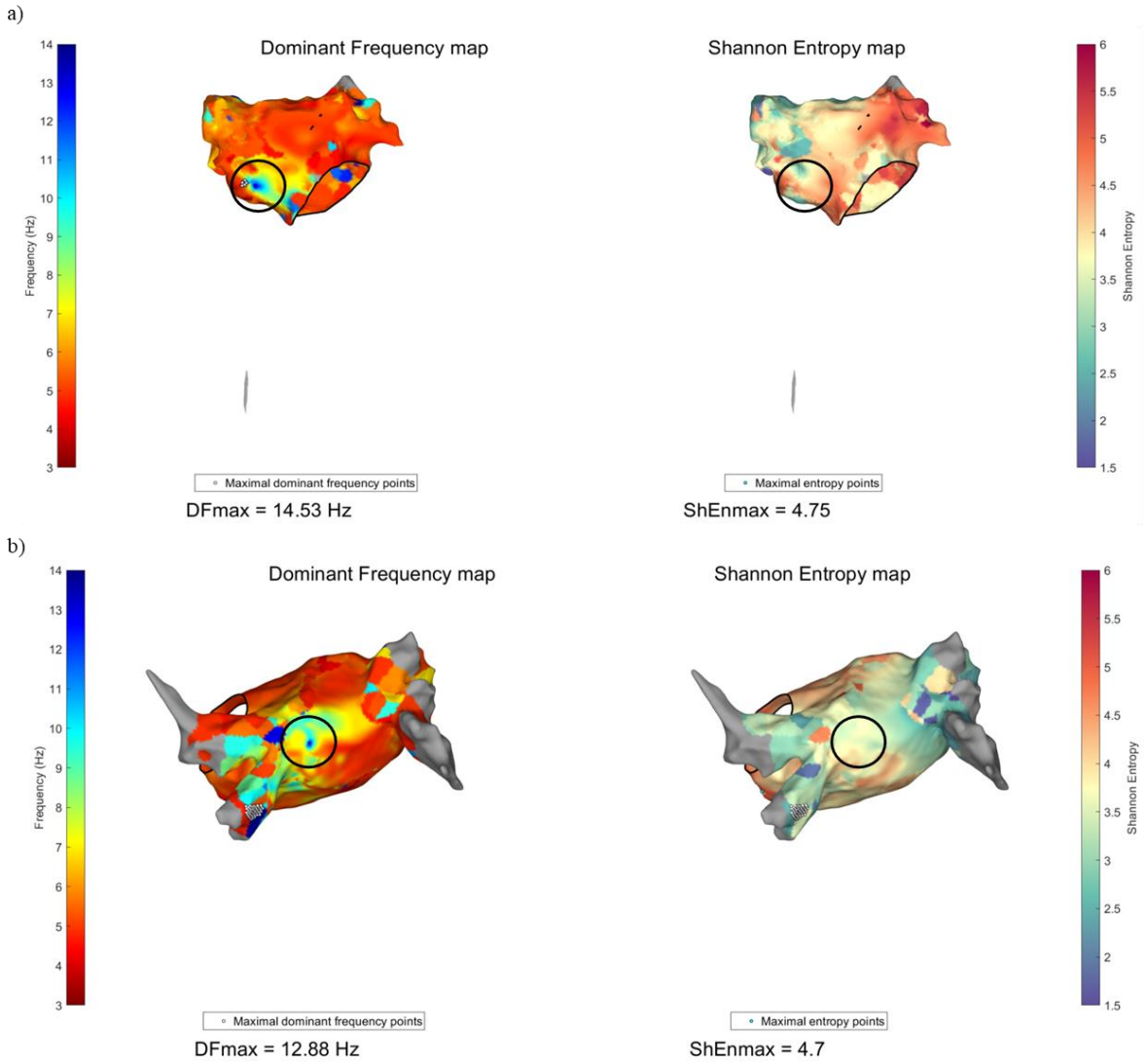

Figure 4.4: DF (left) and ShEn (right) 3D maps from different patients in AF: a 'AF core' candidate located in the septum a) and in the LA roof b). In both DF maps, the center has a higher frequency, and as we move to the border, the frequency lowers. This does not verify in the ShEn map.

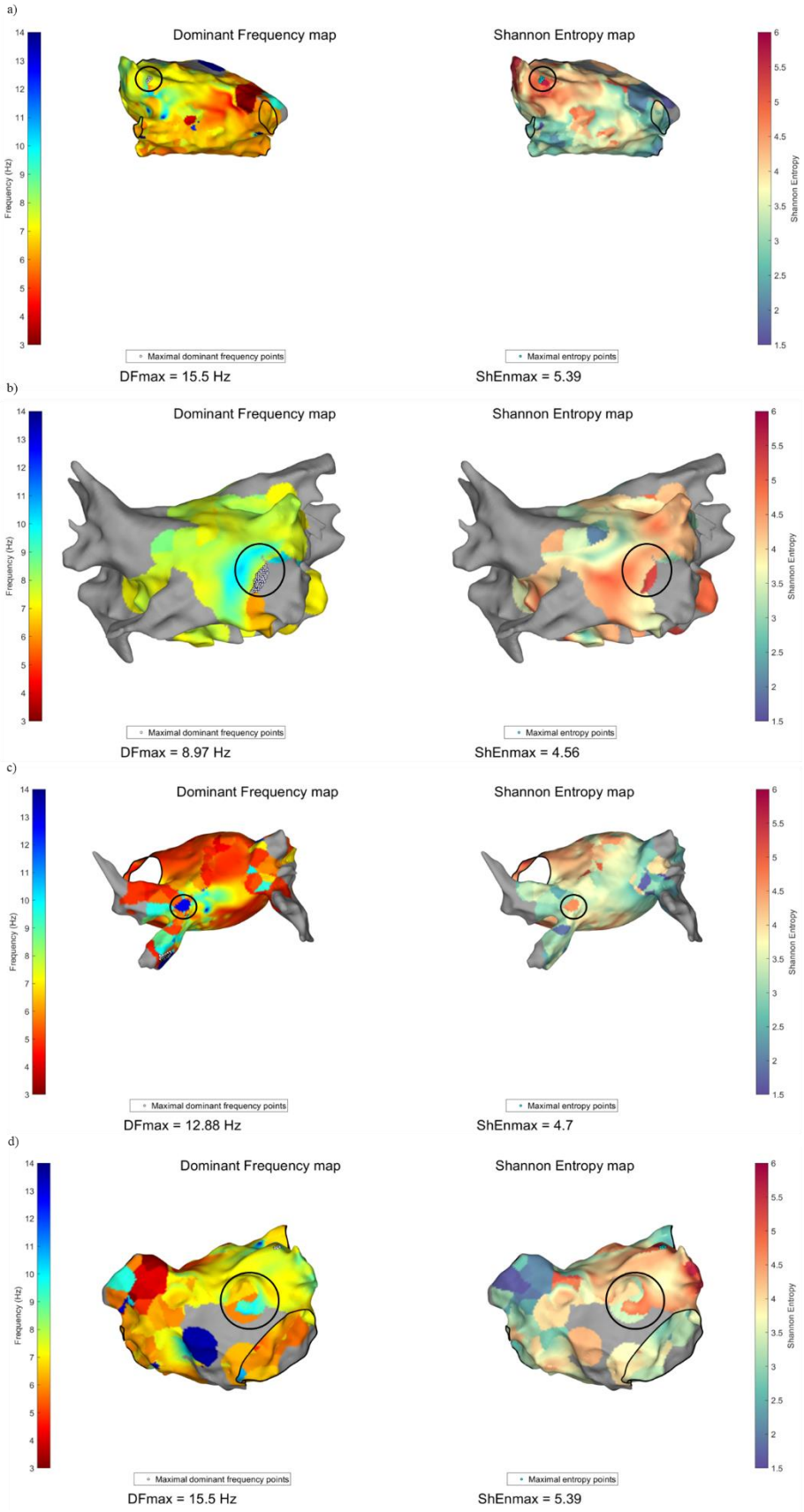

Figure 4.5: DF (left) and ShEn (right) 3D maps from different patients in AF: a) overlapping of a ShEnmax site with a DFmax site at the base of the LA appendage, b) a high ShEn site overlapping a DFmax site in the mitral isthmus, c) a high ShEn site overlaying a high DF site at the LA roof, close to the LIPV, d) a spiral shape located in the anterior wall that could indicate a 'AF source'. We can observe the overlapping colours of the two maps.

4.4 Limitations

As outlined previously, the Fourier transform and Shannon Entropy are not the most suitable methods to analyse physiological signals such as EGM or ECG, because they present some crucial restrictions: employing the Fourier transform implies that the system is linear, and the data is stationary; and the Shannon Entropy does not consider the changing activity of a system over time, and only measures information content in the current value of the time series, and so in both methods we lose the ability to track temporal variations. Physiological signals are nonlinear and nonstationary, for which it is desirable alternative methods that do not assume stationarity and linearity.

An alternative method for frequency analysis could be the Wavelet transform (Continuous wavelet transform and the Discrete wavelet transform), which also allows time analysis of the signal. The Wavelet transform is superior to the Fourier transform because it is not limited to sinusoidal analysis functions, rather a large variety of localized wavelet functions can be employed. This allows a more effective time-frequency decomposition of the signal. Hence, the method is especially useful to analyse transients, aperiodicity, and other non-stationary signal features. In spite of the usefulness of this method, there are only a few studies employing it in the context of AF.

Alternative measures to the 'static' nature of ShEn are the 'dynamic' measures of entropy. The latter allow to study the information content of a system that is changing over time. One such measure is the Approximate Entropy, which is a regularity metric that quantifies the amount of regularity in a signal: signals with complex morphologies, like AF, will exhibit fewer regular patterns, thus yield higher approximate entropy.

The goal of this project was to employ a number of different types of quantitative-EGM-based methods, with a great emphasis on nonlinear methods, and to make comparisons between them and understand if we were observing the same phenomena, and the methods were pointing to the same phenomena, were redundant or complemented each other. Unfortunately, this project only included two methods, that are also not the most fitting for this type of physiological signals. A reason for lack of methods included is because most of the tools or methods are incorporated in the EAM systems, so they are proprietary. This leads researchers to develop their own algorithms, which is custom software and generally not available to the public/open-source. As such, we could only rely on the description of the algorithms provided in the articles to implement them on MATLAB. This can be a setback for someone new to the field, and does not have access to the algorithms/tools to analyse the EGM signals.

Another limitation of this project is the absence of a statistical tool to quantify the metrics displayed in a 3D map. Our goal was to perform statistical analysis on different segments of the LA and not on the entire atrium. Having a 3D representation and not segmenting it, would provide us with very little information of a phenomenon so complex electrically and anatomically like AF, since in different regions of the atrium, various distinct events are occurring simultaneously. To our knowledge, there is not a tool in the literature that performs statistical analysis on 3D maps with thousands of mapping points and analyses colour patterns. We also do not know if it would be feasible computationally.

Lastly, the database used in this project is small, containing only ten patients, and the number of mapping points varied from patient to patient. In particular, one the patients had a map with only a hundred points, compared to the remainder that had between hundreds and thousands of points.

5 Conclusion and Future Perspectives

The present study allowed the comparison of some EGM analysis methods, even though a few results were inconsistent. However, considering the limitations exposed earlier, we did encounter some interesting results and in accordance with the literature, mainly the results from the voltage and DF maps and the presence of 'AF source' candidates. Regarding the DF and ShEn map results, and to answer the inquiry that motivated this project 'do the methods describe/point to the same AF mechanism?', we would have to perform ablation on the regions of the LA where high DF/DFmax and high entropy/ShEnmax sites overlapped. Afterwards, we would follow-up the patients for a period of time to observe the outcomes of the procedure and confirm the hypothesis. There might be a chance that it will not improve ablation outcomes, but at least we would have more information about the relationship between these methods, and which method(s) would be most adequate to clinically study each AF electrophysiological property.

Since the main objective was to compare various different methods, but we ended up including only two, the project would greatly enrich with the addition of more methods of distinct domains (phase, nonlinear, frequency, etc) and make comparisons between them by having the 3D projection of the metrics in the anatomical AF maps of the LA. Like that, we could understand as to why there are several methods in the literature, and if it justifies the need for that; some methods can complement each other, while others can be redundant. It is important to mention that one of the reasons as to why the results are mixed throughout this research field is because the experimental setup varies from study to study, while employing the same methods. These variations lead to positive or negative results depending on the survey, favouring one method over another. A great asset to this study would also be the inclusion of a statistical tool that was able to perform statistical analysis on colour patterns of 3D maps and on the different segments of the LA, as spatial information is vital to understand the complex mechanism of AF.

The mechanisms responsible for initiating and maintaining AF are still unknown for certain, and so a gold standard for treating this disease is also still far from reach, especially for patients with persistent AF. A better understanding of the current methods and their relationship, and further research is required to develop more selective ablation procedures to avoid unnecessary complications and improve ablation procedure effects.

Bibliography

[1] G. A. Roth *et al.*, “Global Burden of Cardiovascular Diseases and Risk Factors, 1990-2019: Update From the GBD 2019 Study,” *J. Am. Coll. Cardiol.*, vol. 76, no. 25, pp. 2982–3021, 2020, doi: 10.1016/j.jacc.2020.11.010.

[2] H. Dai *et al.*, “Global, regional, and national prevalence, incidence, mortality, and risk factors for atrial fibrillation, 1990-2017: Results from the Global Burden of Disease Study 2017,” *Eur. Hear. J. - Qual. Care Clin. Outcomes*, vol. 7, no. 6, pp. 574–582, 2021, doi: 10.1093/ehjqcco/qcaa061.

[3] A. N. Ganesan *et al.*, “Long-term outcomes of catheter ablation of atrial fibrillation: a systematic review and meta-analysis.,” *J. Am. Heart Assoc.*, vol. 2, no. 2, pp. 1–14, 2013, doi: 10.1161/JAHA.112.004549.

[4] V. Markides and R. J. Schilling, “Atrial fibrillation: classification, pathophysiology, mechanisms and drug treatment,” *Heart*, vol. 89, no. 8, pp. 939–943, 2003, doi: 10.1136/heart.89.8.939.

[5] J. L. Salinet, N. Masca, P. J. Stafford, G. A. Ng, and F. S. Schlindwein, “Three-dimensional dominant frequency mapping using autoregressive spectral analysis of atrial electrograms of patients in persistent atrial fibrillation,” *Biomed. Eng. Online*, vol. 15, no. 28, pp. 1–15, 2016, doi: 10.1186/s12938-016-0143-8.

[6] M. D. O. Neill *et al.*, “Catheter Ablation for Atrial Fibrillation AF : Mechanisms and Consequences,” *Circulation*, vol. 116, no. 13, pp. 1515–1523, 2007, doi: 10.1161/CIRCULATIONAHA.106.655738.

[7] F. Sahli Costabal, J. A. B. Zaman, E. Kuhl, and S. M. Narayan, “Interpreting Activation Mapping of Atrial Fibrillation: A Hybrid Computational/Physiological Study,” *Ann. Biomed. Eng.*, vol. 46, no. 2, pp. 257–269, 2018, doi: 10.1007/s10439-017-1969-3.

[8] G. Hindricks *et al.*, “2020 ESC Guidelines for the diagnosis and management of atrial fibrillation developed in collaboration with the European Association for Cardio-Thoracic Surgery (EACTS),” *Eur. Heart J.*, vol. 42, no. 5, pp. 373–498, 2021, doi: 10.1093/eurheartj/ehaa612.

[9] G. Cheniti *et al.*, “Atrial Fibrillation Mechanisms and Implications for Catheter Ablation,” *Front. Physiol.*, vol. 9, no. October, p. 1458, 2018, doi: 10.3389/fphys.2018.01458.

[10] G. G. Lalani, R. Trikha, D. E. Krummen, S. M. Narayan, and C. Observation, “Rotors and Focal Sources for Human Atrial Fibrillation –,” *Circ. J.*, vol. 78, no. 10, pp. 2357–2366, 2014, doi: 10.1253/circj.CJ-14-0478.

[11] J. G. Quintanilla *et al.*, “Mechanistic Approaches to Detect, Target and Ablate the Drivers of Atrial Fibrillation,” *Circ. Arrhythmia Electrophysiol.*, vol. 9, no. 1, 2016, doi: 10.1161/CIRCEP.115.002481.Mechanistic.

[12] F. Ravelli and M. Masè, “Computational mapping in atrial fibrillation: How the integration of signal-derived maps may guide the localization of critical sources,” *Europace*, vol. 16, no. 5, pp. 714–723, 2014, doi: 10.1093/europace/eut376.

[13] M. Baumert, P. Sanders, and A. Ganesan, “Quantitative-Electrogram-Based Methods for Guiding Catheter Ablation in Atrial Fibrillation,” *Proc. IEEE*, vol. 104, no. 2, pp. 416–431, 2016, doi: 10.1109/JPROC.2015.2505318.

[14] A. C. Guyton and J. E. Hall, *Textbook of Medical Physiology*, 11th ed. W. B. Saunders, 2006.

[15] P. A. Iaizzo, *Handbook of Cardiac Anatomy, Physiology, and Devices*, 3rd ed. Totowa: Humana Press, 2006.

[16] F. M. Filipoiu, *Atlas of Heart Anatomy and Development*. London: Springer, 2014.

[17] U. R. Acharya, J. A. E. Spaan, J. S. Suri, and S. M. Krishnan, *Advances in Cardiac Signal Processing*. Springer, 2007.

[18] L. Gaztañaga, F. E. Marchilinski, and B. P. Betensky, "Mechanisms of Cardiac Arrhythmias," *Rev. Espanõla Cardiol.*, vol. 65, no. 2, pp. 174–185, 2012, doi: 10.1016/j.rec.2011.09.020.

[19] S. Saksena and A. J. Camm, *Electrophysiological Disorders of the Heart*, 1st ed. Philadelphia: Elsevier Saunders, 2005.

[20] A. O. Grant, "Cardiac ion channels," *Circ. Arrhythmia Electrophysiol.*, vol. 2, no. 2, pp. 185–194, 2009, doi: 10.1161/CIRCEP.108.789081.

[21] R. L. Cecil, L. Goldman, and A. L. Schafer, *Goldman's Cecil Medicine*, 24th ed. Philadelphia: Elsevier Saunders, 2012.

[22] L. F. Santana, E. P. Cheng, and W. J. Lederer, "How does the shape of the cardiac action potential control calcium signaling and contraction of the heart?," *J. Mol. Cell. Cardiol.*, vol. 49, no. 6, pp. 901–903, 2010, doi: 10.1016/j.yjmcc.2010.09.005.

[23] Z. F. Issa, J. M. Miller, and D. P. Zipes, *Clinical Arrhythmology and Electrophysiology, A Companion to Braunwald's Heart Disease*, 1st ed. Saunders, 2009.

[24] J. J. Goldberger and J. Ng, *Practical Signal and Image Processing in Clinical Cardiology*. Springer, 2010.

[25] J. D. Bronzino, *The Biomedical Engineering Handbook*, 2nd ed. CRC Press, 2000.

[26] P. Laguna and L. Sörnmo, *Bioelectrical Signal Processing in Cardiac and Neurological Applications*. Elsevier Science, 2005.

[27] K. L. Venkatachalam, J. E. Herbrandson, and S. J. Asirvatham, "Signals and signal processing for the electrophysiologist: Part II: Signal processing and artifact," *Circ. Arrhythmia Electrophysiol.*, vol. 4, no. 6, pp. 974–981, 2011, doi: 10.1161/CIRCEP.111.964973.

[28] S. A. Jones, *ECG Notes: Interpretation and Management Guide*, 2nd ed. F. A. Davis Company, 2010.

[29] U. B. Tedrow and W. G. Stevenson, "Recording and interpreting unipolar electrograms to guide catheter ablation," *Hear. Rhythm*, vol. 8, no. 5, pp. 791–796, 2011, doi: 10.1016/j.hrthm.2010.12.038.

[30] W. G. Stevenson and K. Soejima, "Recording techniques for clinical electrophysiology," *J. Cardiovasc. Electrophysiol.*, vol. 16, no. 9, pp. 1017–1022, 2005, doi: 10.1111/j.1540-8167.2005.50155.x.

[31] J. M. T. De Bakker, "Electrogram recording and analyzing techniques to optimize selection of target sites for ablation of cardiac arrhythmias," *Pacing Clin. Electrophysiol.*, vol. 42, no. 12, pp. 1503–1516, 2019, doi: 10.1111/pace.13817.

[32] C. D. Cantwell, C. H. Roney, F. S. Ng, J. H. Siggers, S. J. Sherwin, and N. S. Peters, "Techniques for automated local activation time annotation and conduction velocity estimation in cardiac mapping," *Comput. Biol. Med.*, vol. 65, no. C, pp. 229–242, 2015, doi: 10.1016/j.compbiomed.2015.04.027.

[33] M. El Haddad, R. Houben, R. Stroobandt, F. Van Heuverswyn, R. Tavernier, and M. Duytschaever, "Novel Algorithmic Methods in Mapping of Atrial and Ventricular Tachycardia," *Circulation*, vol. 7, no. 3, pp. 463–472, 2014, doi: 10.1161/CIRCEP.113.000833.

[34] D. L. Mann, D. P. Zipes, P. Libby, R. O. Bonow, E. Braunwald, *Braunwald's Heart Disease: A Textbook of Cardiovascular Medicine*, 10th ed. Philadelphia: Elsevier/Saunders, 2015.

[35] F. Castells, C. Mora, J. Millet, J. J. Rieta, C. Sánchez, and J. M. Sanchis, "Multidimensional ICA for the separation of atrial and ventricular activities from single lead ECGs in paroxysmal atrial fibrillation episodes," *Lect. Notes Comput. Sci. (including Subser. Lect. Notes Artif. Intell. Lect. Notes Bioinformatics)*, vol. 3195, no. September, pp. 1229–1236, 2004, doi: 10.1007/978-3-540-30110-3_155.

[36] V. Fuster *et al.*, "ACC / AHA / ESC Practice Guidelines ACC / AHA / ESC 2006 Guidelines for the Management of Patients With Atrial Fibrillation A Report of the American College of Cardiology / American Heart Association Task Force on Practice Guidelines and the European Soci," *Circulation*, vol. 114, no. 7, pp. e257–e354, 2006, doi: 10.1161/CIRCULATIONAHA.106.177292.

[37] T. H. Everett 4th and J. E. Olgin, "Atrial fibrosis and the mechanisms of atrial fibrillation," *Hear. Rhythm*, vol. 4, no. 3 Suppl, pp. S24–S27, 2007, doi: 10.1016/j.hrthm.2006.12.040.

[38] J. W. Waks and M. E. Josephson, "Mechanisms of Atrial Fibrillation – Reentry, Rotors and Reality," *Arrhythmia Electrophysiol. Rev.*, vol. 3, no. 2, pp. 90–100, 2014, doi: 10.15420/aer.2014.3.2.90.

[39] R. S. Wijesurendra and B. Casadei, "Mechanisms of atrial fibrillation," *Heart*, vol. 105, no. 24, pp. 1860–1867, 2019, doi: 10.1136/heartjnl-2018-314267.

[40] A. Yaksh *et al.*, "Atrial fibrillation: To map or not to map?," *Netherlands Hear. J.*, vol. 22, no. 6, pp. 259–266, 2014, doi: 10.1007/s12471-013-0481-0.

[41] M. J. Shen and D. P. Zipes, "Role of the autonomic nervous system in modulating cardiac arrhythmias," *Circ. Res.*, vol. 114, no. 6, pp. 1004–1021, 2014, doi: 10.1161/CIRCRESAHA.113.302549.

[42] P. Chen, L. S. Chen, M. C. Fishbein, S. Lin, and S. Nattel, "Role of the Autonomic Nervous System in Atrial Fibrillation," *Circ. Res.*, vol. 114, no. 9, pp. 1500–1515, 2014, doi: 10.1161/CIRCRESAHA.114.303772.

[43] M. Qin, X. Liu, and C. Zeng, "The cardiac autonomic nervous system : A target for modulation of atrial fibrillation," *Clin. Cardiol.*, vol. 42, no. 6, pp. 644–652, 2019, doi: 10.1002/clc.23190.

[44] S. Stavrakis and S. Po, "Ganglionated plexi ablation: Physiology and clinical applications," *Arrhythmia Electrophysiol. Rev.*, vol. 6, no. 4, pp. 186–190, 2017, doi: 10.15420/aer2017.26.1.

[45] M. Haïssaguerre *et al.*, "Spontaneous initiation of atrial fibrillation by ectopic beats originating in the pulmonary veins," *N. Engl. J. Med.*, vol. 339, no. 10, pp. 659–666, 1998.

[46] R. Arora *et al.*, "Arrhythmogenic substrate of the pulmonary veins assessed by high-resolution optical mapping," *Circulation*, vol. 107, no. 13, pp. 1816–1821, 2003, doi: 10.1161/01.CIR.0000058461.86339.7E.

[47] M. Hocini *et al.*, "Electrical conduction in canine pulmonary veins: Electrophysiological and anatomic correlation," *Circulation*, vol. 105, no. 20, pp. 2442–2448, 2002, doi: 10.1161/01.CIR.0000016062.80020.11.

[48] S.-A. Chen *et al.*, "Initiation of Atrial Fibrillation by Ectopic Beats Originating From the Pulmonary Veins," *Circulation*, vol. 100, no. 18, pp. 1879–1886, 1999, doi: 10.1161/01.CIR.100.18.1879.

[49] Y. J. Chen and S. A. Chen, “Electrophysiology of pulmonary veins,” *J. Cardiovasc. Electrophysiol.*, vol. 17, no. 2, pp. 220–224, 2006, doi: 10.1111/j.1540-8167.2005.00317.x.

[50] P. Jaïs *et al.*, “Distinctive electrophysiological properties of pulmonary veins in patients with atrial fibrillation,” *Circulation*, vol. 106, no. 19, pp. 2479–2485, 2002, doi: 10.1161/01.CIR.0000036744.39782.9F.

[51] R. Khan, “Identifying and understanding the role of pulmonary vein activity in atrial fibrillation,” *Cardiovasc. Res.*, vol. 64, no. 3, pp. 387–394, 2004, doi: 10.1016/j.cardiores.2004.07.025.

[52] J. R. Ehrlich *et al.*, “Cellular electrophysiology of canine pulmonary vein cardiomyocytes: Action potential and ionic current properties,” *J. Physiol.*, vol. 551, no. 3, pp. 801–813, 2003, doi: 10.1113/jphysiol.2003.046417.

[53] H. Oral *et al.*, “Pulmonary vein isolation for paroxysmal and persistent atrial fibrillation,” *Circulation*, vol. 105, no. 9, pp. 1077–1081, 2002, doi: 10.1161/hc0902.104712.

[54] E. Pokushalov *et al.*, “Ganglionated plexus ablation vs linear ablation in patients undergoing pulmonary vein isolation for persistent/long-standing persistent atrial fibrillation: A randomized comparison,” *Hear. Rhythm*, vol. 10, no. 9, pp. 1280–1286, 2013, doi: 10.1016/j.hrthm.2013.04.016.

[55] G. K. Moe and J. A. Abildskov, “Atrial fibrillation as a self-sustaining arrhythmia independent of focal discharge,” *Am. Heart J.*, vol. 58, no. 1, pp. 59–70, 1959, doi: 10.1016/0002-8703(59)90274-1.

[56] M. A. Allessie, F. I. M. Bonke, and F. J. G. Schopman, “Circus movement in rabbit atrial muscle as a mechanism of tachycardia. III. The ‘leading circle’ concept: a new model of circus movement in cardiac tissue without the involvement of an anatomical obstacle,” *Circ. Res.*, vol. 41, no. 1, pp. 9–18, 1977, doi: 10.1161/01.RES.41.1.9.

[57] H. Calkins *et al.*, “2017 HRS / EHRA / ECAS / APHRS / SOLAECE expert consensus statement on catheter and surgical ablation of atrial fibrillation,” *Hear. Rhythm*, vol. 14, no. 10, pp. e275–e444, 2017, doi: 10.1016/j.hrthm.2017.05.012.

[58] K. R. Grzęda, S. F. Noujaim, O. Berenfeld, and J. Jalife, “Complex Fractionated Atrial Electrograms: Properties of Time- Domain vs. Frequency-Domain Methods,” *Hear. Rhythm*, vol. 6, no. 10, pp. 1475–1482, 2010, doi: 10.1016/j.hrthm.2009.07.014.Complex.

[59] K. Nademanee, M. Schwab, J. Porath, and A. Abbo, “How to perform electrogram-guided atrial fibrillation ablation,” *Hear. Rhythm*, vol. 3, no. 8, pp. 981–984, 2006, doi: 10.1016/j.hrthm.2006.03.018.

[60] S. Nedios, P. Sommer, A. Bollmann, and G. Hindricks, “Advanced Mapping Systems To Guide Atrial Fibrillation Ablation: Electrical Information That Matters,” *J. Atr. Fibrillation*, vol. 8, no. 6, p. 1337, 2016, doi: 10.4022/jafib.1337.

[61] K. Nademanee, E. Lockwood, N. Oketani, and B. Gidney, “Catheter ablation of atrial fibrillation guided by complex fractionated atrial electrogram mapping of atrial fibrillation substrate,” *J. Cardiol.*, vol. 55, no. 1, pp. 1–12, 2010, doi: 10.1016/j.jjcc.2009.11.002.

[62] M. Shenasa, G. Hindricks, M. Borggrefe, and G. Breithardt, *Cardiac Mapping*, 3rd ed. Wiley-Blackwell, 2009.

[63] S. Rolf *et al.*, “Electroanatomical mapping of atrial fibrillation: Review of the current techniques and advances,” *J. Atr. Fibrillation*, vol. 7, no. 4, pp. 57–68, 2014, doi: 10.4022/jafib.1140.

[64] J. Ng, V. Sehgal, J. K. Ng, D. Gordon, and J. J. Goldberger, “Iterative method to detect atrial activations and measure cycle length from electrograms during atrial fibrillation,” *IEEE Trans. Biomed. Eng.*, vol. 61, no. 2, pp. 273–278, 2014, doi: 10.1109/TBME.2013.2290003.

[65] M. El Haddad, R. Houben, R. Stroobandt, F. Van Heuverswyn, R. Tavernier, and M. Duytschaever, “Algorithmic detection of the beginning and end of bipolar electrograms: Implications for novel methods to assess local activation time during atrial tachycardia,” *Biomed. Signal Process. Control*, vol. 8, no. 6, pp. 981–991, 2013, doi: 10.1016/j.bspc.2012.11.005.

[66] R. P. M. Houben, N. M. S. de Groot, F. W. Lindemans, and M. A. Allessie, “Automatic mapping of human atrial fibrillation by template matching,” *Hear. Rhythm*, vol. 3, no. 10, pp. 1221–1228, 2006, doi: 10.1016/j.hrthm.2006.06.009.

[67] J. C. Pachon M *et al.*, “A new treatment for atrial fibrillation based on spectral analysis to guide the catheter RF-ablation,” pp. 590–601, 2004, doi: 10.1016/j.eupc.2004.08.005.

[68] P. Sanders *et al.*, “Spectral analysis identifies sites of high-frequency activity maintaining atrial fibrillation in humans,” *Circulation*, vol. 112, no. 6, pp. 789–797, 2005, doi: 10.1161/CIRCULATIONAHA.104.517011.

[69] J. Ng, A. H. Kadish, and J. J. Goldberger, “Effect of electrogram characteristics on the relationship of dominant frequency to atrial activation rate in atrial fibrillation,” *Hear. Rhythm*, vol. 3, no. 11, pp. 1295–1305, 2006, doi: 10.1016/j.hrthm.2006.07.027.

[70] J. Ng *et al.*, “Measuring the complexity of atrial fibrillation electrograms,” *J. Cardiovasc. Electrophysiol.*, vol. 21, no. 6, pp. 649–655, 2010, doi: 10.1111/j.1540-8167.2009.01695.x.

[71] N. Navoret, S. Jacquir, G. Laurent, and S. Binczak, “Detection of complex fractionated atrial electrograms using recurrence quantification analysis,” *IEEE Trans. Biomed. Eng.*, vol. 60, no. 7, pp. 1975–1982, 2013, doi: 10.1109/TBME.2013.2247402.

[72] D. Scherr *et al.*, “Automated detection and characterization of complex fractionated atrial electrograms in human left atrium during atrial fibrillation,” *Hear. Rhythm*, vol. 4, no. 8, pp. 1013–1020, 2007, doi: 10.1016/j.hrthm.2007.04.021.

[73] R. Vijayakumar, S. K. Vasireddi, P. S. Cuculich, M. N. Faddis, and Y. Rudy, “Methodology considerations in phase mapping of human cardiac arrhythmias,” *Circ. Arrhythmia Electrophysiol.*, vol. 9, no. 11, pp. 1–11, 2016, doi: 10.1161/CIRCEP.116.004409.

[74] S. M. Narayan, D. E. Krummen, and W.-J. Rappel, “Clinical Mapping Approach To Diagnose Electrical Rotors and Focal Impulse Sources for Human Atrial Fibrillation,” *J. Cardiovasc. Electrophysiol.*, vol. 23, no. 5, pp. 447–454, 2012, doi: 10.1111/j.1540-8167.2012.02332.x.Clinical.

[75] T. H. Everett, S. Member, L. Kok, R. H. Vaughn, J. R. Moorman, and D. E. Haines, “Frequency Domain Algorithm for Quantifying Atrial Fibrillation Organization to Increase Defibrillation Efficacy,” vol. 48, no. 9, pp. 969–978, 2001.

[76] L. Faes, G. Nollo, R. Antolini, F. Gaita, and F. Ravelli, “A method for quantifying atrial fibrillation organization based on wave-morphology similarity,” *IEEE Trans. Biomed. Eng.*, vol. 49, no. 12 I, pp. 1504–1513, 2002, doi: 10.1109/TBME.2002.805472.

[77] Ó. Barquero-Prez *et al.*, “Fundamental frequency and regularity of cardiac electrograms with Fourier organization analysis,” *IEEE Trans. Biomed. Eng.*, vol. 57, no. 9, pp. 2168–2177, 2010, doi: 10.1109/TBME.2010.2049574.

[78] M. K. Stiles, P. Sanders, and D. H. Lau, “Targeting the substrate in ablation of persistent atrial fibrillation: Recent lessons and future directions,” *Front. Physiol.*, vol. 9, no. 1158, pp. 1–11, 2018, doi: 10.3389/fphys.2018.01158.

[79] K. Nademanee *et al.*, “A new approach for catheter ablation of atrial fibrillation: Mapping of the electrophysiologic substrate,” *J. Am. Coll. Cardiol.*, vol. 43, no. 11, pp. 2044–2053, 2004, doi: 10.1016/j.jacc.2003.12.054.

[80] H. Oral *et al.*, “Radiofrequency Catheter Ablation of Chronic Atrial Fibrillation Guided by Complex Electrograms,” *Circulation*, vol. 115, no. 20, pp. 2606–2613, 2007, doi: 10.1161/CIRCULATIONAHA.107.691386.

[81] A. Verma *et al.*, “Approaches to Catheter Ablation for Persistent Atrial Fibrillation,” *N. Engl. J. Med.*, vol. 372, no. 19, pp. 1812–1822, 2015, doi: 10.1056/NEJMoa1408288.

[82] M. Sohal *et al.*, “Is mapping of complex fractionated electrograms obsolete?,” *Arrhythmia Electrophysiol. Rev.*, vol. 4, no. 2, pp. 109–115, 2015, doi: 10.15420/aer.2015.04.02.109.

[83] L. J. M. E. van der Does and N. M. S. de Groot, “Inhomogeneity and complexity in defining fractionated electrograms,” *Hear. Rhythm*, vol. 14, no. 4, pp. 616–624, 2017, doi: 10.1016/j.hrthm.2017.01.021.

[84] A. A. Hussein and W. Saliba, “Electrogram - based Mapping and Ablation in Atrial Fibrillation Electrogram - guided PV isolation - Introduction,” in *Cardiac Mapping*, Fifth Edit., 2019, pp. 643–651.

[85] T. P. Almeida *et al.*, “Minimizing discordances in automated classification of fractionated electrograms in human persistent atrial fibrillation,” *Med. Biol. Eng. Comput.*, vol. 54, no. 11, pp. 1695–1706, 2016, doi: 10.1007/s11517-016-1456-2.

[86] I. Sim, M. Bishop, M. O’Neill, and S. E. Williams, “Left atrial voltage mapping: defining and targeting the atrial fibrillation substrate,” *J. Interv. Card. Electrophysiol.*, vol. 56, no. 3, pp. 213–227, 2019, doi: 10.1007/s10840-019-00537-8.

[87] V. B. Traykov, R. Pap, and L. Saghy, “Frequency Domain Mapping of Atrial Fibrillation - Methodology, Experimental Data and Clinical Implications,” *Curr. Cardiol. Rev.*, vol. 8, no. 3, pp. 231–238, 2012, doi: 10.2174/157340312803217229.

[88] J. L. Semmlow, *Biosignal and Medical Image Processing*, 2nd ed. CRC Press, 2004.

[89] J. Ng and J. J. Goldberger, “Understanding and Interpreting Dominant Frequency Analysis of AF Electrograms,” *J. Cardiovasc. Electrophysiol.*, vol. 18, no. January, pp. 680–685, 2007, doi: 10.1111/j.1540-8167.2007.00832.x.

[90] A. Orozco-Duque, J. P. Ugarte, C. Tobón, C. A. Morillo, J. Saiz, and J. Bustamante, “Dominant frequency, regularity and organization indexes response to preprocessing filter variations on simulated electrograms during atrial fibrillation,” *BIOSIGNALS 2013 - Proc. Int. Conf. Bio-Inspired Syst. Signal Process.*, pp. 306–309, 2013, doi: 10.5220/0004231903060309.

[91] A. C. Skanes, R. Mandapati, O. Berenfeld, and J. M. Davidenko, “Spatiotemporal Periodicity During Atrial Fibrillation in the Isolated Sheep Heart,” *Circulation*, vol. 98, pp. 1236–1248, 1998.

[92] F. Atienza *et al.*, “Real-time dominant frequency mapping and ablation of dominant frequency sites in atrial fibrillation with left-to-right frequency gradients predicts long-term maintenance of sinus rhythm,” *Hear. Rhythm*, vol. 6, no. 1, pp. 33–40, 2009, doi: 10.1016/j.hrthm.2008.10.024.

[93] F. Atienza *et al.*, “Comparison of Radiofrequency Catheter Ablation of Drivers and Circumferential Pulmonary Vein Isolation in Atrial Fibrillation,” *J. Am. Coll. Cardiol.*, vol. 64, no. 23, pp. 2455–2467, 2014, doi: 10.1016/j.jacc.2014.09.053.

[94] J. Ng, A. H. Kadish, and J. J. Goldberger, “Technical Considerations for Dominant Frequency Analysis,” *J. Cardiovasc. Electrophysiol.*, vol. 18, no. 7, pp. 757–764, 2007, doi: 10.1111/j.1540-8167.2007.00810.x.

[95] R. Kogawa *et al.*, “Dominant Frequencies and Fractionation Intervals: A Comparison of Bipolar and Unipolar Electrogram-Derived Values,” *J. Nihon Univ. Med. Assoc.*, vol. 75, no. 6, pp. 260–267, 2016, doi: 10.4264/numa.75.6_260.

[96] C. E. Shannon, “A Mathematical Theory of Communication,” *Bell Syst. Tech. J.*, vol. 27, no. 4, pp. 623–656, 1948, doi: 10.1002/j.1538-7305.1948.tb00917.x.

[97] A. N. Ganesan *et al.*, “Bipolar electrogram Shannon entropy at sites of rotational activation implications for ablation of atrial fibrillation,” *Circ. Arrhythmia Electrophysiol.*, vol. 6, no. 1, pp. 48–57, 2013, doi: 10.1161/CIRCEP.112.976654.

[98] A. N. Ganesan *et al.*, “Origin and characteristics of high Shannon entropy at the pivot of locally stable rotors: Insights from computational simulation,” *PLoS One*, vol. 9, no. 11, pp. 1–8, 2014, doi: 10.1371/journal.pone.0110662.

[99] M. Hwang, J. S. Song, Y. S. Lee, C. Li, E. B. Shim, and H. N. Pak, “Electrophysiological rotor ablation in in-silico modeling of atrial fibrillation: Comparisons with dominant frequency, shannon entropy, and phase singularity,” *PLoS One*, vol. 11, no. 2, pp. 1–15, 2016, doi: 10.1371/journal.pone.0149695.

[100] W. Xiong, L. Faes, and P. C. Ivanov, “Entropy measures , entropy estimators , and their performance in quantifying complex dynamics : Effects of artifacts , nonstationarity , and long-range correlations,” vol. 062114, pp. 1–37, 2017, doi: 10.1103/PhysRevE.95.062114.

[101] D. Dharmaprani, L. Dykes, A. D. Mcgavigan, P. Kuklik, and R. Gray, “Information Theory and Atrial Fibrillation (AF): A Review,” vol. 9, no. July, pp. 1–19, 2018, doi: 10.3389/fphys.2018.00957.

[102] E. M. Aliot *et al.*, “EHRA/HRS Expert Consensus on Catheter Ablation of Ventricular Arrhythmias: Developed in a partnership with the European Heart Rhythm Association (EHRA), a Registered Branch of the European Society of Cardiology (ESC), and the Heart Rhythm Society (HRS); i,” *Europace*, vol. 11, no. 6, pp. 771–817, 2009, doi: 10.1093/europace/eup098.

[103] Y. H. Kim *et al.*, “2019 APHRS expert consensus statement on three-dimensional mapping systems for tachycardia developed in collaboration with HRS, EHRA, and LAHRS,” *J. Arrhythmia*, vol. 36, no. 2, pp. 215–270, 2020, doi: 10.1002/joa3.12308.

[104] “Innovative Health: IFUs.” [Online]. Available: https://innovative-health.com/wp-content/uploads/2019/07/IFU-EP-0020_Reprocessed_PentaRay_Nav_eco_High-Density_Mapping_Catheter_Rev-1.pdf. [Accessed: 12-Jul-2022].

[105] I. Deisenhofer, “Mapping of atrial fibrillation : strategies to understand an enigmatic arrhythmia,” *Herzschrittmacherther. Elektrophysiol.*, vol. 29, no. 3, pp. 307–314, 2018, doi: 10.1007/s00399-018-0586-7.

[106] S. Kodali and P. Santangeli, “How, When, and Why High-Density Mapping of Atrial,” *Card. Electrophysiol. Clin.*, vol. 12, no. 2, pp. 155–165, 2020, doi: 10.1016/j.ccep.2020.02.004.

[107] J. P. Piccini and J. P. Daubert, “Cryoablation of atrial fibrillation,” *J. Interv. Card. Electrophysiol.*, vol. 32, no. 3, pp. 233–242, 2011, doi: 10.1007/s10840-011-9603-z.

[108] L. M. Haegeli and H. Calkins, “Catheter ablation of atrial fibrillation: An update,” *Eur. Heart J.*, vol. 35, no. 36, pp. 2454-2459b, 2014, doi: 10.1093/eurheartj/ehu291.

[109] J. D. Fisher, M. A. Spinelli, D. Mookherjee, A. K. Krumerman, and E. C. Palma, “Atrial fibrillation ablation: Reaching the mainstream,” *PACE - Pacing Clin. Electrophysiol.*, vol. 29, no. 5, pp. 523–537, 2006, doi: 10.1111/j.1540-8159.2006.00388.x.

[110] M. K. Hołda *et al.*, “Anatomic characteristics of the mitral isthmus region: The left atrial appendage isthmus as a possible ablation target,” *Ann. Anat.*, vol. 210, pp. 103–111, 2017, doi: 10.1016/j.aanat.2016.11.011.

[111] P. A. Scott, J. Silberbauer, and F. D. Murgatroyd, “The impact of adjunctive complex fractionated atrial electrogram ablation and linear lesions on outcomes in persistent atrial fibrillation: A meta-analysis,” *Europace*, vol. 18, no. 3, pp. 359–367, 2016, doi: 10.1093/europace/euv351.

[112] R. Providência *et al.*, “Is There Still a Role for Complex Fractionated Atrial Electrogram Ablation in Addition to Pulmonary Vein Isolation in Patients with Paroxysmal and Persistent Atrial Fibrillation?,” *Circ. Arrhythmia Electrophysiol.*, vol. 8, no. 5, pp. 1017–1029, 2015, doi: 10.1161/CIRCEP.115.003019.

[113] S. NATH, J. P. DiMARCO, and D. E. HAINES, “Basic Aspects of Radiofrequency Catheter Ablation,” *J. Cardiovasc. Electrophysiol.*, vol. 5, no. 10, pp. 863–876, 1994, doi: 10.1111/j.1540-8167.1994.tb01125.x.

[114] K. H. Kuck *et al.*, “Cryoballoon or radiofrequency ablation for paroxysmal atrial fibrillation,” *J. Cardiopulm. Rehabil. Prev.*, vol. 36, no. 5, pp. 393–394, 2016, doi: 10.1056/NEJMoa1602014.

[115] D. J. Wilber, D. L. Packer, and W. G. Stevenson, Eds., *Catheter Ablation of Cardiac Arrhythmias - Basic Concepts and Clinical Applications*, 3rd ed. Blackwell Futura, 2008.

[116] F. H. M. Wittkampf and H. Nakagawa, “RF catheter ablation: Lessons on lesions,” *PACE - Pacing Clin. Electrophysiol.*, vol. 29, no. 11, pp. 1285–1297, 2006, doi: 10.1111/j.1540-8159.2006.00533.x.

[117] D. E. Haines, “The Biophysics of Radiofrequency Catheter Ablation in the Heart : The Importance of Temperature Monitoring,” vol. 16, pp. 586–592, 1993.

[118] F. Straube *et al.*, “First-line catheter ablation of paroxysmal atrial fibrillation: Outcome of radiofrequency vs. cryoballoon pulmonary vein isolation,” *Europace*, vol. 18, no. 3, pp. 368–375, 2016, doi: 10.1093/europace/euv271.

[119] “OpenEP.” [Online]. Available: https://openep.io/. [Accessed: 01-Aug-2022].

[120] “EPLab Research Works.” [Online]. Available: https://eplabworks.com/. [Accessed: 01-Aug-2022].

[121] G. W. Botteron and J. M. Smith, “A Technique for Measurement of the Extent of Spatial Organization of Atrial Activation During Atrial Fibrillation in the Intact Human Heart,” *IEEE Trans. Biomed. Eng.*, vol. 42, no. 6, pp. 579–586, 1995, doi: 10.1109/10.387197.

[122] F. Castells, R. Cervigón, and J. Millet, “On the Preprocessing of Atrial Electrograms in Atrial Fibrillation : Understanding Botteron’s Approach,” *Pacing Clin. Electrophysiol.*, vol. 37, no. 2, pp. 133–143, 2013, doi: 10.1111/pace.12288.

[123] M. K. Stiles *et al.*, “High-density mapping of atrial fibrillation in humans: Relationship between high-frequency activation and electrogram fractionation,” *J. Cardiovasc. Electrophysiol.*, vol. 19, no. 12, pp. 1245–1253, 2008, doi: 10.1111/j.1540-8167.2008.01253.x.

[124] I. Romero, E. Fleck, and C. Kriatselis, “Frequency analysis of atrial fibrillation surface and intracardiac electrograms during pulmonary vein isolation,” *Europace*, vol. 13, no. 9, pp. 1340–1345, 2011, doi: 10.1093/europace/eur104.

[125] N. Razzaq, S. A. A. Sheikh, T. Zaidi, I. Akhtar, and S. H. Ahmed, “Automated differentiation between normal sinus rhythm, atrial tachycardia, atrial flutter and atrial fibrillation during electrophysiology,” *Proc. - 2017 IEEE 17th Int. Conf. Bioinforma. Bioeng. BIBE 2017*, vol. 2018-Janua, no. October, pp. 266–272, 2017, doi: 10.1109/BIBE.2017.00-43.

[126] K. Kumagai, K. Minami, Y. Sugai, T. Sumiyoshi, and T. Komaru, “Effect of ablation at high-dominant frequency sites overlapping with low-voltage areas after pulmonary vein isolation of nonparoxysmal atrial fibrillation,” *J. Cardiovasc. Electrophysiol.*, vol. 30, no. 10, pp. 1850–1859, 2019, doi: 10.1111/jce.14090.

[127] B. Burstein and S. Nattel, “Atrial Fibrosis: Mechanisms and Clinical Relevance in Atrial Fibrillation,” *J. Am. Coll. Cardiol.*, vol. 51, no. 8, pp. 802–809, 2008, doi: 10.1016/j.jacc.2007.09.064.

[128] Y. K. Iwasaki, K. Nishida, T. Kato, and S. Nattel, “Atrial fibrillation pathophysiology: Implications for management,” *Circulation*, vol. 124, no. 20, pp. 2264–2274, 2011, doi: 10.1161/CIRCULATIONAHA.111.019893.

[129] J. Salinet *et al.*, “Propagation of meandering rotors surrounded by areas of high dominant frequency in persistent atrial fibrillation,” *Hear. Rhythm*, vol. 14, no. 9, pp. 1269–1278, 2017, doi: 10.1016/j.hrthm.2017.04.031.

[130] A. Verma *et al.*, “Relationship Between Complex Fractionated Electrograms (CFE) and Dominant Frequency (DF) Sites and Prospective Assessment of Adding DF-Guided Ablation to Pulmonary Vein Isolation in Persistent Atrial Fibrillation (AF),” *J. Cardiovasc. Electrophysiol.*, vol. 22, no. 12, pp. 1309–1316, 2011, doi: 10.1111/j.1540-8167.2011.02128.x.

[131] K. Kumagai *et al.*, “Combined dominant frequency and complex fractionated atrial electrogram ablation after circumferential pulmonary vein isolation of atrial fibrillation,” *J. Cardiovasc. Electrophysiol.*, vol. 24, no. 9, pp. 975–983, 2013, doi: 10.1111/jce.12166.

[132] F. Atienza *et al.*, “Mechanisms of Fractionated Electrograms Formation in the Posterior Left Atrium during Paroxysmal Atrial Fibrillation in Humans,” *J. Am. Coll. Cardiol.*, vol. 57, no. 9, pp. 1018–1092, 2011, doi: 10.1016/j.jacc.2010.09.066.Mechanisms.

[133] A. S. Jadidi *et al.*, “Ablation of Persistent Atrial Fibrillation Targeting Low-Voltage Areas With Selective Activation Characteristics,” *Circ. Arrhythmia Electrophysiol.*, vol. 9, no. 3, pp. 1–11, 2016, doi: 10.1161/CIRCEP.115.002962.

[134] S. Kircher *et al.*, “Individually tailored vs. standardized substrate modification during radiofrequency catheter ablation for atrial fibrillation: A randomized study,” *Europace*, vol. 20, no. 11, pp. 1766–1775, 2018, doi: 10.1093/europace/eux310.

[135] S. Rolf *et al.*, “Tailored Atrial Substrate Modification Based on Low-Voltage Areas in Catheter Ablation of Atrial Fibrillation,” *Circ. Arrhythmia Electrophysiol.*, vol. 7, no. 5, pp. 825–833, 2014, doi: 10.1161/CIRCEP.113.001251.

[136] B. Yang *et al.*, “STABLE-SR (Electrophysiological substrate ablation in the left atrium during sinus rhythm) for the treatment of nonparoxysmal atrial fibrillation: A prospective, multicenter randomized clinical trial,” *Circ. Arrhythmia Electrophysiol.*, vol. 10, no. 11, pp. 1–13, 2017, doi: 10.1161/CIRCEP.117.005405.

Appendix A: MATLAB codes

A.1 Botteron and Smith approach + DF and OI calculations

```
function userdata_updated = df(userdata,sig)
% DF calculates the Dominant Frequency (DF) and the Organization
Index (OI)


[no_rows,no_cols] = size(sig); % for memory preallocation

fs = 1000; % sampling frequency 1 kHz
nyq = fs/2; % Nyquist frequency

%% Define variables and steps that will be applied during the for
loop

% STEP 1: Bandpass filtering: Butterworth bandpass filtering at 40-
250 Hz (IIR filter)
n1 = 4; % filter order
wn1 = [40 250]/nyq; % cutoff frequencies
ftype1 = 'bandpass'; % bandpass filter
[B1,A1] = butter(n1,wn1,ftype1); % create butterworth filter
sig_fil = zeros(no_rows,no_cols); % matrix with the filtered signal
(bandpass)

% STEP 2: Rectification (absolute value of the signal)
sig_rec = zeros(no_rows,no_cols); % matrix with the rectified
signal

% STEP 3: Low pass filtering: Butterworth lowpass filter
n2 = 8; % filter order
fc = 20/nyq; % cutoff frequency
ftype2 = 'low'; % lowpass filter
[B2,A2] = butter(n2,fc,ftype2);
sig_fil_rec = zeros(no_rows,no_cols); % matrix with the filtered
signal (lowpass)
```

```
% STEP 4: Apply FFT
% Apply window and zero-padding to improve frequency resolution
sig_win = zeros(no_rows,no_cols);
nfft = 2^nextpow2(size(sig,2)*4); % next larger power of 2
fprintf('Frequency resolution: %.2f Hz\n',fs/nfft)
win = hann(no_cols); % hanning window
sig_dft = zeros(no_rows,nfft);
sig_dft_half = zeros(no_rows,nfft/2);
T = nfft/fs; % sampling period
f = linspace(0,nyq-1/T,nfft/2); % frequency vector

% STEP 5: Find the Dominant Frequency
df_int = [3 20]; % interval of interest in Hz

% STEP 6: Organization Index (OI) to ensure reliability in DF
detection
freq_interval = 0.75; % frequency band (Hz)
df_sig = zeros(no_rows,1);
OI = zeros(no_rows,1);

% STEP 7: Calculate the OI

% STEP 8: Add the DF and OI matrices to the userdata structure

%% Actual for loop
for n = 1:no_rows

% Bandpass filter
sig_fil(n,:) = filtfilt(B1,A1,sig(n,:)); % apply filter to signal

% Rectification
sig_rec(n,:) = abs(sig_fil(n,:));

% Lowpass filter
sig_fil_rec(n,:) = filtfilt(B2,A2,sig_rec(n,:));
```

```
% Apply Hanning window
sig_win(n,:) = sig_fil_rec(n,:).*win';

% FFT
sig_dft(n,:) = abs(fft(sig_win(n,:),nfft)).^2/nfft; % power
spectrum
sig_dft_half(n,:) = sig_dft(n,1:nfft/2);  % get first half of the
spectrum

% Find DF
idx = find((f >= df_int(1)) & (f <= df_int(2))); % Indices
corresponding to frequency interval

[~,df_peak] =
findpeaks(sig_dft_half(n,idx),f(idx),'NPeaks',1,'sortstr','descend'
); % get DF, which corresponds to the point
% with maximum power

% In signals where DF > 10 Hz, it's not possible to calculate OI
% because the harmonics are greater than 20 Hz

if df_peak > 10
    OI(n,:) = NaN;
    df_sig(n,:) = round(df_peak,3);

elseif isempty(df_peak)
    OI(n,:) = NaN;
    df_sig(n,:) = NaN;
```

```
else
    % Find DF harmonics
    % Note that the first row of harms_DF will have the fundamental
frequency
    % and then the DF harmonics

    i = 1; % note that harms_DF will have the fundamental frequency
included plus the DF harmonics
    harms_df = [];
    while df_peak*i <= df_int(2)
    %     harms = DF*i; % calculate the harmonics of DF
        harms_df(i,:) = df_peak*i;  % matrix with the harmonics
        i = i+1;
    end

    harms_int = [];
    harms_int = [harms_df-freq_interval,harms_df+freq_interval]; %
DF harmonics within 0.75 Hz interval

    % Find indexes of the harmonics in frequency interval
    idx_harms = []; % store the indexes of the harmonics' duration
    pow_df_harms = []; % power of the fundamental frequency + its
harmonics

    for z = 1:size(harms_int,1)
        idx_harms(z,:) = find((f >= harms_int(z,1)) & (f <=
harms_int(z,2)));

        % calculate area under curve of DF harmonics using
Simpson's Rule
        for w = 1:size(idx_harms,1)
            pow_df_harms(w,:) =
simps(f(idx_harms(w,:)),sig_dft_half(n,idx_harms(w,:))); % power of
the DF and its adjacent frequencies within 0.75 Hz
        end
    end
```

```
num = sum(pow_df_harms);
    total_pow = simps(f(idx),sig_dft_half(n,idx)); % power of the
total spectrum between 3-20 Hz

    % Calculate OI and store DF values for each signal
    OI(n,:) = round(num/total_pow,3);
    df_sig(n,:) = round(df_peak,3);

end
end

userdata_updated = userdata;

% Add fields to the userdata structure
% it's easier to later use the other functions of OpenEP
[userdata_updated.electric.dominantFrequency] = df_sig;
[userdata_updated.electric.organizationIndex] = OI;

% userdata_updated now contains 2 new matrices: DominantFrequency
and OrganizationIndex

end
```

A.2 ShEn calculation

```
function userdata_updated = sentrop(userdata,sig)
% SENTROP calculates the Shannon entropy

userdata_updated = userdata;

fs = 1000; % sampling frequency (Hz)
nyq = fs/2; % Nyquist frequency

[no_rows,no_cols] = size(sig); % for memory preallocation


%% Filtering the signal with a bandpass Butterworth filter 40-250
Hz

sig_fil = zeros(no_rows,no_cols); % for memory preallocation

% Bandpass filter
n1 = 4; % filter order
wn1 = [40 250]/nyq; % cutoff frequencies
ftype1 = 'bandpass'; % bandpass filter
[B,A] = butter(n1,wn1,ftype1); % butterworth filter of order 8

for n = 1:no_rows
    sig_fil(n,:) = filtfilt(B,A,sig(n,:)); % apply filter to signal
end


%% Calculate Shannon Entropy

SE = zeros(no_rows,1);
binwidth = 0.01; % for bipolar egms
% binwidth for voltage histogram
```

```
% outer for loop to go through all signals in sig-matrix
for a = 1:no_rows

    if isnan(sig_fil(a,:))
        SE(a,1) = NaN;
    else
        p =
histcounts(sig_fil(a,:),'BinWidth',binwidth,'Normalization','probab
ility'); % use histcounts instead of
        % histogram because we do not want to plot the histogram.
We only want
        % the probabilities given by the histogram

        % p is the number of bins

        % inner loop to go through the bins of the histogram of
each signal and calculate the
        % Shannon Entropy
        for i = 1:size(p,2)
            if p(1,i) == 0
                entropy(a,i) = 0; % special case for 0*log2(0)
            else
                entropy(a,i) = p(i).*log2(p(i));
            end
        end

        SE(a,1) = round(-sum(entropy(a,:)),3); % store the Shannon
Entropy values
    end
end


% Add the matrix with the Shannon Entropy values to the userdata
structure
% it's easier to later use the other functions of OpenEP
[userdata_updated.electric.shannonEntropy] = SE;
end
```

A.3 Plot 3D anatomical maps (Voltage, DF and ShEn)[1]

```
function fig =
plot_maps(userdata_updated,type1,type2,new_coords_surf)
% PLOT_MAPS plots two different maps in separated 3d shells

% 1st step: load the data and everything necessary for the maps
% 2nd step: prepare mesh for the first map
% 3rd step: prepare data for the first map
% 4th step: prepare mesh for the second map
% 5th step: plot maps in separate 3d-mesh
% 6th step: Link two axes together


%% Check if the user inserted the correct inputs

prompt1 = 'Choose type of map to plot (voltage, df, or entropy -
must be different from type1): ';

while strcmpi(type1,type2) == true || type2 == ""
    warning('type2 must be different from type1');
    type2 = input(prompt1,'s');

end

%% 1st step: set variables for the maps

switch type1

     case 'voltage'
        data1 = userdata_updated.electric.interpData_bip; % voltage
data
        temppts1 = userdata_updated.electric.egmSurfX;
        load('custom_colormap_voltage2.mat'); % custom colormap for
voltage map
        map1 = voltage_custom_map;
        cBarTitle1 = 'Voltage (mV)';
        coloraxis1 = [0.5 1.5]; % mV % coloraxis limits
        str1 = 'Voltage map';
        faceAlpha1 = 1; % transparency of mesh
```

[1] This Matlab script was adapted and modified from the OpenEP tool.

```
case 'df'
        data1 = userdata_updated.electric.interpData_df; %
frequency data
        temppts1 = new_coords_surf;
        map1 = flipud(jet(256)); % colormap for the voltage map
        cBarTitle1 = 'Frequency (Hz)';
        coloraxis1 = [3 14]; % Hz % coloraxis limits
        str1 = 'Dominant Frequency map';
        faceAlpha1 = 1; % transparency of mesh

    case 'entropy'
        data1 = userdata_updated.electric.interpData_entropy;
        temppts1 = new_coords_surf;
        load('custom_colormap_entropy2.mat'); % custom colormap for
entropy map
        map1 = entropy_custom_map;
        cBarTitle1 = 'Shannon Entropy';
        coloraxis1 = [1 6];
        str1 = 'Shannon Entropy map';
        faceAlpha1 = 1; % transparency of mesh

end


%% 2nd step: Prepare mesh for the first map

fig = figure;
subplot(1,2,1)

% threshold distance
t = 10; % mm

% Draw the surface
hSurf1 = trisurf(userdata_updated.surface.triRep, 'edgecolor',
'none'); % trisurf already creates a figure
% creating another Surf will delete the previous one
axis equal vis3d % equal - use the same length for the data units
along each axis
% vis3d - freeze the aspect ratio properties
set(hSurf1, 'facecolor', [.5 .5 .5]); % facecolor is going to be
grey
```

```
set(gcf,'color',[1 1 1]); % sets figure background color to white
% set(gca,'color',[1 1 1]); % sets axes background

% Draw the free boundary, i.e. valve
drawFreeBoundary(userdata_updated.surface.triRep, [0 0 0]);

% Adjust the light/material
material dull
cameraLight

% Adjust the viewpoint
% ap orientation
set(gca, 'cameraposition', get(gca, 'cameratarget') + [0 0 700])

% pa orientation
% set(gca, 'cameraposition', get(gca, 'cameratarget') - [0 0 700])

set(gca, 'cameraupvector', [0 1 0]);

% Every point in the surface - r for required.
rPts = userdata_updated.surface.triRep.X;

% Adjust the appearances of figure
set(gcf, 'color', 'white');

%% 3rd step: prepare data for the first map

% get a handle to the figure and axis
hAx1 = get(hSurf1, 'parent');
% get the data and the coordinates
dataField1 = data1(:,1);

% find the shortest distance from every point in the surface to the
dataset pointcloud
id1 = knnsearch(temppts1, rPts);
cPts1 = temppts1(id1,:); %c for closest
d1 = distBetweenPoints(cPts1, rPts);

% coloraxis has been specified set up for raw data thresholding now
tAboveCAxis1 = zeros(size(d1));
tBelowCAxis1 = zeros(size(d1));

tAboveCAxis1(dataField1>max(coloraxis1)) = 1;
tBelowCAxis1(dataField1<min(coloraxis1)) = 1;
```

```
% get the appropriate color map
end_color1 = map1(end,:);
first_color1 = map1(1,:);


% Limit the size of the colormap
if length(map1) > 256
    map1 = downsample(map1, round(length(map1)/256));
end

disp(['Length of ', type1, ' map is: '  num2str(length(map1))]);

scaledDataField1 = round(scaleData( dataField1(~tAboveCAxis1 &
~tBelowCAxis1), [1 size(map1,1)] ));

iC1 = ones(size(dataField1));
iC1(find(~tAboveCAxis1 & ~tBelowCAxis1)) =
scaledDataField1; %#ok<FNDSB>
thresholdNaN1 = isnan(iC1);
iC1(thresholdNaN1) = 1;
col_1 = map1(iC1,:);

% At this point the color map col is correct for all non-nan points
p satisfying the expression min(caxis)<dataField(p)<max(caxis)
% Threshold based on coloraxis
col_1(logical(tAboveCAxis1),:) = repmat(end_color1,
[numel(find(tAboveCAxis1)),1]);
col_1(logical(tBelowCAxis1),:) = repmat(first_color1,
[numel(find(tBelowCAxis1)),1]);

% Threshold based on the distance t
thresholdDistance1 = zeros(size(d1));
thresholdDistance1(d1>t) = 1;

% Create the color data matrix, making any vertex grey when it is
greater than t distance from the point cloud
col_1(logical(thresholdDistance1),:) = .6; %ie [.6 .6 .6] grey
col_1(logical(thresholdNaN1),:) = .6; % ie [1 1 1] white
% it says white but the color is grey
```

```
%% 4th step: prepare data for the second map

% get the data to plot the map

switch type2
     case 'voltage'
        data2 = userdata_updated.electric.interpData_bip; % voltage
data
        temppts2 = userdata_updated.electric.egmSurfX;
        load('custom_colormap_voltage2.mat'); % custom colormap for
voltage map
        map2 = voltage_custom_map;
        cBarTitle2 = 'Voltage (mV)';
        coloraxis2 = [0.5 1.5]; % mV % coloraxis limits
        str2 = 'Voltage map';
        faceAlpha2 = 1; % transparency of mesh


    case 'df'
        data2 = userdata_updated.electric.interpData_df;
        temppts2 = new_coords_surf;
        map2 = flipud(jet(256));
        cBarTitle2 = 'Frequency (Hz)';
        coloraxis2 = [3 14]; % Hz
        str2 = 'Dominant Frequency map';
        faceAlpha2 = 1; % transparency of mesh

    case 'entropy'
        data2 = userdata_updated.electric.interpData_entropy;
        temppts2 = new_coords_surf;
        load('custom_colormap_entropy2.mat'); % custom colormap for
entropy map
        map2 = entropy_custom_map;
        cBarTitle2 = 'Shannon Entropy';
        coloraxis2 = [1 6];
        str2 = 'Shannon Entropy map';
        faceAlpha2 = 1; % transparency of mesh
end
```

```
% get the data and the coordinates
dataField2 = data2(:,1);
% projected to the closest point on the surface of the chamber

% find the shortest distance from every point in the surface to the
dataset pointcloud
id2 = knnsearch(temppts2, rPts);
cPts2 = temppts2(id2,:); %c for closest
d2 = distBetweenPoints(cPts2, rPts);

% coloraxis has been specified set up for raw data thresholding now
tAboveCAxis2 = zeros(size(d2));
tBelowCAxis2 = zeros(size(d2));

tAboveCAxis2(dataField2>max(coloraxis2)) = 1;
tBelowCAxis2(dataField2<min(coloraxis2)) = 1;

end_color2 = map2(end,:);
first_color2 = map2(1,:);

% Limit the size of the colormap
if length(map2) > 256
    map2 = downsample(map2, round(length(map2)/256));
end

disp(['Length of ', type2,' map is: ' num2str(length(map2))]);

scaledDataField2 = round(scaleData( dataField2(~tAboveCAxis2 &
~tBelowCAxis2), [1 size(map2,1)] ));

iC2 = ones(size(dataField2));
iC2(find(~tAboveCAxis2 & ~tBelowCAxis2)) =
scaledDataField2; %#ok<FNDSB>
thresholdNaN2 = isnan(iC2);
iC2(thresholdNaN2) = 1;
col_2 = map2(iC2,:);
```

```
% At this point the color map col is correct for all non-nan points
p satisfying the expression min(caxis)<dataField(p)<max(caxis)
% Threshold based on coloraxis
col_2(logical(tAboveCAxis2),:) = repmat(end_color2,
[numel(find(tAboveCAxis2)),1]);
col_2(logical(tBelowCAxis2),:) = repmat(first_color2,
[numel(find(tBelowCAxis2)),1]);

% Threshold based on the distance t
thresholdDistance2 = zeros(size(d2));
thresholdDistance2(d2>t) = 1;

% Create the color data matrix, making any vertex grey when it is
greater than t distance from the point cloud
col_2(logical(thresholdDistance2),:) = .6; %ie [.6 .6 .6] grey
col_2(logical(thresholdNaN2),:) = .6; % ie [1 1 1] white
% it says white but the color is grey


% find all points with maximal dominant frequency or maximal
entropy
switch type1
    case 'df'
        max1 = max(data1);
        idx_map_max1 = find(data1 == max1);
        rPts_map1 =
[rPts(idx_map_max1,1),rPts(idx_map_max1,2),rPts(idx_map_max1,3)];

    case 'entropy'
        max1 = max(data1);
        idx_map_max1 = find(data1 == max1);
        rPts_map1 =
[rPts(idx_map_max1,1),rPts(idx_map_max1,2),rPts(idx_map_max1,3)];

end

switch type2
    case 'df'
        max2 = max(data2);
        idx_map_max2 = find(data2 == max2);
        rPts_map2 =
[rPts(idx_map_max2,1),rPts(idx_map_max2,2),rPts(idx_map_max2,3)];
```

```
    case 'entropy'
        max2 = max(data2);
        idx_map_max2 = find(data2 == max2);
        rPts_map2 =
[rPts(idx_map_max2,1),rPts(idx_map_max2,2),rPts(idx_map_max2,3)];

end


%% 5th step: Plot maps

% Update the color of the surface
% the 3d-mesh is colored when this line is executed

set(hSurf1, 'FaceVertexCData', col_1 ...
    ,'FaceColor', 'interp' ...
    ,'FaceAlpha', faceAlpha1 ...
    );


if strcmpi(type1,'df')

    hold on

    graph_pts_df1 =
stem3(hAx1,rPts_map1(:,1),rPts_map1(:,2),rPts_map1(:,3),'filled','L
ineStyle','none' ...
        ,'Marker','o','MarkerSize',3.5,'MarkerEdgeColor','k','Marke
rFaceColor','w');

elseif strcmpi(type1,'entropy')

     hold on

    graph_pts_entrp1 =
stem3(hAx1,rPts_map1(:,1),rPts_map1(:,2),rPts_map1(:,3),'filled','L
ineStyle','none' ...
        ,'Marker','o','MarkerSize',3.5,'MarkerEdgeColor','k','Marke
rFaceColor','c');

end
```

```
% Show the colorbar
hColBar1 = colorbar(hAx1, 'location', 'manual'); % colorbar shows
up
% when this line is executed
hColBar1.Label.String = cBarTitle1;
hColBar1.Colormap = map1;
hColBar1.Position = [0.1 0.15 0.015 0.7];
hColBar1.Label.FontSize = 14;
hColBar1.FontSize = 14;

% Set the figure color axis
colormap(hAx1,map1) % View and set current colormap
caxis(hAx1,coloraxis1); % setup the limits of the colorbar

axis(hAx1,'off')

dim1 = [0.26 0.67 0.15 0.2];

annotation(fig,'textbox',dim1,'String',str1,'FitBoxToText','on' ...
    ,'EdgeColor','none','FontUnits','normalized')


subplot(1,2,2)
% Draw the surface
hSurf2 = trisurf(userdata_updated.surface.triRep, 'edgecolor',
'none'); % trisurf already creates a figure
% creating another Surf will delete the previous one
axis equal vis3d % equal - use the same length for the data units
along each axis
% vis3d - freeze the aspect ratio properties
set(hSurf2, 'facecolor', [.5 .5 .5]); % facecolor is going to be
grey

% set(gcf,'color',[1 1 1]); % sets figure background

% Draw the free boundary, i.e. valve
drawFreeBoundary(userdata_updated.surface.triRep, [0 0 0]);

% Adjust the light/material
material dull
cameraLight
```

```
set(gca, 'cameraupvector', [0 1 0]);

% Get axes
hAx2 = get(hSurf2, 'parent');

% Update the color of the surface
% the 3d-mesh is colored when this line is executed
set(hSurf2, 'FaceVertexCData', col_2 ...
    ,'FaceColor', 'interp' ...
    ,'FaceAlpha', faceAlpha2 ...
    );

if strcmpi(type2,'df')

    hold on

    graph_pts_df2 =
stem3(hAx2,rPts_map2(:,1),rPts_map2(:,2),rPts_map2(:,3),'filled','L
ineStyle','none' ...
        ,'Marker','o','MarkerSize',3.5,'MarkerEdgeColor','k','Marke
rFaceColor','w');

elseif strcmpi(type2,'entropy')

    hold on

    graph_pts_entrp2 =
stem3(hAx2,rPts_map2(:,1),rPts_map2(:,2),rPts_map2(:,3),'filled','L
ineStyle','none' ...
        ,'Marker','o','MarkerSize',3.5,'MarkerEdgeColor','k','Marke
rFaceColor','c');

end

% Show the colorbar
hColBar2 = colorbar(hAx2, 'location', 'manual'); % colorbar shows
up
% when this line is executed
hColBar2.Colormap = map2;
hColBar2.Position = [0.92 0.15 0.015 0.7];
hColBar2.Label.String = cBarTitle2;
hColBar2.FontSize = 14;
hColBar2.Label.FontSize = 14;
```

```
% Set the figure color axis
colormap(hAx2,map2) % View and set current colormap
% this line causes to change the color scheme of the voltage
colorbar

% create colorbar and set range for color
caxis(hAx2,coloraxis2); % setup the limits of the colorbar

axis(hAx2,'off')

dim2 = [0.62 0.67 0.2 0.2]; % title position

annotation(fig,'textbox',dim2,'String',str2,'FitBoxToText','on' ...
    ,'EdgeColor','none','FontUnits','normalized')

if strcmpi(type1,'df')

    annotation(fig,'textbox',[0.2 0.2 0.2 0.05],'String',[type1 '
max = ' num2str(round(max1,2)) 'Hz' ],'FitBoxToText','on' ...
    ,'EdgeColor','none','FontUnits','normalized')

    lgd1 = legend(graph_pts_df1,'Maximal dominant frequency
points','Location','none');
    lgd1.Position = [0.2 0.1 0.2 0.05];
    lgd1.FontSize = 14;

elseif strcmpi(type1,'entropy')

    annotation(fig,'textbox',[0.2 0.2 0.2 0.05],'String',[type1 '
max = ' num2str(round(max1,2))],'FitBoxToText','on' ...
    ,'EdgeColor','none','FontUnits','normalized')

    lgd1 = legend(graph_pts_entrp1,'Maximal entropy
points','Location','none');
    lgd1.Position = [0.2 0.1 0.2 0.05];
    lgd1.FontSize = 14;


end
```

```
if strcmpi(type2,'df')

    annotation(fig,'textbox',[0.6 0.2 0.2 0.05],'String',[type2 '
max = ' num2str(round(max2,2)) 'Hz'],'FitBoxToText','on' ...
    ,'EdgeColor','none','FontUnits','normalized')

    lgd2 = legend(graph_pts_df2,'Maximal dominant frequency
points','Location','none');
    lgd2.Position = [0.6 0.1 0.2 0.05];
    lgd2.FontSize = 14;

elseif strcmpi(type2,'entropy')

    annotation(fig,'textbox',[0.6 0.2 0.2 0.05],'String',[type2 '
max = ' num2str(round(max2,2)) ],'FitBoxToText','on' ...
    ,'EdgeColor','none','FontUnits','normalized')

    lgd2 = legend(graph_pts_entrp2,'Maximal entropy
points','Location','none');
    lgd2.Position = [0.6 0.1 0.2 0.05];
    lgd2.FontSize = 14;

end

%% 6th step: Link the two axes together

hLink =
linkprop([hAx1,hAx2],{'XLim','YLim','ZLim','CameraUpVector',...
    'CameraPosition','CameraTarget'});

% Store the link to rotate and zoom the maps synchronically
setappdata(gcf,'StoreTheLink',hLink);

end
```